PHOTOACOUSTIC SIGNAL CHARACTERIZATION OF CELL MORPHOLOGY IN MICROCHANNEL FLOW

by

Nasire Uluç

B.S., Physics, Trakya University, 2008

M.S., Physics, Boğaziçi University, 2012

Submitted to the Institute for Graduate Studies in
Science and Engineering in partial fulfillment of
the requirements for the degree of
Doctor of Philosophy

Graduate Program in Physics

Boğaziçi University

2018

PHOTOACOUSTIC SIGNAL CHARACTERIZATION OF CELL MORPHOLOGY
IN MICROCHANNEL FLOW

APPROVED BY:

Prof. Mehmet Burçin Ünlü   . . . .
(Thesis Supervisor)

Prof. Naci İnci   . . . .

Assoc. Prof. Özgür Özdemir   . . . .

Hakan Erkol, Ph.D.   . . . .

Onur Ferhanoğlu, Ph.D.   . . . .

DATE OF APPROVAL: 04.10.2018

ACKNOWLEDGEMENTS

Firstly, I would like to acknowledge Prof. Mehmet Burçin Ünlü for his support during my Ph.D. study. He gave me endless support, encouragement, generous instruction and provided motivation, as well as help me to boost my confidence through all my years as a graduate student.

I am extremely grateful to Dr. Hakan Erkol for his valuable guidance, helpful discussions for every step of the research. He offered excellent guidance feedback and suggestions along the way. He is not only a mentor but also a precious friend. I feel honored to work with him.

I am also hugely appreciative of Dr. Uğur Parlatan for helpful discussions and feedback. During my research, he suggested to me the necessary software tools, different methods of optical design, and readings for pursuing Ph.D. research. Without his contribution, this dissertation would not be possible.

I would like to thank Dr. Seydi Yavaş for his critical comments, which enabled me to notice some mistakes on my experiments and make the necessary improvements on my research according to his valuable experience in the field of optics.

Thanks to my dear colleagues Esra Aytaç Kipergil and Aytaç Demirkıran for their valuable suggestions and sharing through all the years. Apart from academic help, they always provided me with emotional support and became my sister and my brother.

I would like to thank The Department of Molecular Biology and Genetics, especially Açelya Yılmazer and Ozan for maintaining cell lines, and their comments and biological advice on my research.

I would like to thank Gizem (Mamık) Alpakut for her valuable suggestions. She provided me with a moral and emotional support during my experiments.

I also extend my thanks to my fellow lab mates and dear friends Şirin Yonucu, İrem Demirkan, Defne Yılmaz for their support.

I am grateful to my dear best friends Pınar Kütükçü and Hüseyin Uzunkoşar, who have provided me with a moral and emotional support in my life. They gave endless support and understanding to every aspect of my life. My unique and sincerest thanks go to my family for their help, and for everything.

ABSTRACT

PHOTOACOUSTIC SIGNAL CHARACTERIZATION OF CELL MORPHOLOGY IN MICROCHANNEL FLOW

Photoacoustic (PA) imaging, a hybrid imaging modality, provides both functional and structural information of biological tissue by combining both optical imaging and ultrasound imaging. It takes advantages of high contrast and resolution, as well as deep tissue penetration. Photoacoustic measurements of biological cells have been used to characterize the cell morphology and allow for the detection of various enzymes activity in vivo and in vitro. In this thesis, I extend the photoacoustic transport model for the examination of detecting red blood cell (RBC) aggregation. To confirm the theoretical predictions, the experiments are conducted by measuring the interaction force between red blood cells via optic tweezers and obtaining photoacoustic signals originating from the blood suspensions. This hybrid simulation approach is for not only the characterization of red blood cell morphology but also for cancer cell lines in the microchannel flow. The activated probe by matrix metalloproteinase (MMP) and melanin-containing which are helpful for the identification of cancer cells are detected in a novel design of microchannels in vitro by using photoacoustic microscopy. Moreover, the laser source used in the field of photoacoustics is developed in terms of flexibility of adjusting pulse duration (5-10 ns), energy (up to 10 μJ), repetition frequency (up to 1 MHz) independently, and wavelength (from 450 to 1100 nm). Regarding the adjustable properties of the fiber laser, the photoacoustic signal is enhanced via bubble dynamics formed under CW irradiation with the help of an analytic model including laser parameters. As a result, the hybrid PAM and OT system can be used for detecting RBC aggregation. Our theoretical simulations show that PA measurements can be used to differentiate levels of RBC aggregation. Moreover, the expression levels of MMPs in cancer cell lines is determined by combining multi-modality data such as PAM, confocal, and acoustic microscopy.

ÖZET

MİKROKANAL AKIŞINDAKİ HÜCRE MORFOLOJİSİNİN FOTOAKUSTİK SİNYAL KARAKTERİZASYONU

Fotoakustik görüntüleme, bir hibrit görüntüleme modalitesi, hem optik görüntüleme hem de ultrason görüntülemeyi birleştirerek biyolojik dokunun hem fonksiyonel hem de yapısal bilgisini sağlar. Biyolojik hücrelerin foto-akustik ölçümleri, hücre morfolojisini karakterize etmek ve çeşitli enzim aktivitelerinin in vivo ve in vitro olarak tespit edilmesine izin vermek için kullanılmaktadır. Bu bağlamda, kırmızı kan hücresi agregasyonunun saptanması için foto akustik taşıma modelinin genişletilmesi amaçlanmıştır. Teorik tahminleri doğrulamak için, kan hücreleri arasındaki etkileşim kuvveti optik cımbız deneyleri aracılığıyla ölçülerek ve kan süspansiyonlarından kaynaklanan foto akustik sinyaller elde edilerek gerçekleştirildi. Bu hibrit simülasyon yaklaşımı sadece kırmızı kan hücresi morfolojisinin karakterizasyonu değil, aynı zamanda mikrokanal akışındaki kanser hücresi çeşitleri için de geçerlidir. Kanser hücreleri-nin tanımlanması için yararlı olan Matriks metalloproteinaz ile aktive edilen prob ve hücrelerdeki melanin içeriği foto akustik mikroskop kullanılarak mikrokanalı taklit eden yeni bir tasarımında olan fantomlar içinde tespit edildi. Ayrıca, fotoakustik alanında kullanılan lazer kaynağı, darbe süresi, enerji , tekrarlama frekansı bağımsız olarak dalga boyu esnekliği açısından geliştirilmiştir. Bu lazerin bağımsız olarak ayarlanabilir özellikleri ile ilgili olarak, sinyal baloncuk yoluyla deneysel olarak geliştirilmiştir. Ayrıca lazer parametreleri de dahil olmak üzere analitik model yardımıy-la CW ışınlama altında oluşan baloncuk dinamiklerinin fotoakustik sinyal üzerindeki etkisi incelenmiştir. Sonuç olarak, PAM ve OT sistemi RBC kümelenmesini tespit etmek için kullanılabilir. Teorik simülasyonlarımız, fotoakustik ölçümlerinin RBC kümelenmesi düzeylerini ayırt etmek için kullanılabileceğini göstermektedir. Ayrıca, kanser hücrelerinde bulunan ve tümörün büyümesine, invazyon ve metastaza sebep olan enzimin seviyeleri, PAM, konfokal ve akustik mikroskop gibi çok modlu verilerin birleştirilmesiyle belirlenir.

TABLE OF CONTENTS

LIST OF FIGURES

LIST OF TABLES

LIST OF SYMBOLS

c_p	constant pressure heat capacity per unit mass
c_s	Speed of sound
d	Local distance between two surface elements of the cells
D	Coefficient of the surface energy
F	Interaction Force
h	Standard deviation of the kernel
H	Heating Function
K	Compressibility
p	Pressure
p_0	Equilibrium pressure
r	Distance between the source and the detector
r'	Radius of the region of interest
S	Source Term
T	Temperature
β	Coefficient of volume thermal expansion
$\triangle$	Interpolation function
ζ	Bulk viscosity
η	Shear viscosity
κ	Trap stiffness
λ	Wavelength
μ_a	Absorption coefficient
∇	Gradient
ρ	Density
ρ_0	Equilibrium density
σ	Beam width
τ	Pulse Duration
φ	Velocity field

ω_0 Resonant frequency of a microbubble

LIST OF ACRONYMS/ABBREVIATIONS

ACF	Autocorrelation Function
AR-PAM	Acoustic Resolution Photoacoustic Microscopy
ASE	Amplified Spontaneous Emission
BBO	Barium Borate
CCD	Charge Couple Device
CW	Continuous Wave
DAQ	Data Acquisition Card
DC	Double Clad
DWA	Dielectric Wall Accelerators
FFAG	FixedField Alternating Gradients
FFT	Fast Fourier Transform
FHG	Fourth Harmonic Generation
FPGA	Field Programmable Gate Array
FWHM	Full Width At Half Maximum
LBO	Lithium Triborate
LMA-PCF	Large Mode Area Photonic Crystal Fiber
MAP	Maximum Amplitude Projection
MMP	Matrix Metalloproteinase
MOPA	Master Oscillator Power Amplifier
MSD	Mean Squared Displacement
OCT	Optical Coherence Tomography
OPO	Optical Parametric Oscillator
OR-PAM	Optical Resolution Photoacoustic Microscopy
OSA	Optical Spectrum Analyzer
OT	Optical tweezers
PAM	Photoacoustic Microscopy
PCF	Photonic Crystal Fiber
PDMS	Polydimethylsiloxanes

PI	Photoacoustic Imaging
PM-SMF	Polarization Maintaining Single Mode Fiber
PNH	Paroxysmal Nocturnal Hemoglobinuriau
PRF	Pulse Repetition Frequency
PVA	Polyvinyl Alcohol
PVCP	Polyvinyl Chloride Plastisol
ROI	Region of Interest
SHG	Second Harmonic Generation
SLMs	Spatial Light Modulators
SNR	Signal To Noise Ratio
SRS	Stimulated Raman Scattering
TA	thermoacoustic
THG	Third Harmonic Generation
UV	Ultra Violet
WDM	Wavelength Division Multiplexer
YD	Yterrbium Doped

1. INTRODUCTION

Photoacoustic microscopy (PAM) enables a remarkable sensitivity to optical absorption and opens up new opportunities to study biological systems at multiple length and timescales non-invasively. Photoacoustic signal generation depends on properties of laser excitation, while photoacoustic signal detection and image formation rely on ultrasonic imaging principles.

First, selecting or developing photoacoustic excitation sources is the state-of-the-art developments of the system in characterizing cells. To increase the sensitivity of the photoacoustic imaging (PAI) technique, it is also necessary to use new exogenous contrast agents which could provide sufficient PA signal even in low concentrations because most diseases such as cancers do not show a good PA contrast using endogenous PAI molecules. The other important steps along this path is the evaluation of the performance of a photoacoustic system, the validation of the imaging agent, and the discrimination of different cancer cells with new design microfluduic devices which provide higher image quality.

Generally, the laser sources used in photoacoustics have very short pulse. Short enough pulses with high pulse repetition rates, and sufficient pulse energies. Moreover, the lasers with a wide range of wavelengths including the visible and the near-infrared (NIR) region, in which biological samples are relatively transparent, are required for the fields of photoacoustics.

1.1. Basic Pirinciple of the Photoacoustic Effect

In the nineteenth century, Alexander Graham Bell irradiated a selenium cell using modulated sunlight and he managed to hear sound waves. He was first reported the photoacoustic effect in 1980. The photoacoustic effect occurs when the modulated energy source is rapidly absorbed by a material [13]. In that case, the duration of the light source should be less than heat relaxation time and the only interaction mechanism

between source and material could be described as absorption since heat diffusion could be ignored. The absorbed light which results from the intrinsic optical absorption spectra induces a thermal expansion in a sample, and a pressure wave is generated called photoacoustic wave. The photoacoustic wave includes the formation of the optical absorption coefficient and the optical intensity [14, 15]. Although both ultrasonics and photoacoustic are based on ultrasonic pressure waves, their methods differ. In the ultrasound field, scattered signal is generated due to the travelling pressure wave towards the material, and the signal has its mechanical properties such as acoustic impedance. Compared to the ultrasonics, the photoacoustic wave coming from a sample is inherently broadband, where the frequencies of the wave depend on the size, shape, and sound speed of the object [16]. Equation represents the heat conduction. Here, T(r,t), S(r,t) are defined as the increase in temperature distribution, and the heat source term coming from the absorbed energy per unit time, per unit volume, where ρ, c, and λ as the mass density, the specific heat, and thermal conductivity of the medium, respectively. The emission of a photoacoustic pressure is represented by the following equation [14, 17, 18]

$$\rho c \frac{\partial T(\mathbf{r}, t)}{\partial t} = \lambda \nabla^2 T(\mathbf{r}, t) + S(\mathbf{r}, t). \tag{1.1}$$

The equation 1.2 represents the photoacoustic wave propagation $p(r,t)$ to the excess temperature distribution, T(r,t);

$$\nabla^2 p(\mathbf{r}, t) - \frac{1}{c_s^2} \frac{\partial^2 p(\mathbf{r}, t)}{\partial t^2} = -\frac{\beta}{c_p} \frac{\partial T^2(\mathbf{r}, t)}{\partial t^2} \tag{1.2}$$

where β is the coefficient of volume thermal expansion, $c_s = 1/\sqrt{\rho K}$ is the velocity of sound, K is the compressibility. The optical energy is absorbed in a short enough temporal pulse, so the first term on the right side of Equation , the thermal conductivity

(λ) can be neglected, and Equation 1.1 can be written as,

$$\frac{\partial T(\mathbf{r},t)}{\partial t} = \frac{S(\mathbf{r},t)}{\rho c}. \tag{1.3}$$

Equation is valid if $\rho c l^2 / K\tau >> 1$, which means that pulse width, τ, is short enough, where l is the absorbance distance. Substitution 1.1 into 1.2, the photoacoustic equation can be written as

$$\nabla^2 p(\mathbf{r},t) - \frac{1}{c_s^2}\frac{\partial^2 p(\mathbf{r},t)}{\partial t^2} = -\frac{\beta}{C_p}\frac{\partial H(\mathbf{r},t)}{\partial t} \tag{1.4}$$

where p is the pressure, t is time, c_s is the sound speed, β is the thermal expansion coefficient, and C_p is the heat capacity in the absorbing medium. The left hand side of the Equation 1.4 describes the wave propagation, and H stands for heating function coming from laser source. The photoacoustic wave equation is solved analytically for simple homogeneous geometries such as spheres, cylinders and infinite planes, and numerically for heterogeneous geometries. Moreover, the equation can be extended in order to extract some distinctive parameters related to cell morphology. A more detailed explanation is described in chapter 4. There are two essential conditions for the generation photoacoustic wave. First, the optical energy is absorbed in the medium before heat conduction; this event could be considered as thermal confinement. Furthermore, the propagation of the acoustic wave happens where the energy is absorbed, which is related to stress confinement. Therefore, the laser pulse width t must be shorter than the thermal and stress confinement times, $t_{stress} = \frac{d}{c_s}$ and $d_{thermal} = \frac{d^2}{\alpha}$ where d is the characteristic length of the object, c_s is the sound speed, and α is the thermal diffusivity [14].

In photoacoustic imaging, a biological sample is illuminated by pulsed laser or modulated continuous wave (CW) laser and the resultant photoacoustic wave is de-
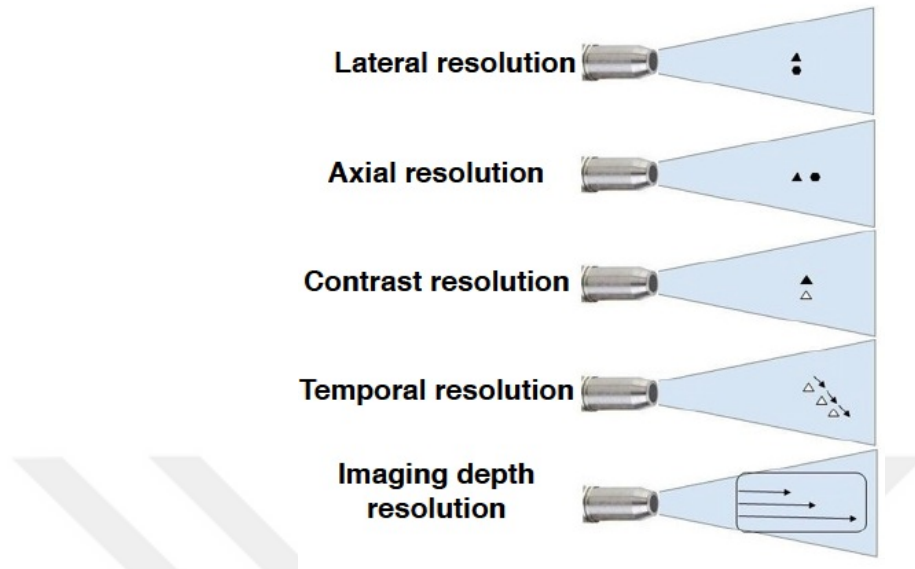
Figure 1.1. Schematic representation of four types of ultrasound resolution.

tected by an ultrasound transducer. For photoacoustic microscopy, the lateral resolution depends on the laser spot size, and the laser spot size is related to both the alignment of the system and the numerical aperture (NA) of the optical objective. While the overall image characteristics in photoacoustics depend on all components of the imaging system such as the laser, the transducer, the electronics, and the scanning, both spatial and contrast resolution play a key role in describing the quality of photoacoustic image. The spatial resolution is classified into two main group such as axial and lateral resolution. The spatial resolution of the image can be described as its ability to distinguish the spatial details and provides identification of objects in space.The imaging parameters of ultrasound equipment ascertain it.

1.1.1. Axial resolution

It is also called as longitudinal or azimuthal resolution, distinguish two objects which lie side by side along the ultrasound beam. Using the value of spatial pulse length (SPL) representing in the following equation, the axial resolution is calculated [19].
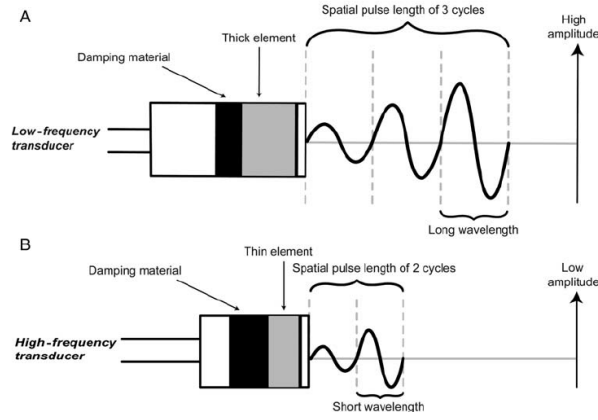
Figure 1.2. (A) Low frequency broadband transducers produce long spatial pulse length and low axial resolution. (B) High frequency broadband transducers produce short pulse length and high axial resolution.

$$\text{Axial Resolution} = \frac{SPL}{2}. \tag{1.5}$$

The SPL is the distance between the beginning of one pulse and the end of that same pulse in the pulse multiplied by the wavelength.

$$SPL = \text{number of cycles in pulse} \times \text{wavelength}. \tag{1.6}$$

Looking at the Equation 1.5, it seems that shorter spatial pulse length leads to a better axial resolution since damping materials absorbing ultrasound put in the particular position at the back of the piezoelectric crystal.

Figure 1.2 illustrates the amplitude change versus distance and indicates the spatial pulse length. The Spatial pulse length is corresponding to the wavelength which is inversely proportional to beam frequency; thus, higher beam frequency improves axial resolution. Nevertheless, sound waves of higher frequency attenuates more because acoustic attenuation is given as $0.6\ dBcm^{-1}MHz^{-1}$ [19]. Taking transducer parameters into consideration, damping determinig the SPL and the frequency identifying the wavelength induces changes in spatial resolution.

1.1.2. Lateral resolution for acoustic-resolution PAM (AR-PAM)

Lateral resolution of ultrasound is expressed as the ability of transducer to distinguish reflectors along the axis perpendicular to the ultrasound beam. It depends on beam width and beam frequency. To illustrate, narrower beam width enables a better lateral resolution since the narrower beam width enhances the transducer's ability in order to discriminate between reflectors types at the same perpendicular line to the transducer. On the other hand, the frequency of the transducer increases, penetration depth decreases. The theoretical lateral resolution value for the AR-PAM is calculated by using the following equation

$$R_{L,AR-PAM} = \frac{0.71V_s}{fNA} \tag{1.7}$$

where f, V_s, and NA are defined as acoustic center frequency, speed of sound, numerical aperture of transducer.

1.1.3. Lateral resolution for optical-resolution PAM (OR-PAM)

The light is tightly focused, and a diffraction-limited focusing is actualized. Because the lateral resolution of OR-PAM is achieved the optical focal spot size, the numerical aperture of objective determines the resolution.

$$R_{L,OR-PAM} = \frac{0.51V_s\lambda}{NA} \tag{1.8}$$

where λ, V_s, and NA are defined as acoustic center frequency, speed of sound, and numerical aperture of objective.

1.1.4. Contrast resolution

It is the capability to distinguish between differences in signal regarding intensity [20]. The signal amplitude is linearly proportional to the absorption coefficient. For photoacoustic imaging, optical absorption properties provide the determination of contrast resolution.

1.2. Laser Sources for Photoacoustic Generation

For photoacoustic imaging, there are several types of lasers such as Q-switched Nd:YAG lasers, Ti:Sapphire lasers, and optical parametric oscillators (OPOs). On the one hand, OPOs have some major limitations of their practical applications such as having low pulse repetition rate, being bulky and expensive, and requiring external cooling units, on the other hand, it takes advantages of tuning with high pulse energies, and wavelength [21]. Based on the applications in the field of photoacoustic, two types of important lasers are used in this thesis. One of them is a custom-made laser, and the other is a commercial laser.

1.2.1. A Custom-Built Fiber Laser

Photoacoustic imaging is based on the detection of generated acoustic waves through thermal expansion of tissue illuminated by short laser pulses. Fiber lasers have recently been preferred for their high repetition frequencies for photoacoustic imaging. Here, we report a unique fiber laser developed specifically for a multiwavelength photoacoustic microscopy system. The laser is custom-made for a maximum flexibility in adjustment of its parameters; pulse duration (5–10 ns), pulse energy (up to 10 μJ) and repetition frequency (up to 1 MHz) independently from each other. The laser covers a broad spectral region from 450 to 1100 nm and also can emit wavelengths of 532, 355, and 266 nm. The laser system consists of a master oscillator power amplifier, seeding two stages; supercontinuum and harmonic generation units. The laser is outstanding since the oscillator, amplifier and supercontinuum generation parts are all-fiber integrated with custom-developed electronics and software. To demonstrate
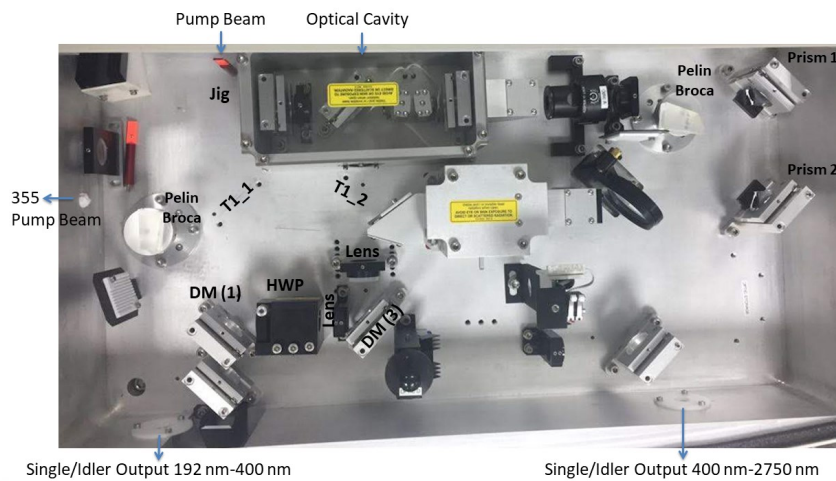
Figure 1.3. The photograph of Horizon OPO system including optical components.

the feasibility of the system, the images of several elements of standardized resolution test chart are acquired at multiple wavelengths. The lateral resolution of optical resolution photoacoustic microscopy system is determined as 2.68 μm. The developed system may pave the way for spectroscopic photoacoustic microscopy applications via widely tunable fiber laser technologies.

1.2.2. Horizon OPO System Description

An optical parametric oscillator (OPO) system generates mid-band radiation in the visible and near-infrared spectral region. The 355 nm Nd:YAG pump laser beam produces coherent light between 400 and 2750 nanometers through the highly efficient single state oscillator. The generation of a wide wavelength range is actualized by optimizing crystal performance with an advanced computer control system. The OPO is constituted of digital motor control of crystals and wavelength separation for optimal output at all times. Moreover, it includes a UV module which enables to generate wavelength coverage from 192-2750 nm. The beam quality, high peak, and average power and mid-bandwidth across an extensive broad tuning range depend on the properties of Horizon OPO parametric converters.

An optical parametric process is responsible for a three-photon interaction. One photon is called as the pump photon which splits into a pair of less energetic ones.

Figure 1.4. The photograph of optical cavity used in OPO laser.

These two photons formed by the pump photon have different energies. The photon with higher energy and the photon with lower energy produced are called as a signal and an idler, respectively. Two photons combine to form a more energetic photon (a third photon). While the optical parametric process occurs, the energy and the momentum vector are conserved, simultaneously by using taking advantage of the birefringence of a transparent nonlinear crystal such as beta-barium borate (BBO). These types of crystals have different indices of refraction for different polarizations of light and these indexes are tuned with changes in the propagation direction according to the crystal angle. The combination of signal and idler frequencies equals the pump frequency in the presence of energy conservation. Nevertheless, the two resultant photons have different frequencies than the pump. If the pump photon orthogonally polarized to the pump, idler and/or signal photons, the conservation of linear momentum is actualized by changing angels of the crystal which determines the pump, idler and signal velocities. In this regard, the crystal realizes all angular conversation momentum because angular momentum conserved.

In order to increase conversion efficiencies, Horizon OPO employs two methods.

Table 1.1. Main components description of optical cavity of Horizon OPO.

Item	Description I	Description II
7	Porro prism	it provides signal-idler walk-off and a resonator
8, A	Half wave plate A option	their ability is to change the attenuation (A 45 rotation changes the attenuation from 5 % and 98 %)
9	Injection Pump Mirror	it optimizes for transmission pump laser beams.
10 11	Crystal 1 BBO Crystal 2 BBO	a non-linear crystal (having the features of good transmission qualitiesand a high damage threshold. it has been pumped by a laser sources at 532 nm, 355 nm, it produces tuning range of wavelength)
12	Mirror	it deviates the light path.
A	Polarizer (option)	it isolates specific polarizations of light.
22	Pelin Broca	it separates the output wavelengths changing direction via motorized system

The first method is that most of the undepleted pump pulse energy back into the nonlinear crystal is reflected by using the output mirror of the Horizon OPO oscillator, which results in the doubling the interaction length between the pump and the generated waves. The second method is to increase the number of round-trips of the oscillating wave during the duration of the pump pulse, as well as to increase the interaction length and efficiency of parametric conversion. If the crystal length is longer, the generated signal and idler waves are shorter. Figure 1.4 represents the optical cavity. The bandwidth of the nonlinear crystal divided by the square root of the number of round-trips in the OPO oscillator determines the linewidth of the OPO output. With a pump as simple Surelite lasers or unseeded Powerlite lasers, the cavity enables to generate less than 3-7 cm^{-1} output bandwidth in the whole tuning range. If the Horizon OPO is pumped by one of the seeded Powerlite lasers, the output linewidth becomes as narrow as 2 cm^{-1} and called as linewidth narrowing. Because of the fact that the output linewidth changes according to the superposition of the crystal's acceptance bandwidth and the pump linewidth, narrower pump linewidth diminishes the output linewidth. Owing to the competition of different spectral components, the pump pulse coming from the unseeded laser possesses a strong amplitude modulation while the pulse from the seeded laser produces a smooth shape with almost the same envelope duration. The energies of both the unseeded and the seeded pulse are the same whereas the higher intensities of the multiple peaks result in a broader output linewidth. The Horizon OPO produces coherent light over a wide wavelength range. The oscillator crystal angle determines the wavelength and produces coherent light. The phase match angle of each of the crystals is realized by rotating them in concert when changing wavelength. The Horizon OPO has software which controls its crystal calibration by keeping all crystal angles, as well as it optimizes Pellin Broca during all wavelength changes. The motor position for each crystal is captured and stored in the software during the tuning range. The critical optical components in the optical cavity are described in Table 1.1 with the number shown in Figure 1.4.

1.3.   Characterization of Biological Cells

Although the photoacoustic image does not include the information about cell shape and structure, the photoacoustic signal with amplitude, width, rise, and relaxation time renders the observation of morphological changes in cells [22–24]. Furthermore, in order to manipulate biological cells and perform sophisticated biophysical or biomechanical characterizations, optical tweezers (OT) are used considering distinct advantages. OT employs a non-contact force for cell manipulation, its force resolution is about 100 aN. It has an ability of transporting foreign materials of applications, delivering cells to specific locations and sorting them in microfluidic systems [25].

In this thesis, the PA signal can enable to detect and characterize red blood cell aggregation. Therefore, studying PA waves coming from red blood cells in a microchannel which mimics a blood vessel structure in vitro can be very useful in the field of blood rheology. The measurements of the interaction force between cells (via conventional techniques such as optical tweezer and atomic microscopy) and the viscosity of aggregated samples as a function of the shear rate (via viscometer) yield the characterization of the aggregation process under distinctive conditions while obtaining photoacoustic waves in various sizes of micro-channels. Our results show that PA can be used to differentiate the red cell aggregation process in detail by using a known interaction force between cells and to combine microfluidic-based measurement methods with photoacoustics. The study of PA signal from the mathematical modeling to the experimental design and detection in micro-channels can be helpful for a therapetic strategy. For example, it can help to make the appropriate choice between surgical and interventional procedures. For a practical application, we studied the red blood cell aggregation in a microcirculatory system. Our detailed analytical solution of the extended photoacoustic transport model combined with a modified Morse type potential function accounts for the dynamics of the aggregate formation. To express the mechanism of RBC aggregation, we measured the interaction force between RBCs, which takes part in Chapter 4.

1.3.1. Principles of Optical Tweezers

Optical tweezers are formed in the presence of highly focused laser beams that lead linear or angular momentum of light to trap μm and nm sized dielectric spherical particles, which is method first proposed by Ashkin [26]. High numerical aperture (NA) objective lens is essential to generate a tightly focused optical trap. Here, linear momentum change occurs due to light refraction and reflection at a sample, leading to trapping forces. The trapping force is controlled by the refractive indices of sample and surrounding medium, laser power, and sample size. According to a theoretical description, there are two different regimes; on the one hand, the trapped particles are much smaller than laser wavelength, on the other hand, trapping samples are much larger than laser wavelength, which can be described by Rayleigh scattering theory and Mie scattering regime, respectively [27].
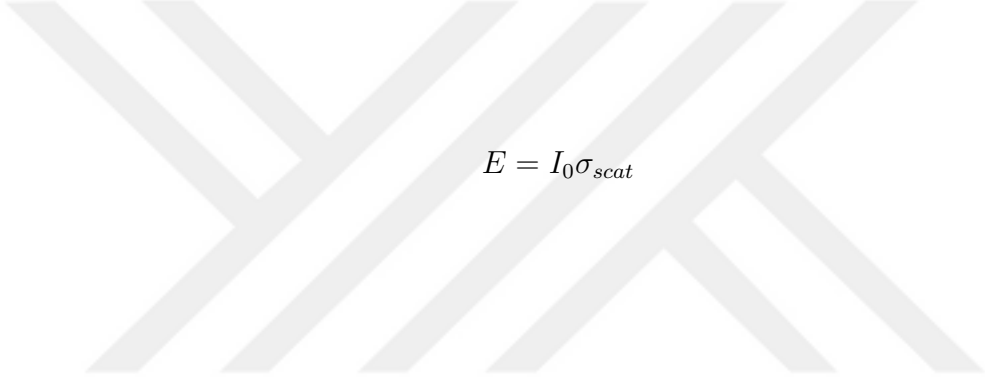
1.3.1.1. The forces arising in the Rayleigh regime (d$<<$ λ). In the case of Rayleigh regime, the diameter of a particle is very small compared to the wavelength. Because of the fact that the wavelength of the trapping beam is larger than the particle size, d, the phase of the field remains constant in time. Thus, the photons behave as waves in this regime. Moreover, the particle can be considered as an induced dipole. The magnitude of the scattering force depends on optical intensity. The incident light and the scattering force have the same direction. The scattering force is expressed as follows:

$$F_{scat} = \frac{n_b P_{scat}}{c} \tag{1.9}$$

where n_b, P_{scat}, and c are defined as the refractive index of the medium, the power of scattered photons and the speed of light, respectively. The scattering cross section for Rayleigh particles is defined as

$$\sigma_{scat} = \frac{2\lambda^2}{3\pi} k^6 \left(\frac{m^2-1}{m^2+2}\right)^2 \tag{1.10}$$

where m and r are an effective refractive index and the radius of the particle, respectively. Here, m and k are defined as the value of m is proportional to surface reflections. Comparing to trap in air (m = 1.65), trapping polystyrene in water (m = 1,24) is achieved without great effort.

$$E = I_0 \sigma_{scat} \tag{1.11}$$

$$F_{scat} = \frac{128\pi^5 r^6}{3c\lambda^4} \left(\frac{m^2-1}{m^2+2}\right)^2. \tag{1.12}$$

The gradient force is proportional to the gradient of optical intensity and propagates in the direction of the gradient of the optical intensity. The gradient force is generally defined as

$$F_{scat} = 4\pi n_b \epsilon a^3 \left(\frac{m^2-1}{m^2+2}\right)^2 n_b \frac{1}{2} \nabla E^2. \tag{1.13}$$

The polarizability, α, for a spherical Rayleigh particle be solved by assuming a particle with radius r, refractive index n_p in a medium of refractive index n_b and an external field E. Following the solution steps [28], the polarizability is found to be
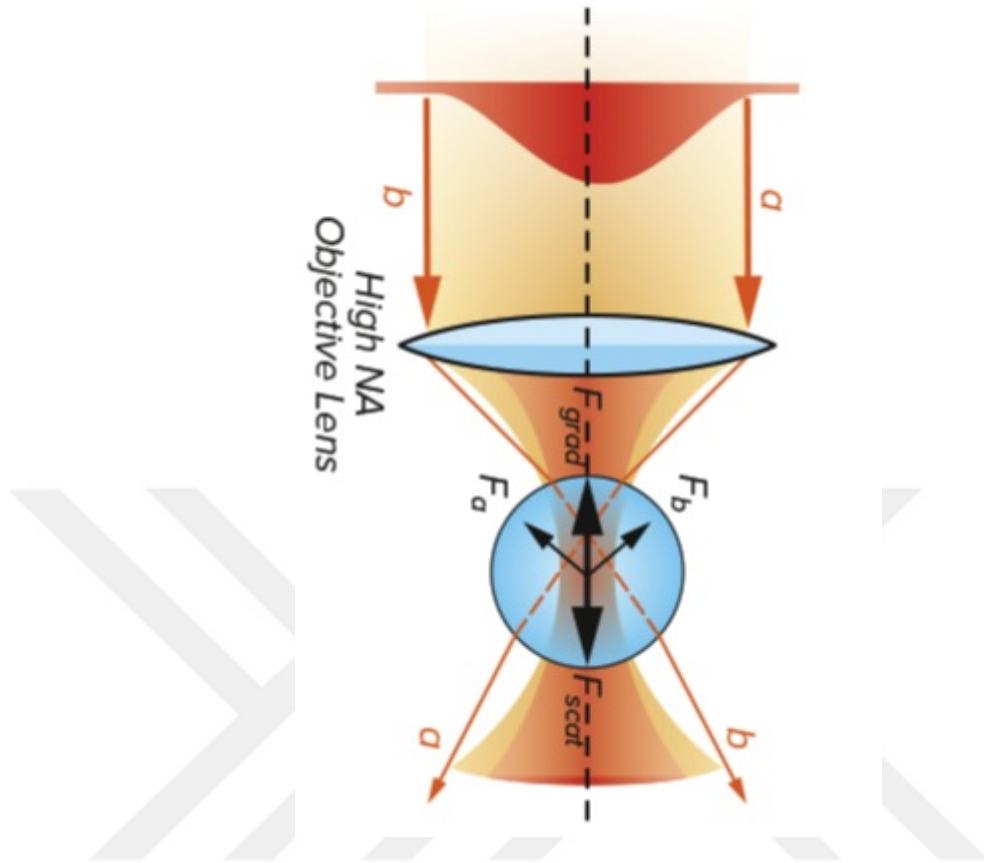
Figure 1.5. Schematic of the net gradient force on a particle.

$$\alpha = n_b r^3 \left(\frac{m^2 - 1}{m^2 + 2}\right).$$

(1.14)

The gradient force can be found using this result as below

$$F_{grad} = 4\pi\epsilon \frac{n_b^2 r^3}{2} a^3 \left(\frac{m^2 - 1}{m^2 + 2}\right) \nabla < E^2 > .$$

(1.15)

1.3.1.2. The forces arising in the Mie regime: (d>> λ). The case of Mie regime is re-alized when the diameter of the particle is much larger than the wavelength of the light. According to the Snell's refraction law and Fresnel's formulas, ray optics description of the optical forces exerted on a dielectric sphere can be represented in Figure 1.5.

Figure 1.5 illustrates two beams as a and b, and these beams resulting from the different intensity gradient regions of the beam exert forces on the particle in a different way. Ashkin reported the ray-optical derivation of the forces arising in the Mie regime in 1992 [29]. He discovered the total net force on the dielectric sphere by considering the contributions from each of the ray entering the aperture of radius r regarding beam axis and the angle alpha with respect to y axis. In this regard, the ray optics calculations were completed with the help of the Fresnel transmission (T) and reflection (R) coefficients. Thus, the contributions of rays that are responsible for sequential reflections and transmissions were evaluated as below [29]: [29]:

$$F_z = F_{scat} = \frac{n_1 P}{c}(1 + R\cos 2\theta - \left\{ \frac{T^2[(\cos 2\theta - 2r) + R\cos 2\theta]}{1 + R^2 + 2R\cos 2r} \right\} \tag{1.16}$$

and

$$F_\gamma = F_{grad} = \frac{n_1 P}{c}(R\sin 2\theta - \left\{ \frac{T^2[(\cos 2\theta - 2r) + R\sin 2\theta]}{1 + R^2 + 2R\cos 2r} \right\} \tag{1.17}$$

where P is the power of beam.

It has been used for measuring the deformability of RBCs beacuse of the fact that it can apply forces at the pN level. It is possible to measure the mechanical properties of RBCs with optical tweezers by using optical force to microspheres attached to RBCs [30, 31] or stretching RBCs by diverging beams from opposite directions. Moreover, OT enables to study cell interaction mechanics by giving detailed information about an individual cell to cell interactions.

1.4. Molecular Imaging of Angiogenesis

Angiogenesis results from new blood vessels originated from the preexisting vasculature. The ability to monitor molecular processes related to the tumor angiogenesis have a vital role in the evaluation of novel antiangiogenic and proangiogenic therapies as

well as early detection of the disease. Expression of various matrix metalloproteinases (MMPs) which have both pro- and antiangiogenic functions plays a great role in the evaluation of every type of human cancer. In particular, both MMP-2 and MMP-9 are defined as the induction of the angiogenic switch in tumor angiogenesis. However, the role of MMPs in tumor angiogenesis is still unknown for most cancers [32]. Razansky *et al.* [33,34] demonstrated that high-resolution deep-tissue multispectral optoacoustic tomography (MSOT) technology has a potential for clinical cardiovascular diagnostics of atherosclerotic plaque instability which leads to the increase of the expression of cathepsins, integrins and MMPs comparing with rotational planar fluorescence imaging. Moreover, Levi *et al.* designed, synthesized, and evaluated a new smart probe in order to detect proteolytic enzyme MMP-2 using photoacoustic microscopy. Furthermore, in vivo MMP is detected by a MMP enzyme-sensitive nano-probe with both CuS nanoparticles and BHQ3 molecules conjugated through a MMP cleavable peptide linker as well as under PA imaging. These types of studies suggest the exploration of smart imaging probes so that the detection of other classes of important functional biological molecules based on PA imaging could be actualized for in vitro and vivo. We aim to reveal that the existence of MMP using a photoacoustic microscopy system (PAM) with OPO laser. In this thesis, to quantitatively distinguish MMP-2 positive (HT-1080, human fibrosarcoma, MeWo, skmel28) from MMP-2 negative (THP-1 (Undifferentiated)) cell cultures, MMPSense-680 and MMPSense-750 probes were used. In this regard, the presence of MMP-2 was investigated with PAM by means of activation-dependent absorption changes. In order to verify probe activation, the cells were visualized using confocal fluorescence microscopy. Under PA imaging and confocal fluorescence microscopy, the cells were loaded into novel microfluidic chips. The characteristics of these cells are given in Table 1.2. The use of microfludic device in this study provides a chance to employ MMP inhibitors for drug delivery. It could pave the way for a better understanding of the role of the MMP in tumor growth and its correlation to the stage of cancer and its metastatic properties.

Table 1.2. Characterization of Ht1080, Thp-1, Skmel28, MeWo, HeLa Cell Lines.

GI	Ht1080	Thp-1	Skmel-28	MeWo	HeLa
Organism	human	human	human	human	human
Tissue	connective tissue	peripheral blood	skin	skin	cervix
Disease	fibrosarcoma	acute monocytic leukemia	malignant melanoma	malignant melanoma	adenocarcinoma
Age	35	1 year infant	51	78	31
Gender	male	male	male	male	female
Cell Types	sarcoma	monocyte	melanoma	melanoma	epithelial
Culture properties	adherent	suspension	adherent	adherenet	adherent
Morphology	eptithelial	monocyte	polygobal	fibroblast	epithelial

1.5. Microfluidic Devices

Microfluidic devices have been developed and it becomes a promising alternative for particle and cell characterization or sorting, trapping, particle development, and coating particles over the last two decades, by using fluorescence [35], electrical impedance [36] or light scattering [37]. Their small size and simple construction render attractive for focusing particles into a narrow stream for a rapid investigation. To illustrate, the classification of particles in terms of the number, size and their distributions are possible via microfluidic devices for rapid analysis of particles. Using microfluidic devices decreases the overall size, complexity, and cost of the instrument. Moreover, the devices can be designed with respect to flow resistances for various applications. For cell culture, special microfluidic devices generated gradient network-based parallel laminar flowing streams are designed [38]. Extensive further research including the creation of microenvironments, the development of cell patterning, 2D and 3D cell culture systems, gradient generation, integration, and automation continue to advance pave the way to represent the complex and diverse range of conditions encountered in natural living systems [39]. The design of stable phantoms is required to evaluate

the performance of a photoacoustic system and can allow to optimize the properties of contrast agents, quantitatively. For photoacoustic, an optimal phantom should have tissue-realistic and controllable acoustic properties for relevant thermoelastic properties, photo- and mechanical stability during the imaging acquisition procedure and long-term stability under storage and repeated use. Taking these properties into consideration, polydimethylsiloxane (PDMS) has been an ideal material to design phantom with exceptionally fine geometry in recent years. Avigo *et al.* [40] designed and developed a PDMS device composed of micrometric channels and tested the performance of a PA imaging system by using selected dyes (ICG) and/or nano-sized contrast agents (i.e., GNRs). In this study, both custom-made agar and PDMS phantom were used to determine which the phantom provides higher signal to noise ratio when the photoacoustic images were acquired. M. Strohm *et al.* [41] integrated for the first time, a microfluidic device with an ultrasound probe for particle characterization.

Besides the advantages, PDMS phantoms have higher acoustic attenuation than the agarose phantom. The drawback reduces image quality parameters such as signal-to-noise ratio (SNR), contrast, uniformity, spatial resolution. In order to compensate for this undesirable situation, we design a PDMS microfluidic device with novel properties. For this thesis, a custom PDMS microfluidic device is composed of eight parallel channels with size varying from 50 μm to 1 mm (50, 250, 300 μm, 1 mm) and a thickness of 1 mm. The PDMS phantom was generated by a standard soft lithography. SU-8 was spin coated on a 100 mm silicon wafer to obtain the structures with 100 μm heights. The photoresist−coated wafers were soft baked at 65 °C for 5 minutes and at 95 °C for 10 minutes. Afterwards, the microchannel design directly was transferred on a photoresist coated wafer using maskless Laser Direct Lithography at 1 um beam size. Next, two consecutive post-baking processes were applied by heating at 65 °C for 5 minute and at 95 °C for 10 min. Using MicroChem's SU-8 developer, the developer purchased from the producer was prepared in a petri dish and the baked photoresist was placed in the dish to be developed for 8 minutes for this application. The developed patterns were rinsed with isopropanol. The resist pattern was hard-baked at 100 °C for 10 minutes.

The PDMS (Sylgard 184, Dow Corning, Midland, MI) prepolymer and curing agent (cross-linker) were prepared in a 10:1 ratio, poured the mixture onto the wafer that includes the master mold, degassed to remove the bubbles baking at 65 °C for 2 h. After cutting the PDMS devices and punching the inlet and outlet ports, both glass and PDMS surfaces were activated using oxygen plasma treatment. The floor of the channels was created by sealing the device to a glass bottom petri dish (11 cm in diameter) that permits the use of an immersion transducer with water. The thickness of a casting layer ($<$ 1 mm) of the PDMS at the top and bottom of the flow channel was preferred in order to minimize acoustic losses.

1.6. Microbubble Generation

Photoacoustic imaging is a non-invasive and high-resolution hybrid imaging modality that bridges the molecular sensitivity of optical imaging and the spatial resolution of ultrasound imaging. It employs light as an excitation source and ultrasound imaging to detect sound waves generated from the absorption of light by endogenous chromophores like blood, melanin, lipids, and even water. In the absence of endogenous absorbers, photoacoustic imaging has been extended to molecular imaging applications through the use of exogenous contrast agents, such as dyes and metallic nanoparticles [42, 43]. Besides these types of contrast agents, microbubble is a possible alternative not only for contrast enhancement and offering greater signal amplification but also for therapeutic agent [44–47].

In the field of photoacoustic imaging, microbubbles used for enhancement of photoacoustic signal are generated by coating with an optically absorbing material or formed under the pulsed or continuous wave laser illuminiation [48]. Diebold *et al.* represented that a chemical reaction leads to the formation of stable gaseous species and the production of the steam bubble during photoacoustic and photothermal processes through transient grating experiment [49, 50]. The steam bubble produces a sizeable pressure increase within the bubble and enables obtaining a powerful sound generation, which has a great role in photoacoustic effect as contrast agents and as directed therapy agents. Gonzalez *et al.* [51] proposed a mathematical model in which

a simulation program based on the widely known Rayleigh–Plesset model [52–54]. He supported experimentation to explain the behavior found on the photoacoustic effect generated by laser-induced nanobubbles in colloidal gold solutions. The regime that precludes transitions for bubble generation based on thermal nonlinearity yields the ability to discriminate between different types of the absorber. In that case, measuring the temperature changes based on photoacoustic amplitude discriminates the types of tissue during thermal therapies [55].

Gas and vapor bubble formations of nano- and micrometric sizes in aqueous solutions under the pulsed laser illumination are involved in many processes and applications. Although the bubble formation under the pulsed laser illumination is the main object during the applications [56–59, 59, 60], the bubble generated by short laser pulse induces liquid evaporation and bubble growth very rapidly [61]. The bubble generation behavior by continuous wave (CW) laser radiation is more suitable compared with the bubble formation under pulsed laser irradiation in terms of considerable variation in behavior, mostly in their resonant size, with some bubbles growing from sub-resonant to super-resonant size during exposure [62–64]. Moreover, the microbubbles under CW laser illumination exhibit stronger nonlinear behavior than expected, and an increase in the generation of acoustic emissions at harmonic and subharmonic frequencies. These significant results are useful for contrast-enhanced PA imaging/therapeutic agent [65].

Photoacoustic (PA) and thermoacoustic (TA) effects have been reported in many applications. Pulsed laser induced photoacoustic effect and CW laser-induced thermotherapy are incorporated to guide and monitor photothermal therapy. The temperature rises during therapy and before therapy is identified by generated photoacoustic waves in the presence of photo absorbers. In parallel, there are several significant theoretical and simulation studies which establish nonlinear PA and TA generation efficiency and optimize of photomechanical drug delivery [66–68]. The PA/TA theoretical models are expressed in terms of multiple physical processes including absorption, heating, thermoelastic expansion, and mechanical vibration [69, 70].

In Chapter 6, we used experimental results to propose theoretical model mecha-

nisms including nonlinear photoacoustic signal amplification and changes from a bipolar shape in the linear regime to a tripolar shape due to localized temperature enhancement and the acoustic pressure variation emitted by microbubble under both pulse and CW illuminations on the basis of dynamics of microbubble growth. The wave equation modified by Markus W. Sigrist [70] is extended to include the pressure changes radiated by the bubble. We propose an analytical model approximation which is verified by the experimentally measured results. Besides, our analytic model enables adjustment the pulse duration according to the resonant frequency of microbubble, thereby leads to higher photoacoustic signal amplitude. The study of the mathematical modeling and the experimental design and detection of nonlinear PA waves can be helpful for photoacoustic signal enhancement with controllable generation and manipulation of microbubbles. The model yields optimization of PT/PA applications, imaging with higher resolution, and treatment of deeper tissues containing numerous microbubbles used in a diverse range of applications, killing of individual abnormal cells.

1.7. Thesis Outline

In Chapter 2, the laser sources for photoacoustic microscopy are compared in terms of pulse energy, wavelength tunability, and pulse repetition frequency. The design of a custom-made laser is described with some important stages such as oscillator and pre-amplifier, and supercontinuum generation, as well as the requirement of building a custom-made laser, is expressed in this chapter. Chapter 3 describes our photoacoustic microscopy system with custom-made fiber and commercial laser and includes the phantom studies. In this chapter, two photoacostic microscopy systems with two laser are described, and the evaluation of the performance of them is realized with the application of including cell suspension in PDMS based microfluidic devices. Chapter 4 develops the analytical methods for the characterization of cell morphology in microchannel flow. A combined Navier-Stokes and photoacoustic equation is investigated and the analytic solution including determinant parameters for the cell deformability such as plasma viscosity, density, and red blood cell aggregation, as well as involving laser parameters such as beamwidth, pulse duration, and repetition rate

takes part under its sections. Subsequently, the experimental method for the measurement of interaction force is described, and the results are analyzed. Chapter 5 represents the photoacoustic detection and confocal image of accumulation in vitro by using a novel design of microfluidic devices. Chapter 6 describes the bubble dynamics formed under CW irradiation and develops the analytical model for the influence of temperature rises due to the CW laser illumination on photoacoustic generation. The proposed analytical approach gives valid solutions for the experiment including photoacoustic enhancement through microbubble formation. Chapter 7 summarizes the results.

2. DEVELOPMENT OF A NOVEL FIBER LASER FOR PHOTOACOUSTIC MICROSCOPY SYSTEM

Photoacoustic microscopy (PAM) is a promising imaging modality that combines optical and ultrasound imaging. It takes advantage of high optical contrast and high ultrasonic spatial resolution owing to its hybrid nature. When a short laser pulse illuminates tissue, absorbed light leads to acoustic emission via thermoelastic expansion [13, 15–17, 71–76]. Generated ultrasonic waves are conventionally detected by transducers. Recorded signals are used to map the distribution of the locations of optical absorbers. Relatively low scattering of ultrasonic waves in biological tissues provides deeper penetration beyond the optical transport mean free path [17]. The contrast of PAM is endogenously produced by optical absorption of chromophores within the tissue [18, 77]. The laser system needs to produce short enough pulses, i.e., several nanoseconds, in order to generate photoacoustic signals efficiently and emit wavelengths in the visible range to cover absorption peaks of tissue chromophores in their spectra [14, 17, 78]. To obtain adequate penetration depth, it is also desirable to utilize a wavelength in the near infrared range, from 600 to 1200 nm, where biological tissues are relatively transparent [79, 80]. Several kinds of lasers have been used for photoacoustic imaging. Pulsed laser diodes draw researchers' attention by being compact and inexpensive. While the peak power is relatively modest [79, 81], it is sufficient to obtain adequate signal-to-noise ratio for in-vivo optical resolution photoacoustic microscopy (OR-PAM), as demonstrated in several publications [82–86]. On the other hand, they found only limited place in photoacoustic applications due to their lack of continuous tunability in wavelength. Q-switched Nd:YAG lasers operating at 1064 nm (and/ or acquiring 532 nm by frequency doubling) are frequently utilized for PAM [79, 86]. They are generally preferred because of their easy accessibility. However, their fixed wavelength output is a serious drawback for multispectral photoacoustic applications which quantify unique spectral features of each absorber by a set of wavelengths. On the other hand, Q-switched Nd:YAG pumped dye lasers, Ti:Sapphire lasers, and optical parametric oscillators (OPOs) are usually preferred for providing

necessary wavelength tuning with high pulse energies (> 1 mJ) [73, 74, 78, 87–95]; yet, they have some major limitations of their practical applications such as having low pulse repetition rate (generally less than 50 Hz, recently up to several kHz for OPOs [96, 97], being bulky and expensive, and requiring external cooling units [21]. For the sake of enabling spectroscopic measurements, multiwavelength spectrum is obtained from a single wavelength emitting Q-switched Nd:YAG microchip laser, either through stimulated Raman scattering (SRS) or nonlinear broadening by coupling its output to a fiber [98–107]. For lasers utilizing SRS, major energy is distributed on a series of fixed individual wavelength peaks that result from nonlinear interaction between incoming photons through the fiber and the molecules in the fiber itself, thus offers a limited wavelength tunability [108]. Koeplinger *et al.* [103] reported four bands in a polarization maintaining single mode fiber (PM-SMF), and Loya *et al.* [102] improved the system with a broader wavelength tuning range also with a higher repetition rate and pulse energy per band. It was also demonstrated that both discrete lines and a continuum can be produced by using four-wave mixing in a special fiber (SMF-28e) [104]. As a different technique, Buma *et al.* [105] used a birefringent optical fiber and produced discrete spectral bands in near infrared region. Much broader wavelength tuning can potentially be achieved by a supercontinuum source such as photonic crystal fiber (PCF), which relies on spectral broadening through nonlinear processes [98, 109–111]. PCF is a silica optical fiber with an ordered array of microscopic air holes running along its length [112, 113]. Billeh *et al.* [98] utilized PCF for developing spectroscopic photoacoustic microscopy system. Lee *et al.* [99] also built a supercontinuum laser system for both PAM and optical coherence tomography (OCT). Afterwards, Lee *et al.* [100] determined oxygen saturation of hemoglobin and hemoglobin concentration via the same laser source. Whensoever the applications by coupling the output of Q-switched Nd:YAG microchip to PCF are considered, energy per band is reported to be lower in supercontinuum case than SRS, which may be a drawback for many applications [108]. In order to achieve wider tunability in the wavelength with high energy per band, Shu *et al.* [101] proposed a master oscillator power amplifier (MOPA) laser system with a homebuilt ytterbium-doped (Yb) fiber amplifier for power boost. The amplifier was coupled to a specially designed PCF taper that connects a large-core

fiber that has a much more resistance to high-pulse energy at the input to a small-core PCF for spectrum broadening. Pulse energy per band increased dramatically and became comparable to the ones produced through SRS [101, 107]. Apart from wavelength tunability, a laser system with high pulse repetition frequency (PRF) is also desired for fast image acquisition. The repetition frequencies of solid-state lasers are limited up to several kHz; but recently, fiber lasers with high repetition rates emerge as an alternative excitation source for PAM. Through their high repetition rate, near real and real time imaging can be achieved [108, 114–116]. It has already been reported that in comparison to conventional systems with solid state lasers, the ones with fiber lasers are at least two orders of magnitude faster without compromising lateral resolution [114, 117]. Fiber laser sources are also used for in vivo and in vitro studies also including flow cytometry applications [114, 116–120]. The main disadvantage of these systems is their fixed wavelength that does not allow for multispectral functional imaging. To overcome the limitations, fiber laser technology seeking for tunability in wavelength is put forward. Hajireza *et al.* [120] developed an SRS fiber laser source for photoacoustic imaging. They coupled the output of an Yb fiber laser into a PM-SMF in varying lengths at different PRFs and extended the number of wavelengths at SRS peaks that were previously limited [108, 121]. In recent years, due to high power capabilities, MOPA laser systems have begun to be developed [122–124]. The first demonstration of a short pulse MOPA fiber laser at 1 μm was the study by Ilday *et al.* [125]. Allen *et al.* [122] produced a fiber laser system with a high repetition frequency in MOPA configuration with a single emission wavelength of 1064 nm. Mahmud *et al.* [123] demonstrated an OR-PAM system by using a commercial picosecond MOPA laser system consisting of a fiber-based tunable oscillator and three amplifier stages with a high power booster amplifier. However, the wavelength tunability was limited with 50 nm bandwidth. Here, to address the limitations of each approach, we develop a tunable fiber based MOPA laser system producing nanosecond pulses, covering spectrum from 450 nm to 1100 nm, specifically for PAM. The supercontinuum part is all fiber-integrated; guided-beam-propagation renders its misalignment free and largely immune to mechanical perturbations. Free space harmonic generation creates higher pulse energy for a specific band, i.e. 532 nm, and also generates ultra violet (UV)

light with wavelengths of 355 and 266 nm. Total supercontinuum output power is over 1 W and visible output power is around 270 mW at 65 kHz repetition rate corresponding to 4 μJ pulse energy. One of the novelties here is the improvement of wavelength tunability, output power and pulse energy when fiber-based lasers are benchmarked. This is the first demonstration of spectroscopic PAM by developing a supercontinuum all-fiber based MOPA source. The tunability of the laser parameters allows using only one laser for many different PAM applications, and also high repetition rate enables fast scanning. The coverage of near-UV spectrum gives an opportunity to image cell nuclei. As certain morphological changes such as size and shapes irregularities in the nuclei are known indicators of various cancers [126, 126, 127], we believe our system may also be useful for cell nuclei studies as well.

2.1. Design of a Custom-Made Fiber Laser

For photoacoustic microscopy system, a widely tunable fiber laser system is designed in MOPA configuration. Figure 2.1 shows the general scheme of the laser system. The output of MOPA configuration seeds two arms; the first one is used for supercontinuum generation via spectrum broadening and the second is for harmonic generation through nonlinear crystals. Pulses with sufficiently narrow bandwidths are required for harmonic generation (second, third, and fourth) [128] through nonlinear crystals. The increase in the length of the crystal results in more efficient wavelength conversion; yet, longer crystals bring along phase shifts proportional to the bandwidth of the laser, and decrease the efficiency [129]. For this reason, a 1064 nm fiber-coupled diode laser (I-IV Laser Enterprise) with a very narrow bandwidth (0.3 nm) is used and driven by a nanosecond diode driver (PicoLas, LDP – V03– 100 UF V3). Pulse width of the laser diode is adjusted through a field programmable gate array (FPGA) card (BASYS2, Xilinx). 15 ns long pulses at 65 kHz repetition rate are generated and sent to Yb-doped gain fiber after passing through an isolator and an amplified spontaneous emission (ASE) filter. As a pump source, a 976 nm laser diode (II-VI Laser Enterprise) delivering a maximum power of 540 mW is used. The pump is first passed through a pump protection filter with a maximum power handling of 300 mW, followed by a 30:70 coupler allotting two stages of preamplifier. In the first stage, Yb-doped fiber

is backward-pumped by 30 % of the output of the laser diode, then combined with the signal through a wavelength division multiplexer (WDM). Backward pumping is crucial for decreasing ASE generation rate, and hence preventing possible damage to the pump diodes and other fiber components. Another ASE filter is used between pre-amplifier stages to prevent the first from ASE that may be produced in the second. A WDM is used to combine 70 % of the output of the laser diode pump and the first stage of the preamplifier. For amplification, an Yb-doped fiber is used and the output power is measured as 170 mW at 65 kHz repetition rate. The last component of the second preamplifier is an isolator with a maximum power handling of 2 W in order to protect it from back reflections. At the end of the preamplifier, a 30:70 coupler separates the signal, 30 % is utilized for supercontinuum and 70 % is for harmonic generation. Polarization of light is crucial for frequency multiplication; thus, 70 % of the allocated signal is passed through a polarizer and all fiber components beyond this point are polarization maintaining. A 976 nm diode laser is used and a multi-mode pump combiner (MPC) combines the pump and signal. A polarization maintaining double cladding Yb-doped (PM-DC-Yb) fiber is spliced to the end of the MPC for amplification of the signal and pulses with 8 ns duration with an average power of 3 W at 65 kHz repetition rate are acquired. Figure 4a shows the optical spectrum and Fig. 4b shows the temporal profile of a pulse at the end of the amplification. In the temporal profile, the leading edge of the pulse is sharpened, or self-steepened, as the gain is partially saturated by each individual pulse and consequently less gain is available for the trailing edge. The temporal structure in the trailing edge is a static structure, which does not vary from pulse to pulse, originating primarily from the dynamically varying impedance of the semiconductor diode that seeds the system. Besides, 30 %of the signal having an average power of 45 mW is firstly amplified for supercontinuum generation, a 15 m long PCF (SC 5.0–1040, NKT) with 5 μ m core size is spliced to the end of Yb−doped fiber (Yb-1200 20/125 PM, nLight Liekki). The core size of the Yb-doped fiber is 20 μm which is larger than the core size of the PCF. For this reason, a special splice is used in between the Yb-doped fiber and PCF by a suitable splicer (FSM-100M, Fujikura). Figure 2.3a and b show the photograph of the output of supercontinuum and harmonic generation units, respectively. Optical spectrum of the

supercontinuum is measured by two optical spectrum analyzers (OSA) with different wavelength ranges; OSA 1 (Avaspec-3648-VIS, Avantes) and OSA 2 (QE65 Pro, Ocean Optics). The acquired spectra are digitally combined in a single Figure 2.4. In the first spectrum, the intensity of near infrared region appears lower than its actual level due to the decrease in the response of the analyzer while approaching to the edges of the measurable spectra region. It may also be caused by the difficulty of collecting all the beam with broad spectrum which is collimated by a single lens. Although the lens is an achromatic lens, it may still not be enough to eliminate slight divergence for different wavelengths and thus amplitude measurement variation throughout this broad spectrum range. In the second one, the intensity of the region between 450 to 650 nm lowered to noise level as a result of using neutral density filters in order to prevent saturation of the detector for the remaining spectrum.

For frequency multiplication process, a half wave plate is employed to match the polarization between the isolator and crystals. An anti-reflection coated (for 1064 nm wavelength) lens with a focal length of 30 mm is used to focus light into crystal. For SHG, a 20 mm long Lithium Triborate (LBO) crystal (Eksma, LBO-405) is used. For non-critical phase matching (NCPM), a crystal oven and a proportional–integral (PI) controller is added to maintain the temperature at 150.8 °C that results in maximum power. The light is passed through an anti-reflection coated (for 532/1064 nm) lens for collimation. Two dichroic mirrors separate the generated SHG beam (532 nm light) from the 1064 nm beam. Here, the output power is measured as 500 mW for 532 nm light. A mirror hold including a dichroic mirror reflecting 532 nm wavelength is added to the system. When the mirror is flopped, beam including 532 and 1064 nm wavelengths pass through a lens to enter a crystal (Eksma LBO- 407) for THG. The crystal is maintained at 40 °C for NCPM. The output power is around 3 mW for 355 nm light. Another flip mirror mount with a dichroic mirror that is transmitting 1064 nm and reflecting 532 nm beam is added to direct the beam toward a lens with a focal distance of 30 mm. This lens focuses the beam into a Barium Borate (BBO) crystal (Eksma BBO-700, thickness = 6 mm) that generates second harmonic of the 532 nm beam (fourth harmonic generation), which results in around 10 mW of 266 nm light. The output of the crystal is filtered via a dichroic mirror reflecting 266 nm light and
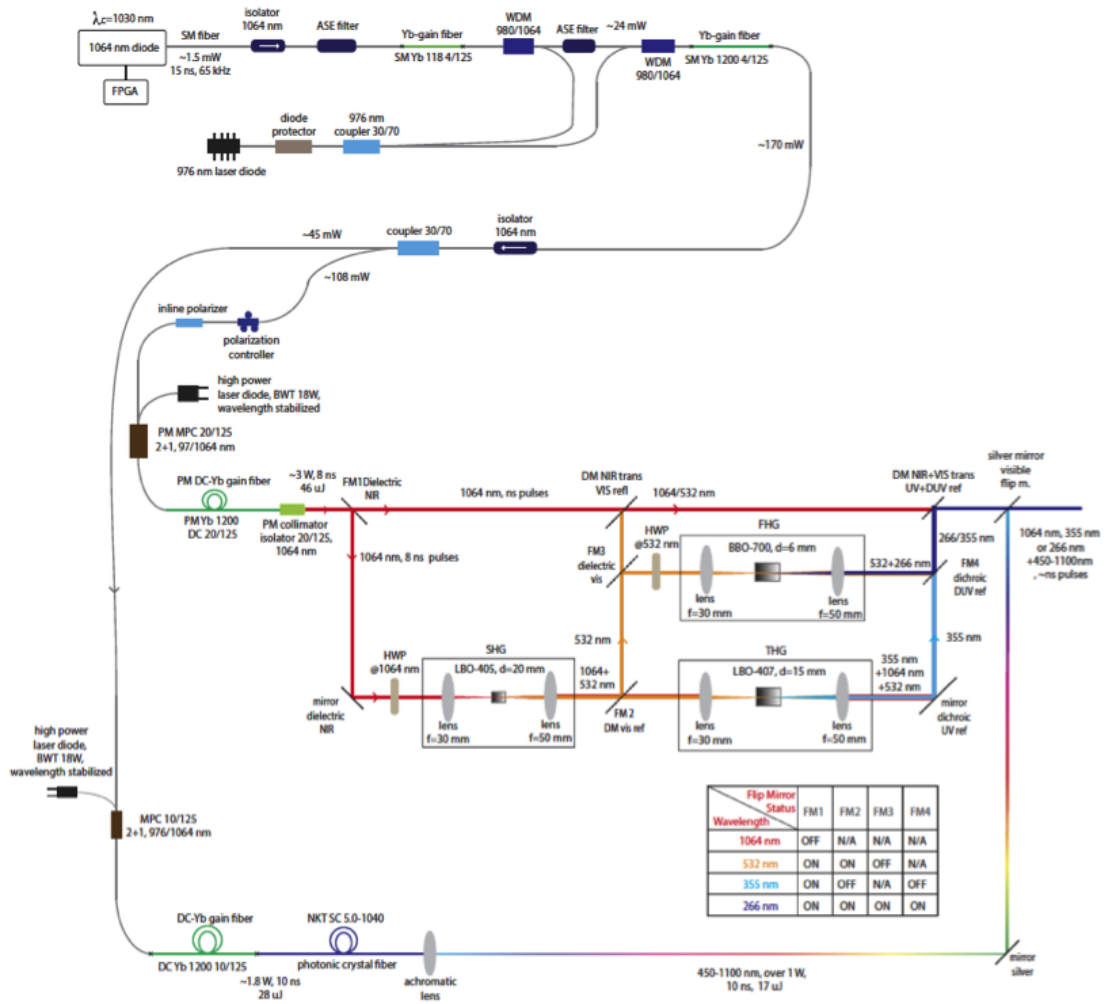
Figure 2.1. Schematics of fiber laser in MOPA configuration, all-fiber supercontinuum, and free-space harmonic generation units.
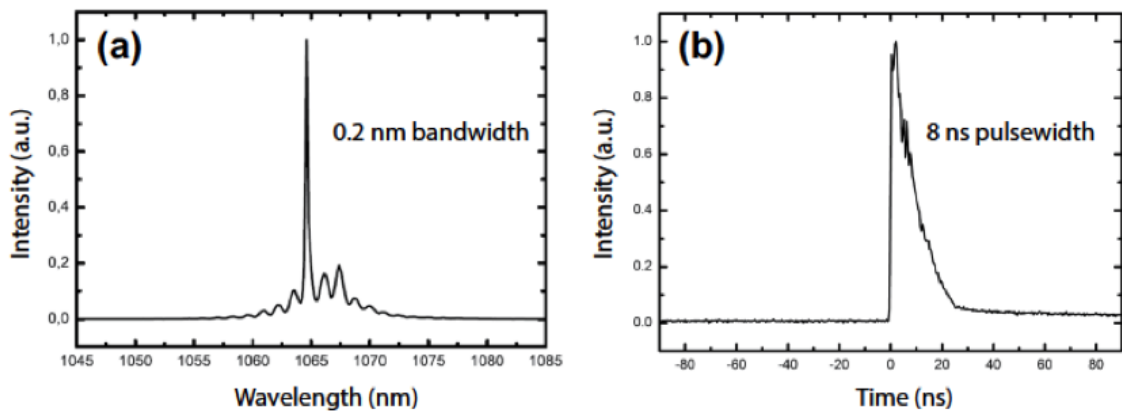
Figure 2.2. (a) Optical spectrum, (b) Temporal profile of a typical pulse at the end of PM-DC-Yb fiber.
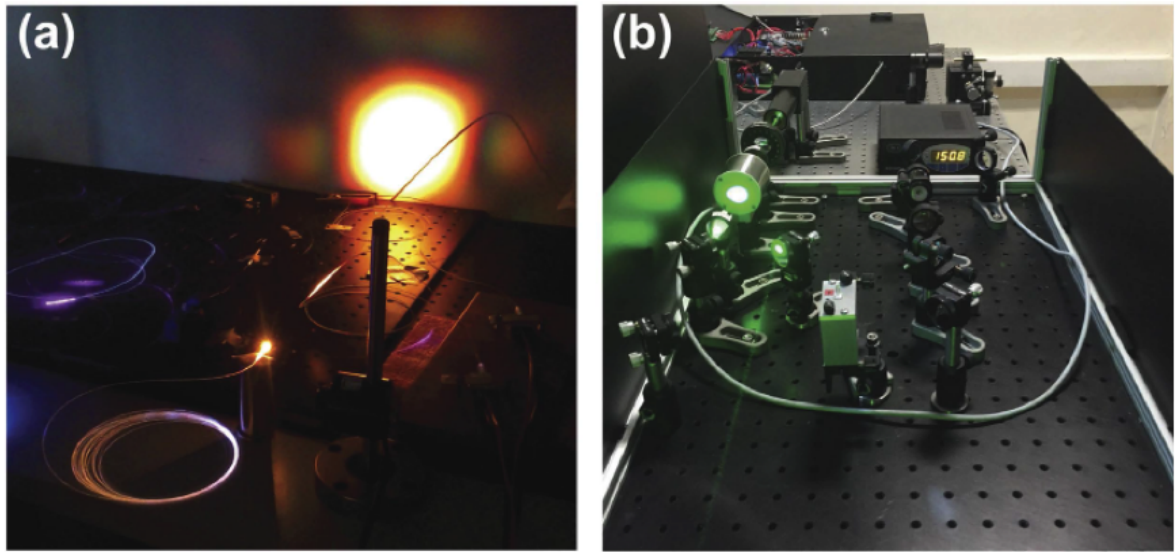
Figure 2.3. Photographs of the outputs of (a) supercontinuum, and (b) harmonic generation unit.

collimated by using a UV-coated lens with a focal distance of 50 mm. The optical spectrum of SHG is shown in Figure 2.4b and of THG in Figure 2.4c. The spectra are acquired with OSA 2 and OSA 1, respectively. Figure 2.1 shows the schematics of fiber laser in MOPA configuration, all-fiber supercontinuum, and free-space harmonic generation units.

The schematics of experimental setup for transmission mode OR-PAM system by using the irradiation source explained previously is shown in Figure 2.5. Pulse duration of the laser is 8 ns for harmonics generation output and 10 ns for supercontinuum port.

2.2. Evaluation of The Performance of Custom-Made Fiber Laser

A standardized resolution test target (USAF-1951, Thorlabs) was imaged for determination of the lateral resolution of our OR-PAM system. A transducer (V384, Panametrics) with a 3.5 MHz center frequency was used to acquire photoacoustic signals at the optical wavelength of 1064 nm filtered from the supercontinuum output. For focusing the light, a $5\times$ objective (LMH-5 $\times -$ 1064, Thorlabs) was used. The target was immersed in water, then 2D raster scanning by a motorized linear translation stage (LNR50SEK1, Thorlabs) along the x-y plane in steps of 1 μ m for an area of 300
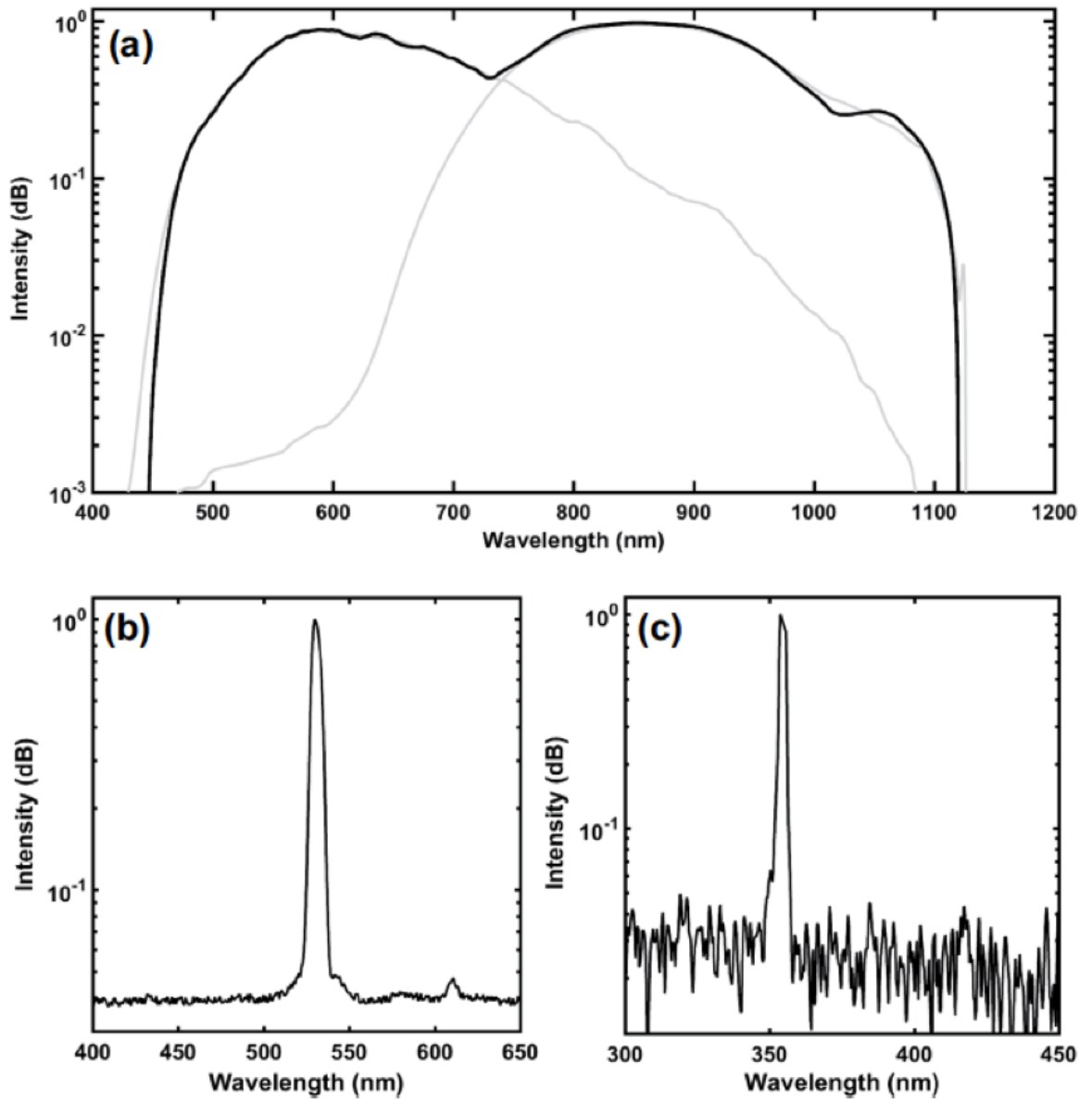
Figure 2.4. Optical spectrum of the (a) supercontinuum output (acquired by OSA 1 and OSA 2, respectively), (b) SHG (acquired by OSA 2), and (c) THG (acquired by OSA 1).
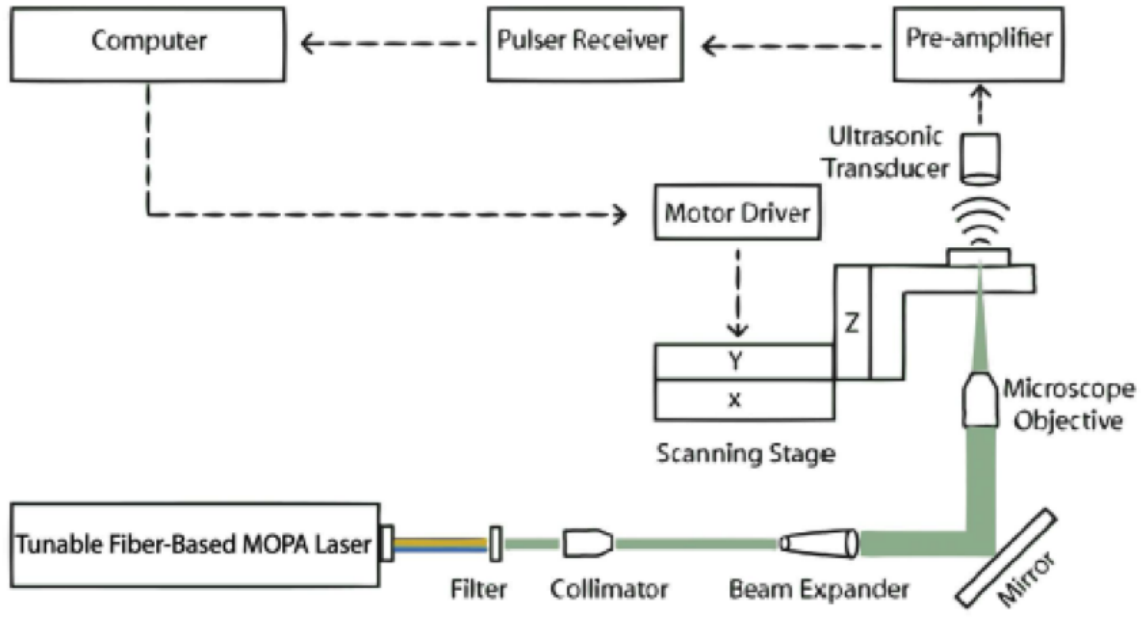
Figure 2.5. The schematics of experimental setup for transmission mode OR-PAM system.

$\times$ 330 μ m2 was performed. The acquired signals were averaged over 128 consecutive signal cycles. The trigger signal from the field programmable gate array (FPGA) of the laser was used to trigger a data acquisition card (DAQ) for synchronization. Following the triggering of each laser pulse, photoacoustic signals were initially amplified by 40 dB using a pre-amplifier (5678, 40 MHz bandwidth, Olympus) and then 39 dB via a pulser/receiver (5073PR, Olympus).

The signals were digitized through a DAQ (Razor Express CompuScope 1422, Gage Applied Technologies, Inc.), then data processing and reconstruction were performed. Figure 2.6a shows the optical microscopy image and Figure 2.6b presents the maximum amplitude projection (MAP) image of the scanned area (Group 6 and 7) of the test target. The lateral full width at half-maximum (FWHM) value from the imaged highlighted well resolved bars (Group 7, Element 6) was determined as 2.68 μ m, as shown in Figure 2.6d. Furthermore, for the demonstration of our multiwavelength PAM system, Group 5 Element 6 of the test target were also imaged with six different wavelengths of 532, 650, 697, 732, 785, and 880 that can be seen in Fig. 2a,b,c,d,e and f, respectively. These wavelength values except from 532 nm which was obtained by
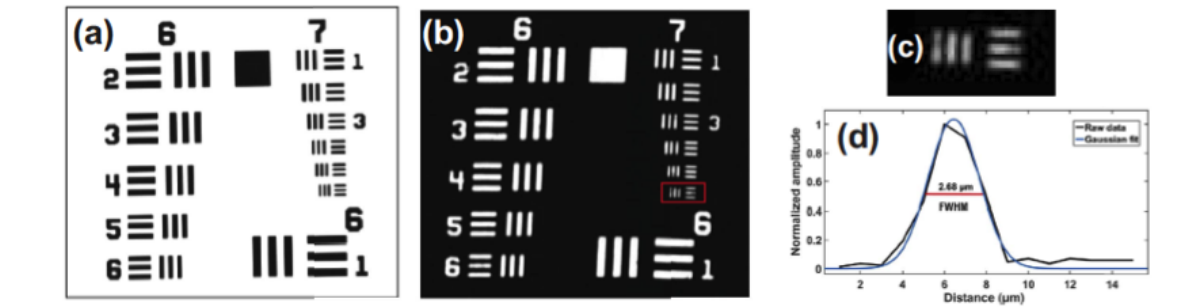
Figure 2.6. Figure 1. (a) Optical microscopy image, (b) Photoacoustic microscopy image of USAF resolution test target (Group 6 and 7). (c) Photoacoustic microscopy image of Group 7 Element 6. (d) FWHM of a line at Group 7 Element 6 from Gaussian fit (blue) of raw data (black).
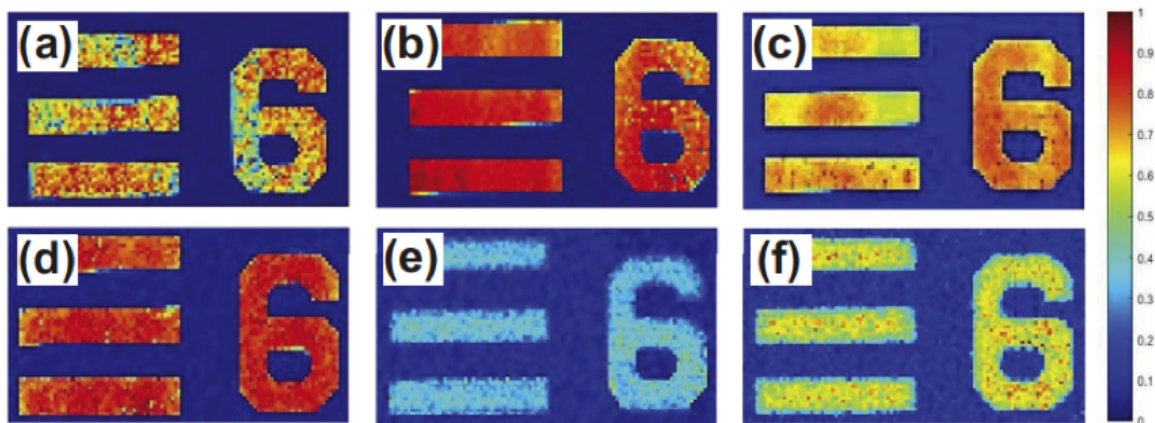
Figure 2.7. The PA image of Group 5 Element 6 scanned within an area of 56x101 μm^2 with steps of 1 μm acquired at optical wavelength (a) 532 nm from harmonic generation unit, (b) 650 nm, (c) 697 nm, (d) 732 nm, (e) 785 nm, and (f) 880 nm, respectively from supercontinuum output.

second harmonic generation (SHG), were filtered from the supercontinuum output of the laser for each experiment. A 10× objective (Plan Achromat, 0.25 NA, Olympus) was used to focus light to the relevant area.

In order to evaluate the performance of our laser system, pulse energy, average power and repetition rate values are compared with the ones in existing systems within the literature including fiber components and independent of seeding laser type.

Billeh *et al.* [98] sent the output of a Q-switched Nd:YAG microchip laser with a repetition frequency of 6.6 kHz to a 7 m-long PCF and reported seven wavelengths of 575, 625, 675, 725, 775, 825, and 875 nm with a bandwidth of 40 nm for each wavelength and pulse energies were measured as 7, 15, 24, 31, 31, 31, and 33 nJ, respectively. Lee *et al.* [100] also sent the output of the same type of laser to a 10 m-long PCF and stated pulse energy of the generated supercontinuum light as 500 nJ. The pulse energies of two bands, 500 to 560 and 560 to 660 nm were measured as 0.6 and 1.8 nJ, respectively. As can be seen, these pulse energies are quite low despite the wide bandwidths. There are many attempts to develop multiwavelength laser systems generating higher pulse energies from the output of an integrated fiber for various photoacoustic imaging applications [98, 101–103, 107]. However, this condition requires PCFs to withstand such high energies. Since non-linearity increases as the effective mode area of fiber gets smaller; thus, it is advantageous to decrease core diameter for generation of more efficient supercontinuum. Yet, energy per surface area of the fiber has a major effect on the maximum optical pulse peak power which a fiber can withstand [130–132]. Therefore, there is a trade-off between supercontinuum efficiency and energy to be coupled into the fiber. In order to overcome this limitation, tapered fibers are designed. Bondu *et al.* [107] used a nonlinear fiber that combines a large-core fiber for high-pulse energy handling with a small-core fiber for efficient spectral broadening. They used five different PCFs with varying core diameters, two of them were tapered for supercontinuum generation. They also demonstrated that total energy at the output of the straight PCF with core diameters of 5, 9, and 10 μm as 10, 29.5, and 30 μJ, respectively with visible output energies of 1.7, 5.4, and 4.6 μJ. Total output energy of tapered PCF of length of 1 m with an input core diameter

Table 2.1. Different types of lasers in terms of the pump laser, pulse duration, OW, MW, PRF, and fiber type. OW: Output wavelengths, MW: Wavelengths for which energy values are measured, and PRF: Pulse Repetition Frequency.

	Billeh *et al.* 2010	Lee et al. 2014	Shu *et al.* 2016 [32]	Bondu *et al.* 2016 [38]
Pump Laser	Q-switched Nd:YAG ML	Q-switched Nd:YAG ML	Q-switched Nd:YAG ML	Q-switched Nd:YAG ML
Pulse Duration (ns)	0.6	0.7	2	4
OW (nm)	500-1300	500-1700	500-2300	500-1600
MW (nm)	575, 625, 675, 725, 775, 825, 875	530-610	NA	Total Visible
Bandwidth (nm)	40	60-100	NA	NA
Energy (nJ)	7, 15, 24, 31, 31, 31, 33	0.6, 1.8	NA	4000
PRF (kHz)	6.6	21	25	1
Fiber Type	7 m PCF	10 m PCF	PCF Taper	15 m PCF Taper
Application	A phantom, consisting of black, blue, green, and, red ink	in vitro bovine blood mixture	in vivo mouse ear imaging	NA

of 10 μ m tapered down to 5 μm was stated as 22 μJ with visible output energy of 6 μJ [101, 107]. Different types of lasers which obtained techniques of SRS and four-wave mixing are summarized regarding the application in Table 2.1. Taking advantage of SRS inside a fiber is another method to increase the number of wavelengths from a fixed wavelength output. Polarization-maintaining single-mode fiber (PM-SMF) as well as PCF have been used for generation of SRS peaks [102, 103, 108, 120, 121]. Koeplinger *et al.* [103] sent the output of a Q-switched Nd:YAG microchip laser with a repetition frequency of 7.5 kHz to a frequency-doubling KTP crystal. Then, this output was sent to a 6 m long PM-SMF and acquired four distinct bands 546, 560, 574, and 600 nm with a pulse energy of 80 nJ for the each wavelength. Loya *et al.* [102] coupled the output of a Q-switched Nd:YAG laser operating at 30 kHz repetition rate to a 30 m-long large mode area photonic crystal fiber (LMA-PCF) and individual pulse energies were reported as 270, 360, 520, 530, and 400 nJ at wavelengths of 532, 546, 568, 589, and 600 nm, respectively. Table 2.2 illustrates several types of lasersin the literature which is related to non-linear broadening in a fiber , which obtained techniques of SRS and four-wave mixing.

Hajireza *et al.* [108, 120, 121] coupled an Yb-doped fiber laser into a PM-SMF in varying lengths at different PRFs and extended the number of wavelengths at SRS peaks. The acquired pulse energies were in between 100 to 500 nJ. Our tunable fiber-based laser system has three outputs; supercontinuum (from 450 to 1100 nm), 1064 nm from single-wavelength emitting port, and harmonic generation (532, 355, and 266 nm). The average power of 1064 nm output is around 3 W which seeds harmonic generation unit but also can be used for its own applications. The maximum average power values of SHG (532 nm), third harmonic generation (THG, 355 nm), and fourth harmonic generation (FHG, 266 nm) are 500, 3, 10 mW, respectively. Total output power of supercontinuum is measured over 1 W with visible output power around 270 mW with a powermeter (S314C, Thorlabs) at 65 kHz repetition rate that corresponds to 17 μJ total and 4 μJ visible energy. Various bandpass filters are used to obtain wavelength of interest from supercontinuum output and power measurements are performed to compare with the values in the literature. In order not to damage bandpass filters, a 1000 nm shortpass filter is firstly employed. Average power values at wavelengths of

Table 2.2. Comparison of the efficacy of several types of lasers which obtained techniques of SRS and four-wave mixing, in terms of the pump laser, pulse duration, OW, MW, PRF, and fiber type. OW: Output wavelengths, MW: Wavelengths for which energy values are measured, and PRF: Pulse Repetition Frequency.

	Koeplinger *et al.* 2011	Loya *et al.* 2012	Buma, *et al.* 2015	Ferrari *et al.* 2015
Pump Laser	Q-switched Nd:YAG ML	Q-switched Nd:YAG	Q-switched Nd:YAG ML	Q-switched Nd:YAG
Pulse Duration (ns)	0.6	1.8	0.6	2
OW (nm)	532, 546, 560, 574, 600	532-610	1064, 1100 1175, 1225 1275, 1375	532-900
MW (nm)		532, 546, 568, 589, 600	1064, 1097 1150, 1215 1275, 1325	532, 546 590, 600 650, 700 750, 800, 850
Bandwidth (nm)	NA	60-100	NA, 4 4.5, 10 20, 55	NA
Energy (nJ)	80	NA	1170, 250 390, 480 430, 200	up to 100
PRF (KHz)	7.5	NA	7.4	20
Fiber Type	6 m PM SMF	30 m LMA PCF	20 m PM SMF	100 m SMF 28e
Application	A phantom, consisting of red, blue	A phantom, consisting of red, blue	lipid phantom	dye phantom

680 and 830 nm with 10 nm bandwidths are measured as 5 and 11 mW by a powermeter (S142C, Thorlabs) after the achromatic lens that corresponds to 76 and 169 nJ pulse energy. For wider bandwidths, average power values for wavelengths of 650, 697, 732, 785, and 880 nm with 80, 75, 68, 62, and 70 nm bandwidths are 92, 93, 82, 84, 142 mW, respectively. Corresponding pulse energies are 1.4, 1.4, 1.3, 1.3, 2.2 μJ. These energies are higher than the ones produced through coupling the output of Q-switched Nd:YAG microchip laser to PCF which is at most 33 nJ [98]. As mentioned above, for the special case of tapered PCFs, visible output energy was reported as 6 μJ at 25 kHz, for our system that is 4 μJ at 65 kHz and comparable to that output 39,45. In addition to that, our laser source can provide higher pulse repetition rate, up to 1 MHz, at the expense of lower pulse energies. For the systems utilizing SRS, the energies per band were reported several hundreds of nJ with an utmost energy of 500 nJ [108, 121]. SRS peaks are produced with a bandwidth around 10 nm, pulse energies are higher than our system for such narrow bandwidths for visible region. However, when filters with wider bandwidths are selected, pulse energies become higher than ones that SRS peaks possess. To be also noted, pulse energies of SRS peaks decreases (estimated around 100 nJ) elongating near-infrared spectral region. The edge of peaks was noted as 788 nm46, our spectrum covers up to 1100 nm. Allen *et al.* [122], produced an all-fiber laser source with a PRF up to 2 MHz but the output wavelength was fixed. Mahmud *et al.* [123] also reported a fiber based laser source. By means of electronic modulations in the oscillator, tuning the repetition rate (0.1–120 MHz), the pulse-width (0.1–5 ns) and the wavelength (1030–1080 nm) were carried out. Green light was also generated through frequency doubling. The output power was reported up to 1.1 W and pulse energy up to 500 nJ. However, wavelength cannot be tuned in a broad range which does not allow for various spectroscopic photoacoustic applications. The efficacy of several types of lasers that employ pump laser as a fiber based and SRS in a fiber in terms of the pump laser is summarized in Table 2.3.

There are many other advantages of our system. All the laser parameters, which are reported as independently adjustable, could be achieved by changing FPGA configuration and currents to the pump diodes electronically without any mechanical intervention. The only exception to this is the switching among the supercontinuum and

Table 2.3. Comparison of the efficacy of several types of lasers that employ pump laser as a fiber based and SRS in a fiber in terms of the pump laser, pulse duration, OW, MW, PRF, and fiber type. OW: Output wavelengths, MW: Wavelengths for which energy values are measured, and PRF: Pulse Repetition Frequency.

	Hajireza *et al.* 2013	Hajireza *et al.* 2014	Mahmud *et al.*
Pump Laser	Yb-doped fiber laser	Yb-doped fiber laser	Fiber based laser (MOPA)
PD (ns)	1	1	0.1-5
OW (nm)	532, 543, 560, 590, 600	545, 550, 558, 570, 580, 590, 600	1030-1080 515-540
MW (nm)			1064
BW (nm)	10	NA	NA
E (nJ)	300-500	136, 76, 151, 21, 105, 213, 116	500
PRF (kHz)	40	160	100-120000
Fiber Type	3 m PM-SMF	6 m PM-SMF	NA
Application	A phantom, consisting of red, blue and in vivo imaging of a capillary network	A phantom, consisting of red, blue and in vivo imaging of a capillary network	A phantom study with carbon fiber

harmonic generation ports, which is achieved by a mechanically switchable mirror, that can also readily be motorized, if desired. In addition to this, it is very compact with dimensions of $40 \times 40 \times 9$ cm^3 except from free-space harmonic generation unit and does not require any big cooling unit. Thanks to its high PRF, it may be a promising source for cytometry as well [119]. To sum up, when all-fiber based laser systems are taken into consideration, the developed system improves the wavelength tunability with a repetition rate up to 1 MHz. For laser systems having fiber components, pulse energies of this system are higher from PCF coupled supercontinuum cases and comparable to the outputs of special tapered PCF designs. The system also offers all-fiber integrity and higher PRF by means of custom developed FPGA electronics that controls laser diode. Pulse energies of SRS peaks can be surpassed at near-infrared region with same bandwidth, at visible region only by using filters with wider bandwidths. This paper presents the potential of a tunable fiber laser system in MOPA configuration for multiwavelength OR-PAM. We believe that the system may provide the means of spectroscopic photoacoustic microscopy applications via widely tunable fiber laser technologies.

3. PHOTOACOUSTIC MICROSCOPY SYSTEM

A polydimethylsiloxane (PDMS) device modeled by a standard soft lithography has been used for the evaluation of the performance of the photoacoustic system for testing various contrast agents before in-vivo experimental tests. The PDMS phantom is composed of micrometric channels having the ability to form multilevel channel features with varying sizes and depths according to biological imaging targets. It can be defined as a stable physical and tissue-simulating phantom with tunable optical properties when agar based phantoms are considered. Furthermore, it has suitable optical and acoustic, non-toxic material related properties during the preparation and application [40, 41].

3.1. Phantom Studies with Fiber Laser

For fiber-laser-based photoacoustic microscopy, we used various types of microfluidic devices made using soft lithography, as shown in Figure 3.1 and 3.2.

In order to evaluate the performance of fiber laser regarding the selection wavelength, adjusting pulse energy, and its stability, as well as to test several microfluidic devices in terms of image quality parameters such as signal to noise ratio (SNR) and
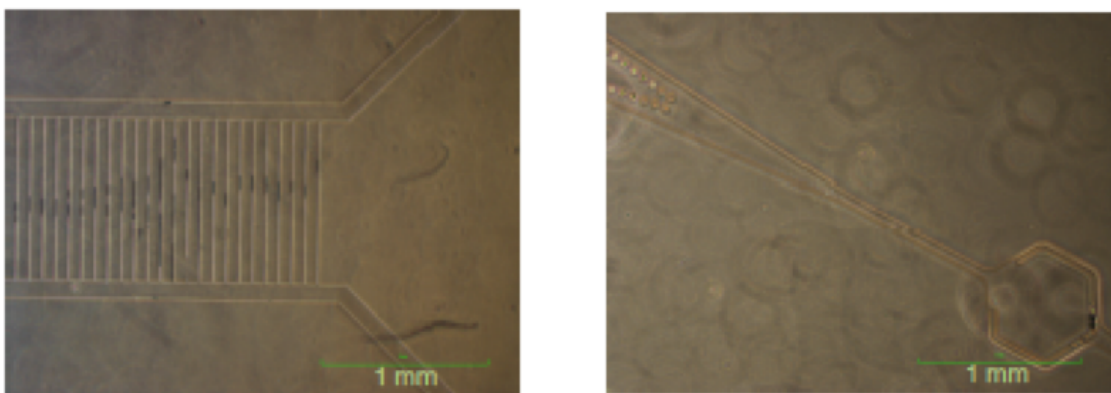
Figure 3.1. Optical microscopy images of two chip designs.
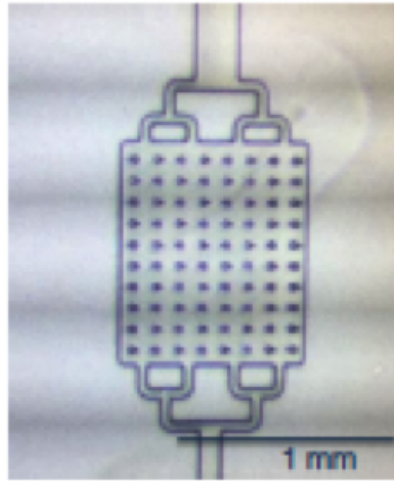
Figure 3.2. Optical microscopy image of chip design.

contrast (C), the devices which are two different in thickness were used for photoacoustic imaging. The PDMS thickness of 6 mm microfluidic device was prepared by adding black ink, and the photoacoustic image of the PDMS phantom loaded with black ink can be seen in Figure 3.3. In order to acquire photoacoustic signals, a water immersion transducer with a center frequency of 3.5 MHz was used. In this work, the wavelength of 1064 nm was filtered from the supercontinuum output, and output power at this wavelength was optimized by neutral density filters (10 mW). As can be seen in the Figure 3.3, the lateral resolution is estimated to be around 5 μm, because of the fact that the pillars can hardly be distinguished and the dimension of the pillars was measured as 5 μm. Note that the photoacoustic image was obtained for scanning an area of 4×1 mm^2.

For the second study of the performance testing of both fiber laser and the microfluidic devices, the image of the PDMS phantom consisting of red blood cells suspended in plasma was obtained with our photoacoustic system. Figure 3.4a shows the photoacoustic image, scan area=600×600 μm^2, was obtained by using a transducer with a 10 MHz center frequency. For the comparison, the images are shown in Figure 3.4b and Figure 3.4c were taken from CCD and optical microscopy images, respectively.
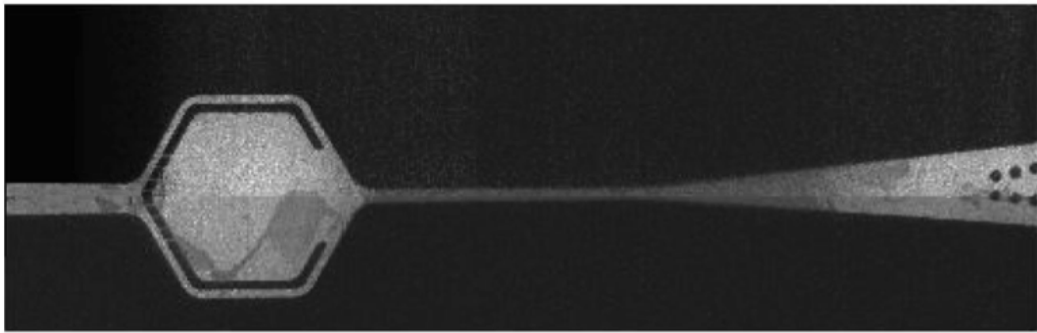
Figure 3.3. Photoacoustic image of a microfluidics device loaded with black ink (4 mm x 1 mm).
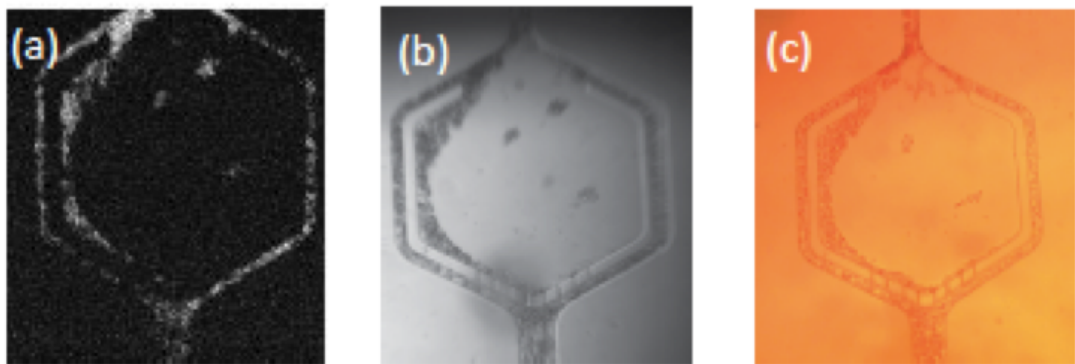
Figure 3.4. (a) Photoacoustic image (b) CCD image (c) Optical microscopy image of a microfluidics device loaded with red blood.

For the third study, two PDMS phantoms were filled with different concentrations of SKMEL-28 (malignant melanoma). We aim to reveal the evaluation of PA signal produced by these phantoms with different concentrations of SKMEL-28 exhibited the largest amount of a precursor of melanin. For this purpose, we use an all-fiber tunable optical source based on a high repetition rate nanosecond custom fiber-laser with unique supercontinuum (600-1100 nm) property. The laser enables for a spectral separation of signals from different absorbers based on their characteristic absorption spectra. It can be used for functional imaging. The PDMS phantom not only can be used as a phantom to assess the performance of the PA system but also used for a better understanding of characteristics of the PA signal produced by different cells in vitro. This proof of concept gives insights on various biomedical and clinical applications of photoacoustic imaging via PDMS device.

SKMEL 28 which is a melanoma cell line was obtained from the American Type Culture Collection (ATCC). Cells were grown in Dulbecco's modified Eagle medium (DMEM) containing 10 % fetal bovine serum (FBS). MEM Non-Essential Amino Acids Solution and Penicillin-Streptomycin mixture were added to the medium to increase cell growth and viability and prevent contamination, respectively. For cell maintenance, cells were cultured on 100 mm tissue culture dishes with 10 mL growth medium at 37 °C in a 5 % CO^2 humidified atmosphere and cell passage was performed with 0.05 % trypsin with EDTA every two days. Before taking measurements at multiple wavelengths for spectral separation of signals from skmel28 cell line based on their characteristic absorption spectra, various cell lines used for this thesis were tested with some methods such as standard Western Blot analysis as well as plate reader.

3.1.1. Western Blot analysis

The cells were collected and washed with PBS three times. The cells were suspended with protein lysis buffer. The cell suspensions were incubated on ice for 30 min. The suspensions were centrifuged at 13000 rpm at 4 °C for 30 min and supernatants were collected into new tubes. Total protein concentration was measured with BCA assay. Then, cell lysates were mixed with 5x protein loading dye and heated at 95 °C
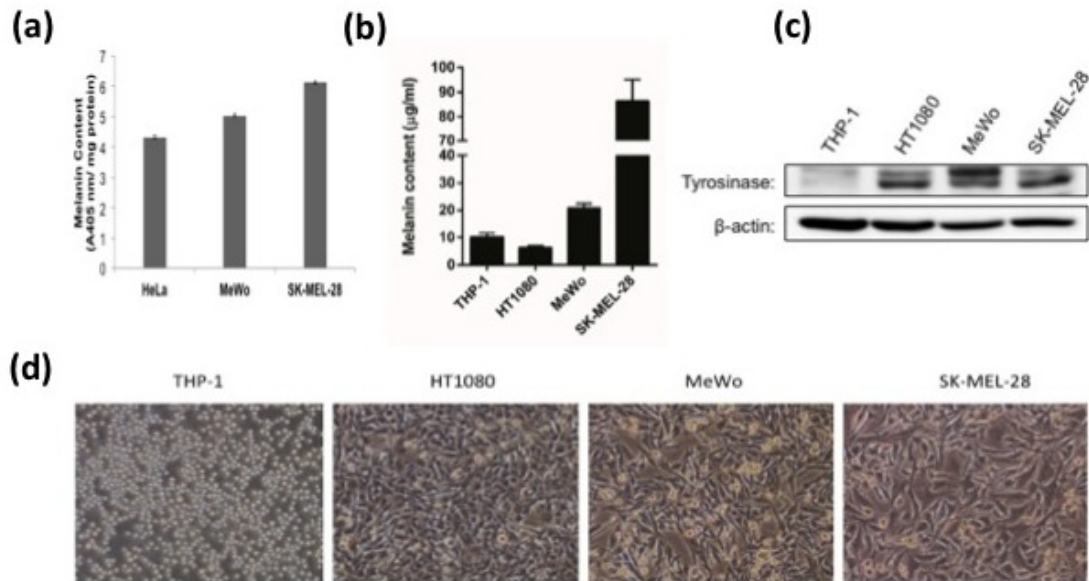
Figure 3.5. (a) the melanin content in different cell lines ((a) HeLa, MeWo, SK-MEL-28), ((b)Thp-1, Ht1080, MeWo, SK-MEL-28) measuring via a microplate reader, (c) Western blots of the induction of melanoma cell differentiation, (d) Thp-1, Ht1080, MeWo, Skmel28, MeWo, HeLa cell image of optic microscope, respectively.

for 10 min. The samples were run into 10 % polyacrylamide gels and proteins were blotted on PVDF membranes. The membranes were blocked with 5 % non-fat milk in TBS-T at a room temperature for 2 hour on an orbital shaker. The membranes were washed with TBS-T for 5 min three times. Then, the membranes were incubated with primary antibody at 4 °C overnight. Next day, the membranes were washed three times with TBS-T and incubated with the secondary antibody at room temperature for 2h. After incubation of the secondary antibody, the membranes were washed again. WesternBright ECL-HRP Substrate was used to visualize the protein bands. The substrate was prepared by mixing two solutions in 1:1 ratio, then the membrane was incubated with the substrate for 1 minute at dark. Visualization of the membrane was performed in SynGene imaging device. For analyses of Western Blotting, the intensity of protein bands was calculated by Image J. repeated at least 3 times with different biological replicas. B-actin was used as loading control. The Figure 3.5c shows that the skmel28 has the highest levels of tyrosinase.

3.1.2. Melanin content assay via plate reader

10^6 cells were collected and washed with PBS three times. The cells were suspended with 1N NaOH containing 10 % DMSO. The cell suspensions were incubated at 80°C for 1 hour. Then, intracellular melanin contents were calculated by measuring OD450 values of samples and standards with a plate reader. Synthetic melanin was used as standard (N=3, Mean+SD). The Figure 3.5a-b shows that the skmel28 has the highest melanin content. For the first study about measuring melanin content via plate reader, HeLa was used as a control group, shown in Figure 3.5a. For the second study about measuring melanin content via plate reader, synthetic melanin was used as a standard, shown in Figure 3.5b. The same results were obtained with the help of different control groups.

For loading of PDMS, SK-MEL-28 cells were counted using Countess II FL Automated Cell Counter with a hemocytometer. In order to prepare a certain concentration of cells, counted cells were centrifuged at 2000 rpm for 2 minutes and diluted with the corresponding volume of PBS. The PDMS microfluidic device is composed of six parallel channels. The central regions of the channels have a hexagonal shape. Each hexagonal unit cell has inner cells and outer cells arranged in a hexagonal symmetry, which mimics in vivo microenvironment. The fourth channel was filled with India Ink (Dr. Ph. Martin's Bombay Black, Salis International Inc., Golden, CO). Four channels (1st, 2nd, 3rd, and 6th) were filled with SK-MEL-28 cells in the concentration of $30x10^6$ cells/ml, and only one channel (5th) was filled with SK-MEL-28 cells in the concentration of $20x10^6$ cells/ml. In order to inject ink and cells into the channels, diabetic needles were used. After loading, all channels were sealed with nail polish as can be seen in Figure 3.6a. In this study, a 1 mm by 1 mm area of the test phantom shown in Figure 3.6c was scanned and the photoacoustic image in Figure 3.6e was obtained. We have reported that the higher concentration of SK-MEL-28 melanoma cells in the PDMS channel produced a detectable photoacoustic signal in which amplitude was dependent on the number of cells, as shown in Figure 3.7. Here, each signal was acquired at the same using wavelength of 532 nm with output power of P = 50 mW. The PDMS phantom not only can be used as a phantom to assess the performance of
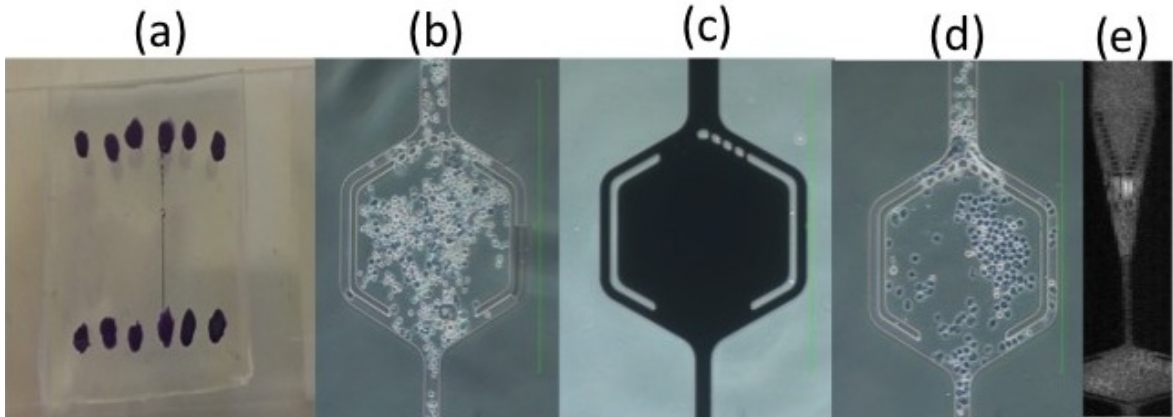
Figure 3.6. The photograph of the PDMS phantom. Four channels were filled with SK-MEL-28 cells in concentration of 30x106 cells/ml, and only one channel (5th) was filled with SK-MEL-28 cells in concentration of 20x106 cells/ml) (B) 3rd, (C) 4th and (C) 5th channel image of optical microscope, respectively.

photoacoustic (PA) system but also allows for a better understanding of characteristics of PA signal produced by different cells in vitro. This proof of concept gives insights on various biomedical and clinical applications of photoacoustic imaging via PDMS device.

Moreover, two types of microfluidic devices made of different PDMS thickness are produced a different signal to noise ratio when the PDMS phantoms loaded with a black ink were scanned. The signals are shown in Figure 3.8. The Figure 3.8A and 3.8B are acquired by the PDMS phantom with the thickness of 6 and 1 mm, respectively. The measurements of the SNR of photoacoustic signals generated in microfluidic channels composed of thinner PDMS is higher than the other one, as can be seen in Figure 3.8.

3.2. Phantom Studies with Optical Parametric Oscillator (OPO) lasers

We build the photoacoustic system with OPO laser for taking advantages of large wavelength tuning range and delivering high pulse energy to the sample. Figure 3.9 illustrates an experimental configuration of our multispectral photoacoustic microscopy PAM system which employs a wavelength-tunable OPO laser (Continuum, Surelite II; pulse duration: 6 ns; wavelength coverage: 192-2750 nm; repetition rate: 1-10
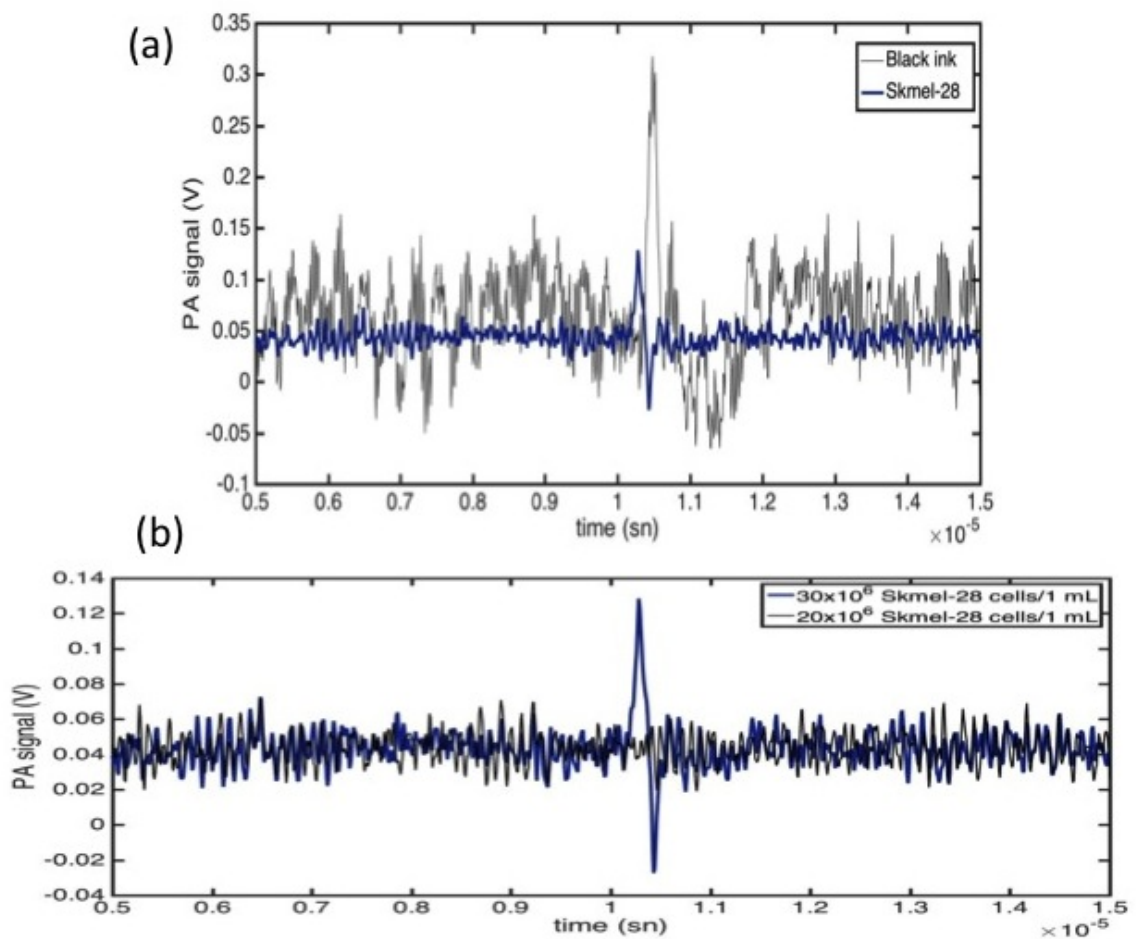
Figure 3.7. (a) The PA signals generated by black ink and higher skmel28 concentrations vs time, (b) the PA signals obtained from different concentrations of skmel28 melanoma cells.

Hz). Moreover, Figure 3.10 shows the experimental set-up used in our multispectral photoacoustic microscopy with OPO laser. For photoacoustic imaging, the output laser beam was reshaped by an iris of 6 mm diameter due to the non-uniform beam shape, and attenuated by a neutral density filter. After attenuated by neutral density filter, the light beam was expanded to reach a beam diameter of 8 mm by a beam expander. The expanded beam was coupled into a multi-mode optical fiber using a reflective collimator (RC08APC-P01, Protected Silver Reflective Collimator, 450 nm - 20 μm, Ø8.5 mm Beam, Thorlabs). Then, the output beam from the multi-mode fiber (M74L01 - Ø400 μm, 0.39 NA) entered the second collimator, and the collimated beam was directed into 2D galvonometer scanner (Raylese). A PC-controlled (scan-controlling PC) analog-output board (PD2-AO-16, United Electronic Industries) was synchronized with the laser triggering and a two-dimensional scanning galvanometer. The energy of each laser pulse was recorded using a beam sampler (BSF-A; Thorlabs, Newton, NJ, USA) and an energy meter (PE25-C; Ophir Optics, Jerusalem, Israel) to compensate for the fluctuation in laser intensity. While using the system including a fiber coupling scheme with a beam homogenizer, we noticed that output fiber energy was limited, and the energy was not sufficient to generate PA signals from smart probes. Moreover, the existing two-dimensional scanning galvanometer did not reduce scanning time in the absence of an array transducer since the PRF of the OPO laser was low. For adjusting nearly Gaussian beam shape, we changed our system by using two pinholes placed at before and after beam expander instead of using mlti-fiber. The generated acoustic pressure waves by the actively and inactively targeted contrast agent were detected by 3.5-MHz unfocused ultrasonic transducer. The induced photoacoustic signals were amplified using by 40 dB using a pre-amplifier (5678, 40 MHz bandwidth, Olympus) then 39 dB via a JSR Ultrasonics DPR 500 (Imaginant,. Pittsford, NY) pulser/receiver. The amplified signals were digitized through a DAQ using a data acquisition card (Express CompuScope 24G8, 2 channels, 4GS/s sampling max, 2 GS memory).
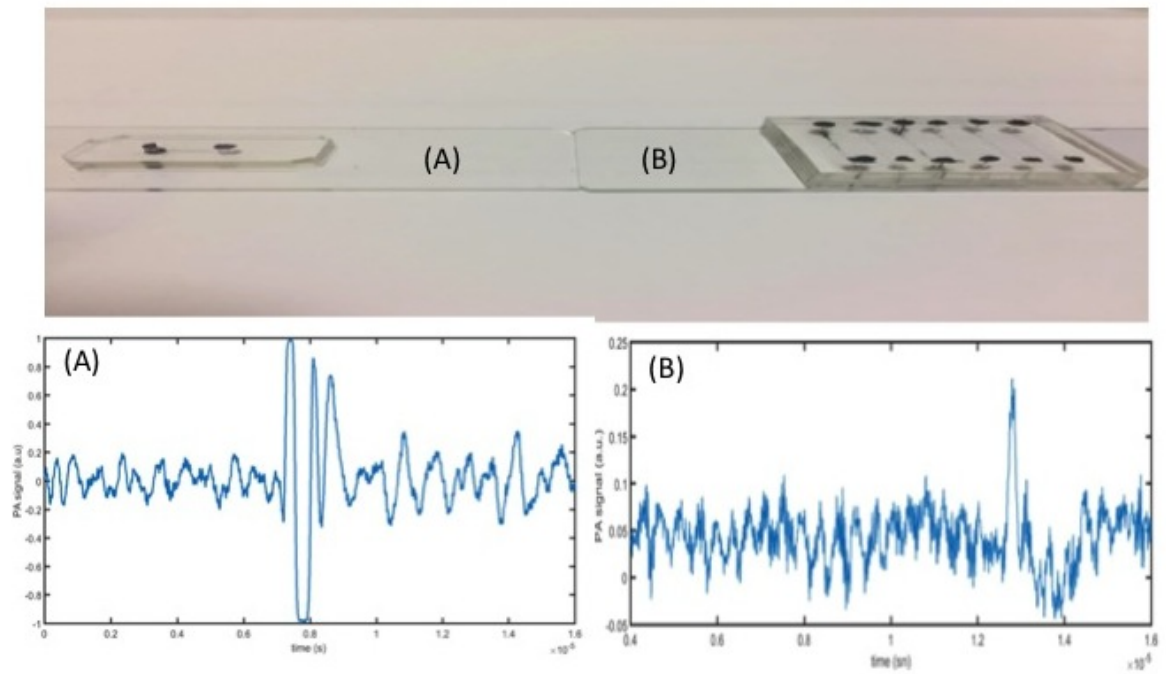
Figure 3.8. (A) The photograph of first design chip based PDMS thickness of 6 mm, (B) of second design chip based PDMS thickness of 1 mm and the resultant photoacoustic signal obtained by (A) and (B) phantom.
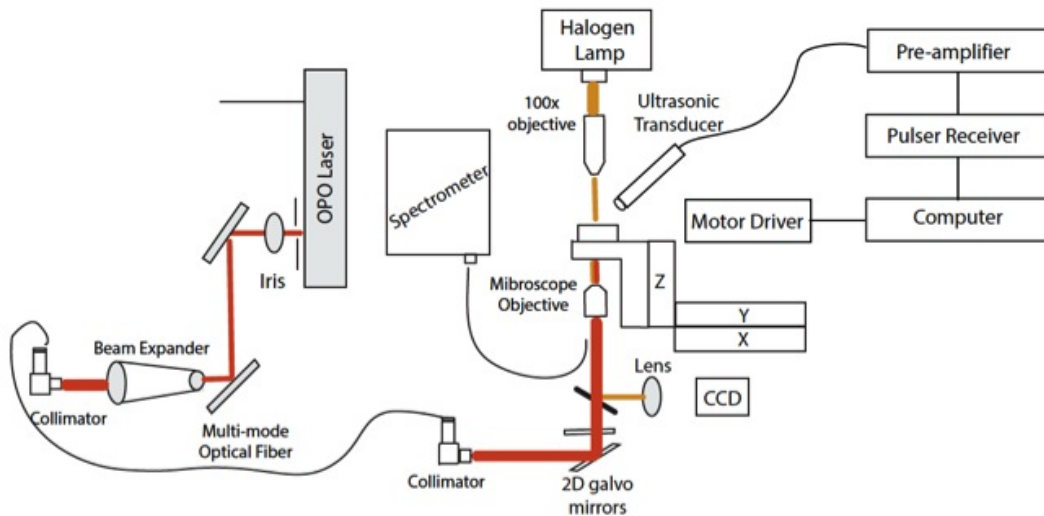
Figure 3.9. The schematics of experimental setup for multispectral transmission mode OR-PAM system with OPO laser.

After the completion of the whole alignment for our system, the laser pulse energy variations were monitored by using a Gentec power meter to acquire the average pulse energies of several output wavelengths, which was summarized in Table 3.2. For the routine quality control and performance evaluation of photoacoustic imaging instruments, the imaging optimization studies were performed with the use of blood phantoms. First, the generated holes in agar phantom shown in Figure 3.11a were filled with blood suspension and black inks, and the photoacoustic image over 0.6×4 mm^2 area of the hole (shown in Figure 3.11b) in the x–y plane was obtained using the 630 nm wavelength with pulse energy of 1 mJ, as shown in Figure 3.11c. To ensure the reconstruction of the image, the signals acquired were analyzed in both time and frequency domain. Figure 3.12 shows the plots of two signals in the time domain and their frequency spectra coming from blood suspension. At the same time, this figure represents different characterizations of PA signals originating from two different RBC
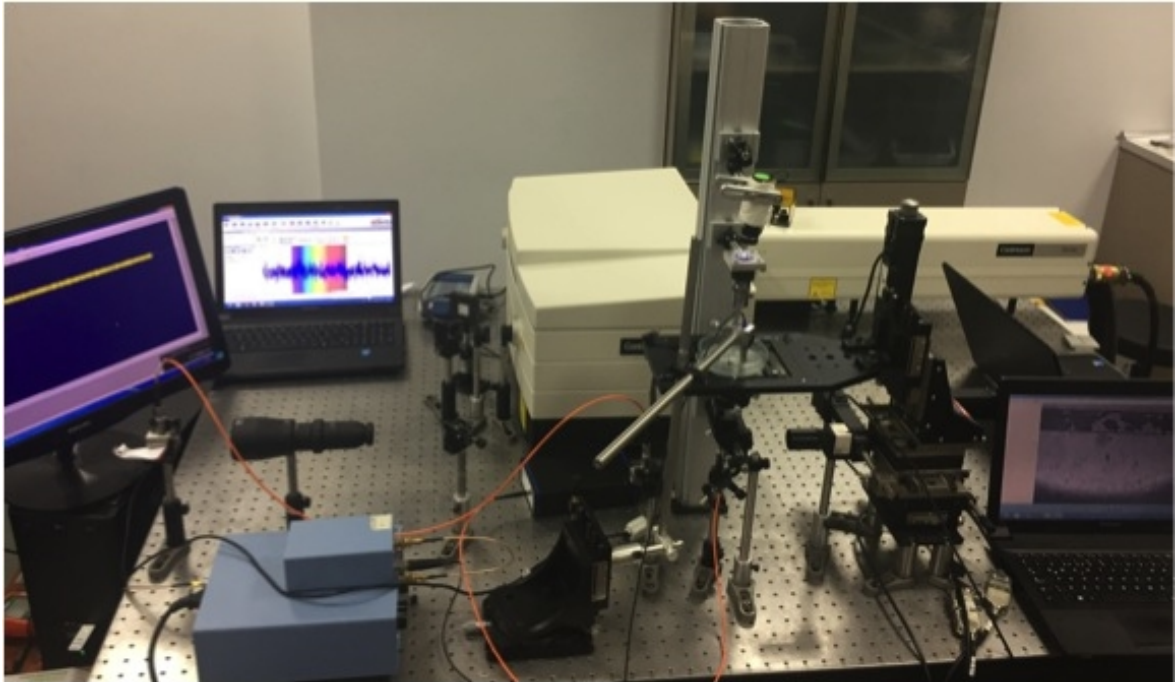
Figure 3.10. The photograph of experimental setup for multispectral transmission mode OR-PAM system with OPO laser.

clusters. Our second blood phantom study was carried out using PAM system with OPO laser. In this study, a novel PDMS device bonded to the petri dish was tested. Bonding the novel PDMS device benefits the system from two main aspects. First, it leads to usage of water immersion transducer, since the petri dish is used as a water tank, as well as enables to acquire PA signal at the same focal point. The PDMS phantom composed of 6 parallel channels with varying dimensions, 100 μm to 1 mm (100, 100, 500, 500, 300, 300 μm) were used in this study. The blood suspension was loaded into the channel with 100 μm by using tubing with appropriate fittings and both the inlet and outlet of the channels were sealed with nail varnish shown in Figure 3.13 a-b. The image of the channel which mimicking the blood vessel was obtained by CCD camera shown in Figure 3.13d and the photoacoustic image was acquired by scanning the area 60μm x 600μm as can be seen in the Figure 3.13d.

Moreover, we prepared two phantoms by molding 1 % of agarose gel. (Sigma-Aldrich, St. Louis, MO, USA). The microtiter plate (Figure 3.14a) was embedded in a container filled with 1 % agarose gel. In order to generate holes, the microtiter plate was pulled out. The first phantom includes the microtiter plate filled with different

Table 3.1. The wavelengths and average pulse energies of OPO laser.

Wavelength (nm)	Power (mJ) (First Measurement)	Power (mJ) (Second Measurement)	Avarage Power (mJ)
532	0.13	0.14	0.135 mJ
555	0.16	0.17	0.165 mJ
600	0.12	0.17	0.145 mJ
630	0.12	0.22	0.170 mJ
680	0.08	0.097	0.088 mJ
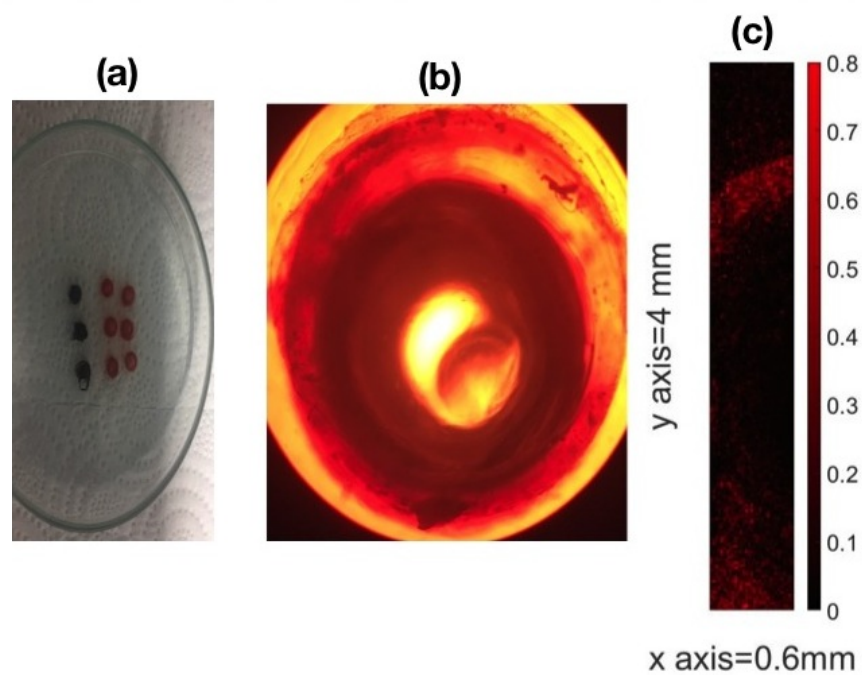
Figure 3.11. (a) The photograph of the agar phantom consisted of black ink and blood suspension, (b) the photoacoustic image, (c) the optical microscopy image obtained from the blood suspensions.
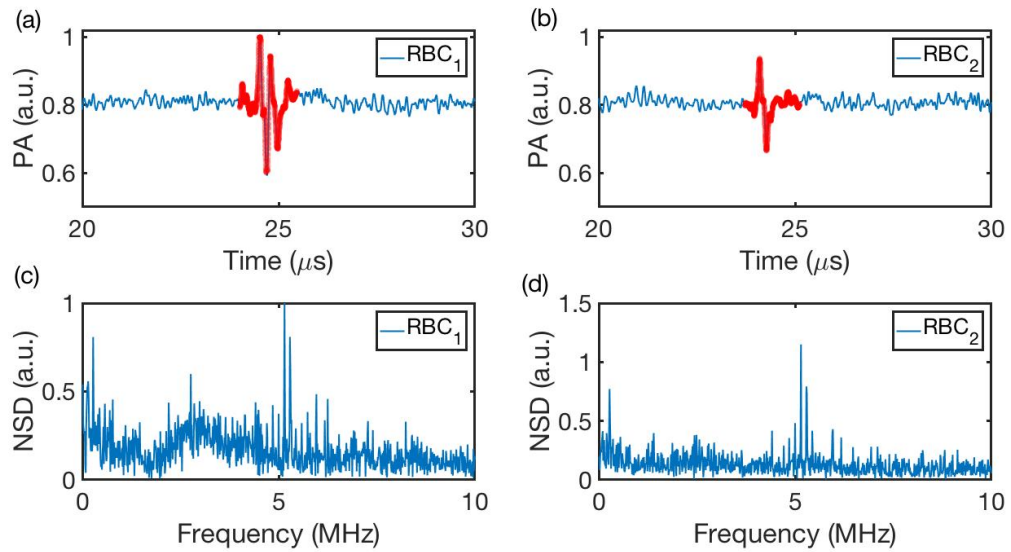
Figure 3.12. Normalized PA wave generated by (a) first (b)second RBC clusters vs time, and the frequency spectra of (c) the first (d) the second RBC clusters, an ultrasonic detector was located at position 3 mm (approximately)
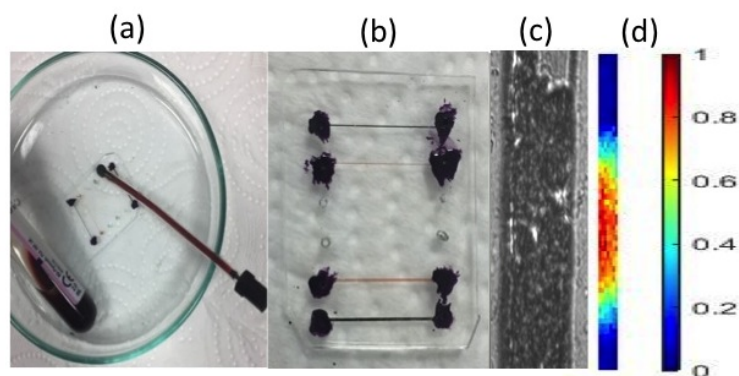
Figure 3.13. The photograph of PDMS phantom while the blood suspension was loaded into the channel with 100 μm by using tubing with appropriate fittings, (c) the photoacoustic image obtained from the blood suspensions
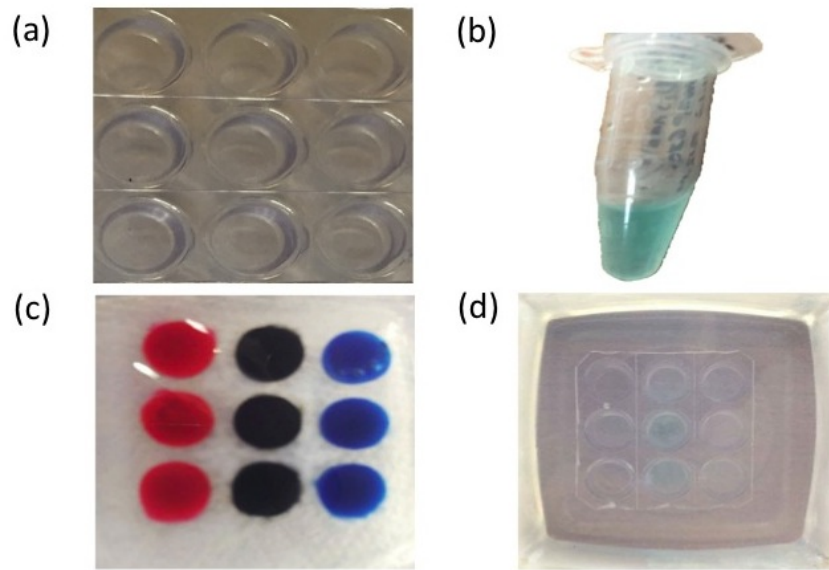
Figure 3.14. The photograph of (a) microtiter plate, (b) MMPSense680 contrast agent, (c) the phantom containing black, red, blue dyes, (e) the phantom containing MMPSense680 contrast agent.

dyes such as Dr. Ph. Martin's Bombay Black, Red, Blue (as shown in Figure 3.14b). MMPSense-680 probe as shown in Figure 3.14b (which is explained in Chapter 5) suspended in 1 % agarose was filled into the part of holes in the second phantom (as shown in Figure 3.14d). Then, the surfaces of both phantoms were covered with 1 % agarose gel. To determine the optimum power for generating the photoacoustic wave, the PA signals were recorded instead of scanning phantom.

The efficacy of multiwavelength photoacoustic imaging was performed for a highly selective and sensitive detection of cancer cell lines. The Figure 3.15 illustrates the photograph of an agarose phantom and detector when the laser is operated at a 532 nm wavelength. The optoacoustic image of skmel28 inserted in an agar phantom was obtained at two wavelengths (600, 630 nm). The scanned area of cancer cell line suspended in an agarose phantom and of agar was 4 mm × 4 mm and 2 mm x 0.2 mm, respectively, shown in Figure 3.16. Figure 3.17a-b represents the PA signals obtained at the different points, the signals in Figure 3.17c-d were represented in the frequency domain. Figure 3.18a shows the images obtained by a section of the sample image which is illustrated in Figure 3.16. The experiment was repeated, and the images taken by
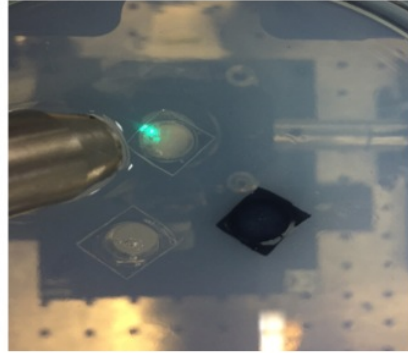
Figure 3.15. The photograph of agorose phantom with different compositions.
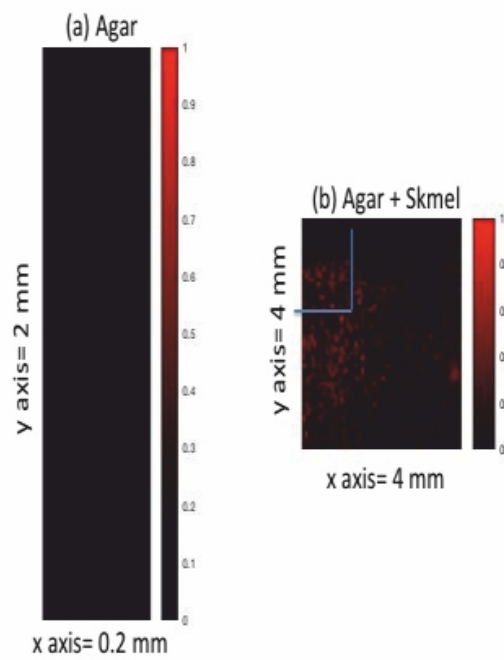
Figure 3.16. Photoacoustic image of the phantom containing (a) only agar (b) skmel28 cell pellet inclusions at 600 nm.
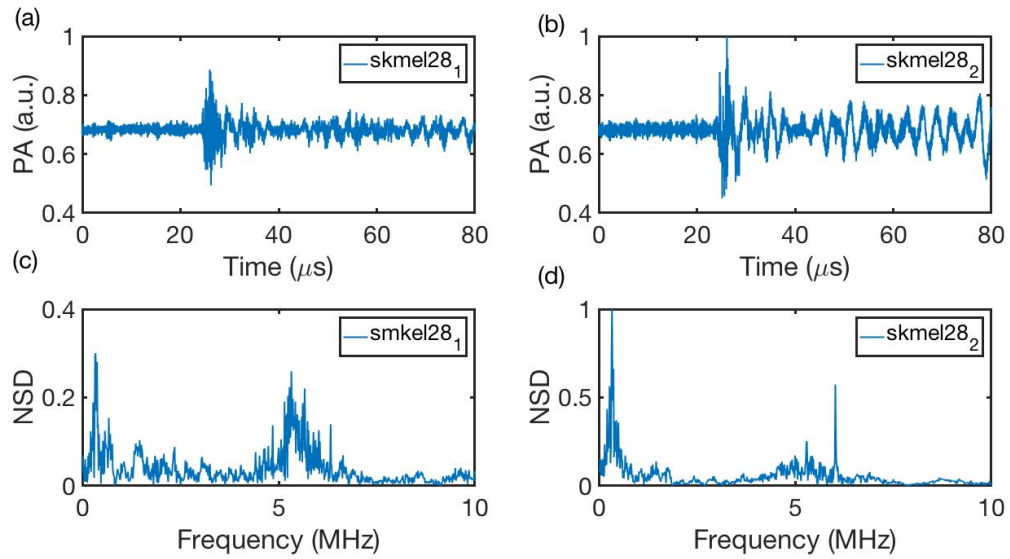
Figure 3.17. Normalized PA wave generated by (a) first (b) second skmel28 clusters vs time, and the frequency spectra of (c) the first (d) the second skmel28 clusters, an ultrasonic detector was located at position 3 mm (approximately)

same region were compared in order to find out the necessary power for collecting photoacoustic signal and to represents pulse-to-pulse fluctuations in the output power of an excitation laser, shown in Figure 3.18b. Here, the output pulse energy was 3.6 μJ. Furthermore, Figure 3.18 represents the comparison of relative photoacoustic images obtained at different wavelengths.
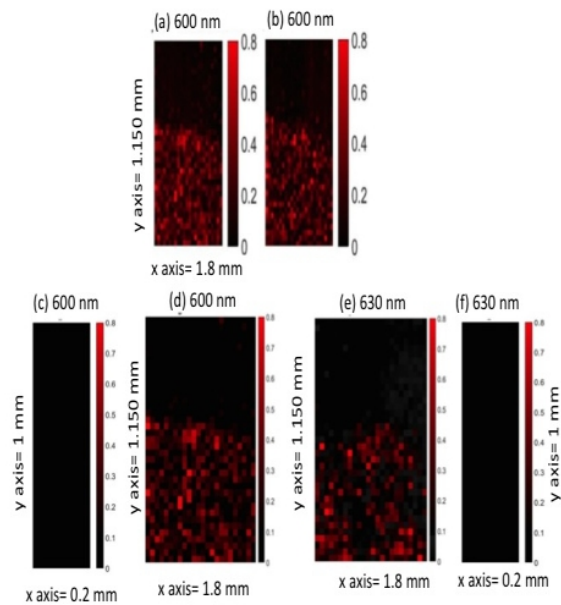
Figure 3.18. Photoacoustic image of the phantom containing skmel28 cell pellet inclusions at (a) 600 nm (b) 600 nm (the repeated scanning), (d) at 600 nm (the repeated scanning), (e) at 600 nm (c) the PA image of agarose based backgrounds at (c) 630 nm, (f) at 630 nm.

4. AN EXTENDED PHOTOACOUSTIC TRANSPORT MODEL FOR CHARACTERIZATION OF RED BLOOD CELL MORPHOLOGY IN MICROCHANNEL FLOW

The dynamic response behavior of red blood cells holds the key to understand red blood cell related diseases. In this regard, understanding of physiological functions of erythrocytes is significant before focusing on red blood cell aggregation in microcirculatory system. In this work, we present a theoretical model for a photoacoustic signal that occurs when deformed red blood cells pass through a microfluidic channel. Using a Green's function approach, the photoacoustic pressure wave is obtained analytically by solving a combined Navier-Stokes and photoacoustic equation system. The photoacoustic wave expression includes determinant parameters for the cell deformability such as plasma viscosity, density, and red blood cell aggregation as well as involves laser parameters such as beamwidth, pulse duration, and repetition rate. The effects of aggregation on blood rheology are also investigated. The results presented by this study show good agreements with the experimental ones in the literature. The comprehensive analytical solution of the extended photoacoustic transport model including a modified Morse type potential function sheds light on the dynamics of aggregate formation and demonstrates that the profile of a photoacoustic pressure wave has the potential for detecting and characterizing red blood cell aggregation.

4.1. Introduction

Red blood cells (RBCs) have the deformation capability in microcapillaries. RBC membrane allows cells to squeeze, deform, and reform through capillaries. The geometric shape of RBC provides an efficient transport through narrow capillaries and increases the surface area in order to maximize oxygen transport. The alternation of the cell membrane deformability under some disease conditions is significantly different than healthy ones [133,134]. To illustrate, the RBCs of sickle cell disease have the most significant loss of deformability because of having different morphologies depending on

its density [135–138]. The small changes in the morphology of RBCs are characterized by the absorption-based contrast of photoacoustic (PA) imaging which is complementary to other imaging modalities in terms of contrast mechanism, penetration, spatial resolution, and temporal resolution [24, 84, 139–148].

Recent studies seek to provide insights to measure RBC deformability via experimental techniques such as atomic force microscopy (AFM) [149–152], micropipette aspiration technique [153–156], optical and magnetic tweezers [30, 31, 157–160], microfluidic device techniques [134, 161–163]. Moreover, mathematical (analytical and numerical) models have been also presented in order to distinguish cell types and identify several diseases [31, 160, 164–166]. Using these experimental techniques and mathematical methods, intrinsic mechanical properties of RBCs (geometry and cytoplasmic viscosity), and viscoelastic properties of their membrane cortex structure are assessed. The shear modulus of RBC is inferred using optical tweezers while two microspheres attached to the opposite sides of RBC are trapped. Unless the laser beam is tightly focused on microbeads attached to the cells, the cell damages occur because of temperature rise [167]. The stiffness of cells is measured via AFM by isolating the AFM system from surrounding vibrations [168]. Micropipette aspiration is another technique for investigating cellular mechanical properties via aspirating pressure. Although this technique provides a broad range of applications, the unstable base pressure coming from vapor evaporation in the aspiration chamber may occur owing to the dependence of operator's skills [156]. Furthermore, magnetic tweezer has been applied to monitor mechanical properties of single molecules, intermolecular bonds, and whole cells. It gives information about complex modulus of elasticity and the local viscoelasticity of the cells. However, it is required to ensure highly localized magnetic fields, field gradients, and spherical magnetic beads with various sizes to obtain more accurate viscoelastic properties of the cells [169].

The hemoglobin within RBCs as an endogenous contrast agent absorbs visible and near-infrared light, which enables to image RBCs without staining via PA microscopy [139, 141, 170, 171]. Even though the image does not give information about their shapes and structures, PA signal with amplitude, width, rise, and relaxation time

enables to observe morphological changes in RBCs. The changes in the PA response depending on the cell elastic properties differentiate between healthy RBCs and diseased or damaged RBCs [22–24]. In the context of the detection of individual RBCs, there are several recent PA studies utilizing theoretical, experimental, and computational methods [172]. Saha *et al.* firstly described the PA pressure field generated by a collection of erythrocytes with the help of a theoretical model developed by Diebold *et al.* [172–175]. In vivo RBC age or surface charge density was presented using a two dimensional simulation study based on the PA signal properties of erythrocyte aggregation level which is related to the suspending medium [173, 175]. In another work, Saha and Kolios not only presented experimental results but also showed that the theoretical simulation study assessing PA signals could be followed to determine the degree of aggregation [176]. This frequency domain theoretical model was also used for a computer simulation study in order to differentiate intraerythrocytic stages of malarial parasite such as normal, ring, trophozoite, and schizont stages [172].

Mathematical models to calculate PA signal produced from one or more cells have been reported in a limited number of studies [174, 176–178]. Generally, cells were approximated as fluid spheres. The PA pressure wave produced by a collection of absorbing spheres was usually considered as a linear superposition of spherical waves emitted by individual sources [176]. It was assumed that acoustic waves coming from an absorbing sphere were not influenced by other particles in the medium, and all double and multiple scatterings of light beam were also ignored. The other study utilizing mathematical models was the description of PA signal in the time domain produced from one or more cells using an absorption model. The results of this study demonstrated that PA amplitude does not depend on the position of the cells in the stimulation field. In addition, the validity of the model was confirmed with experiments and simulations prior to experiments were carried out for the elimination of blind estimation [177]. Li *et al.* solved the PA Helmholtz equation by using the separation of variables method in spheroidal coordinates for a spheroidal droplet which is a more realistic geometric shape than a sphere [178]. When the PA detection of RBCs and their nuclei are considered, this derivation provides an opportunity to obtain a numerical simulation for practical uses of analyzing experimental data.

In this paper, we establish a PA wave expression for RBCs by using an extended Navier-Stokes equation when they travel into a microvessel. Our approach takes into consideration the interaction of cells to investigate RBC aggregation and its effect on blood rheology. We model the cells as spheres and the interaction forces between two cells cause the formation of aggregate clusters. We also analyze PA signal characteristics in the dynamic modes by means of RBC aggregation associated with complex hemorheological changes as well as viscosity. The motion of deformable cells can be described by the immersed boundary method based on Navier-Stokes equation. In order to evaluate the degree of aggregation which is related to their surface structure and their shape, the intercellular interaction is represented by the Morse type potential function [179]. Using a Green's function approach, an extended PA wave equation including a modified Morse type potential is solved analytically in detail. We obtain the PA pressure wave generated by normal and pathological RBCs associated with distinctive parameters such as a coefficient of surface energy and a scaling factor controlling the interaction decay behavior. The PA signal not only includes determinant parameters for the deformability of the cell such as plasma viscosity, density, and RBC aggregation but also contains laser parameters such as beamwidth, pulse duration, and repetition rate since the temporal profile is considered Gaussian rather than the Dirac delta function. Therefore, the approach given in this work can be useful to analyze the deformability of RBCs by taking advantage of the PA phenomena. The study of the mathematical modeling and the experimental design and detection of PA waves in micro-channels can be helpful for an appropriate choice of therapy.

4.2. Method: Combined Navier-Stokes and Heat Transfer Equations for An Compressible Flow

In this section, we present an expression for PA waves resulted from RBCs which travel into microvessels by solving the extended Navier-Stokes equation including RBC aggregation kinetics. The schematic of our model is shown in Fig. 4.1. The red blood cell is radiated with a pulsed laser. The PA waves resulted from the red blood cell are received by the detector. The interaction between the red blood cells is depicted by
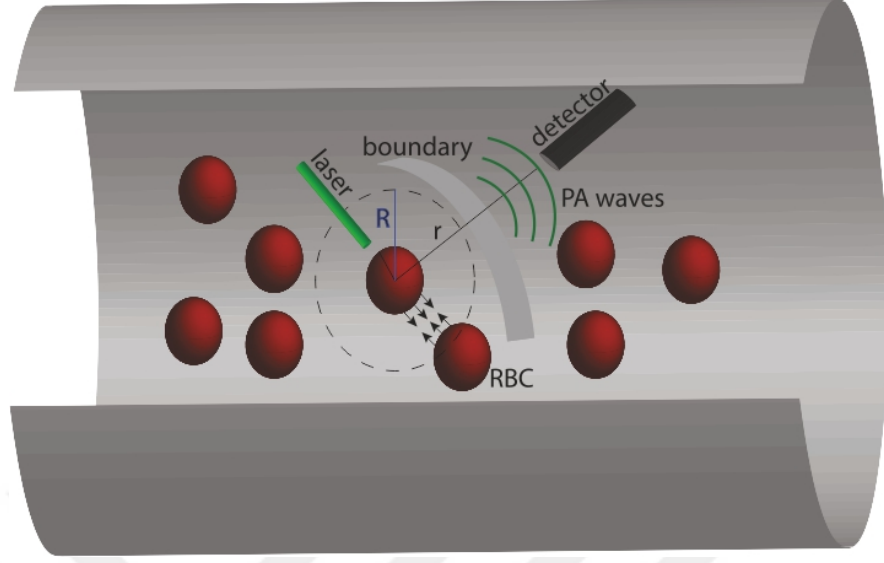
Figure 4.1. The schematic of the model.

the arrows.

Absorption of light leads to a thermal expansion

$$\rho_0 c_p \frac{\partial T(\mathbf{r}, t)}{\partial t} - \kappa \nabla^2 T(\mathbf{r}, t) = H(\mathbf{r}, t) \tag{4.1}$$

where ρ_0 is the mass density, c_p is the constant-pressure heat capacity per unit mass, κ is the thermal conductivity, $T(\mathbf{r}, t)$ is the temperature rise at position $\mathbf{r}$ and time t, and $H(\mathbf{r}, t)$ is the heating function defined as the optical energy deposited per unit time and per unit volume [14, 17].

As a result of the thermal expansion, acoustic waves are generated. In this process, the mass density obeys the continuity equation

$$\frac{\partial \rho}{\partial t} + \nabla \cdot (\rho \mathbf{v}) = \rho \beta \frac{\partial T(\mathbf{r}, t)}{\partial t} \tag{4.2}$$

where ρ, $\mathbf{v}$, and β are the mass density, the velocity field, and the coefficient of the volume thermal expansion, respectively [17, 180]. The velocity field $\mathbf{v}$ holds for the

Navier-Stokes equation

$$\rho[\frac{\partial \mathbf{v}}{\partial t} + \mathbf{v}(\nabla \cdot \mathbf{v})] = -\nabla p + \eta \nabla^2 \mathbf{v} + (\zeta + 1/3\eta)\nabla \cdot (\nabla \cdot \mathbf{v}) \tag{4.3}$$

where p is the pressure, η is the shear viscosity, and ζ is the bulk viscosity [181]. The thermal diffusion can be neglected since the pulse duration is very short so that the combination of Eq. (4.1) with Eq. (4.2) gives

$$\frac{\partial \rho}{\partial t} + \rho \nabla \cdot \mathbf{v} = \frac{\beta H(\mathbf{r}, t)}{c_p}. \tag{4.4}$$

Under the assumptions of small amplitude photoacoustic wave and sufficiently small source power, the pressure and density can be written as $p = p_0 + \delta p$ and $\rho = \rho_0 + \delta \rho$ where p_0 and ρ_0 are the equilibrium pressure and density with $\delta p \ll p_0$ and $\delta \rho \ll \rho_0$, respectively [181]. After the linearizations of the Eqs. (4.3) and (4.4) under the assumption of small amplitude photoacoustic wave with constant p_0 and ρ_0, we obtain

$$\frac{\partial \delta \rho}{\partial t} + \rho_0 \nabla \cdot \mathbf{v} = \frac{\beta H(\mathbf{r}, t)}{c_p} \tag{4.5}$$

and

$$\rho_0 \frac{\partial \mathbf{v}}{\partial t} = -\nabla \delta p + \eta \nabla^2 \mathbf{v} + (\zeta + \frac{1}{3}\eta)\nabla \cdot (\nabla \cdot \mathbf{v}). \tag{4.6}$$

In order to simulate the blood flow in a microfluidic device for the deformation of a single red blood cell in a microvessel, the relationship between the mass density and the velocity field in the fluid can be obtained by solving the extended Navier-Stokes

equation with a body force denoted by $\boldsymbol{f}(\mathbf{r}, t)$

$$\rho_0 \frac{\partial \mathbf{v}}{\partial t} = -\nabla \delta p + \eta \nabla^2 \mathbf{v} + \nu \nabla \cdot (\nabla \cdot \mathbf{v}) + \boldsymbol{f}(\mathbf{r}, t), \tag{4.7}$$

and

$$\boldsymbol{f}(\mathbf{r}, t) = \sum_{n=1}^{N} [\mathbf{F}^n \Delta(\mathbf{r} - Y^n(t))] \tag{4.8}$$

where $\nu = (\zeta + \frac{1}{3}\eta)$ is the blood viscosity. Here, $\mathbf{F}^n$ is the aggregation force between two cells, n is the index of RBCs and N is the total number of interacting RBCs. The interaction force between RBCs, F^n is modeled by the Morse potential, and Δ is an interpolation function (interpolation kernel) which enables to model the interaction between the immersed structure and the fluid. Here, Y^n is the position of the center of the red blood cell and $\mathbf{r}$ is the flow position. The cells aggregate slowly and an equilibrium configuration occurs when the intercellular interaction is balanced via the membrane forces after the deformation of the RBC membrane in microfluidic devices [182, 183].

Combining Eqs. (4.5) and (4.7), the PA wave resulted from a collection of erythrocytes (which is considered as an optical absorber) can be obtained by solving the following equation

$$\frac{1}{c_s^2} \frac{\partial^2 p(\mathbf{r}, t)}{\partial t^2} = \nabla^2 p(\mathbf{r}, t) + \frac{\eta'}{\rho_0 c_s^2} \left[\frac{\partial \nabla^2 p(\mathbf{r}, t)}{\partial t} - \Gamma \nabla^2 H(\mathbf{r}, t) \right] - \nabla \cdot \boldsymbol{f}(\mathbf{r}, t) + \frac{\beta}{c_p} \frac{\partial H(\mathbf{r}, t)}{\partial t} \tag{4.9}$$

where c_s is the speed of sound, $\Gamma = \frac{\beta c_s^2}{c_p}$, $\delta p = c_s^2 \delta \rho$, and $\eta' = (\zeta + \frac{4}{3}\eta)$. Thus, Eq. (4.9) can be written in the following form

$$\nabla^2 p(\mathbf{r}, t) + \frac{\eta'}{\rho_0 c_s^2} \frac{\partial \nabla^2 p(\mathbf{r}, t)}{\partial t} - \frac{1}{c_s^2} \frac{\partial^2 p(\mathbf{r}, t)}{\partial t^2} = S(\mathbf{r}, t) \tag{4.10}$$

where $S(\mathbf{r}, t)$ is the source term which can be described by

$$S(\mathbf{r}, t) = \frac{-\beta}{c_p} \frac{\partial H(\mathbf{r}, t)}{\partial t} + \frac{\Gamma \eta'}{\rho c_s^2} \nabla^2 H(\mathbf{r}, t) + \nabla \cdot \boldsymbol{f}(\mathbf{r}, t). \tag{4.11}$$

The first and second source terms on the right-hand side of Eq. (4.11) are due to the heat-producing, optical absorption within the two-phase sphere composed of one absorber (red blood cell) and fluid (blood plasma). Here, the fluid and the solid occupy a domain, but they do not intersect; thus, we model the fluid-structure interaction with the immersed boundary method and the boundary integral method. Moreover, the basic behaviour of the interaction forces between two RBCs is illustrated in Fig. 4.2. The third source term on the right-hand side of Eq. (4.11) is due to the interaction force between the two RBCs. Therefore, we can write the source term as $S(\mathbf{r}, t) = S_1(\mathbf{r}, t) + S_2(\mathbf{r}, t) + S_3(\mathbf{r}, t)$.

Using the Fourier convention, $\{p(\mathbf{r}, t), S(r, t)\} = \frac{1}{\sqrt{2\pi}} \int_{-\infty}^{\infty} \{\widetilde{p}(\mathbf{r}, \omega), \widetilde{S}(\mathbf{r}, \omega)\} \exp(-i\omega t) d\omega$, the wave equation can be expressed in the frequency domain

$$\nabla^2 \widetilde{p}(\mathbf{r}, \omega) + \frac{\omega^2 \widetilde{p}(\mathbf{r}, \omega)}{c_s^2 (1 - i\omega B)} = \widetilde{S}(\mathbf{r}, \omega). \tag{4.12}$$

where $B = \frac{\eta'}{\rho_0 c_s^2}$. The solution of Eq. (4.9) can be found by utilizing the Green's function approach [184]. The Green's function for Eq. (4.12) is given by

$$\widetilde{G}(\mathbf{r}, \mathbf{r}'; \omega) = -\frac{1}{4\pi \mid \mathbf{r} - \mathbf{r}' \mid} \exp(ik_1 \mid \mathbf{r} - \mathbf{r}' \mid) \tag{4.13}$$

where $k_1^2 = \frac{\omega^2}{c_s^2(1-i\omega)}$ [184]. The heating function can be decomposed into the spatial and temporal parts as follows

$$H(\mathbf{r}, t) = A(\mathbf{r})I(t). \tag{4.14}$$

The heating due to the pulsed laser beam is very localized in both time and space so that the temporal and spatial parts of the heating function can be expressed by Gaussian functions. The radial part of the heating function can be written as

$$A(\mathbf{r}) = \frac{p_0(\mathbf{r})c_p}{c_s^2 \beta}. \tag{4.15}$$

Here, $p_0(r)$ is the initial pressure rise just after the laser pulse and it is defined by

$$p_0(\mathbf{r}) = \frac{\beta T(r)}{c_\kappa} \tag{4.16}$$

where c_κ is the isothermal compressibility [185, 186]. This initial pressure rise can be decsribed by a Gaussian function as can be seen in the following section [186]. The temporal profile can be described by

$$I(t) = \frac{\exp(-t^2/2\tau^2)}{\sqrt{2\pi\tau^2}} \tag{4.17}$$

where τ is the pulse duration of the laser.

Substituting Eqs. (6.15) and (6.14) into Eq. (6.13) leads to

$$S_1(\mathbf{r}, t) = \frac{-p_0(\mathbf{r})}{c_s^2} \frac{\partial}{\partial t}\left[\frac{\exp(-t^2/2\tau^2)}{\sqrt{2\pi\tau^2}}\right] = \frac{1}{\sqrt{2\pi\tau^3}}\frac{p_0(\mathbf{r})}{c_s^2}t\exp(-t^2/2\tau^2). \tag{4.18}$$

After applying the Fourier transform to S_1 yields

$$\widetilde{S}_1(\mathbf{r}, \omega) = \frac{1}{2\pi\tau^3}\frac{p_0(\mathbf{r})}{c_s^2}\int_{-\infty}^{+\infty} t\exp(-t^2/2\tau^2)\exp(i\omega t)dt = \frac{p_0(\mathbf{r})i\omega}{c_s^2}\exp(-\tau^2\omega^2/2).$$

(4.19)

Moreover, the second source term in Eq. (4.11) can be written as follows

$$S_2(\mathbf{r}, t) = \frac{\eta'\Gamma}{\rho_0 c_s^2}\left[\frac{\exp(-t^2/2\tau^2)}{\sqrt{2\pi\tau^2}}\right]\nabla^2 p_0(r).$$

(4.20)

The Fourier transform of $S_2(\mathbf{r}, t)$ is

$$\widetilde{S}_2(\mathbf{r}, \omega) = \frac{\eta'\Gamma}{\rho c_s^2}\nabla^2\widetilde{p}_0(r)\int_{-\infty}^{+\infty}\frac{\exp(-t^2/2\tau^2)}{\sqrt{2\pi\tau^2}}\exp(i\omega t)dt = \frac{\eta'\Gamma}{\rho c_s^2}\nabla^2\widetilde{p}_0(\mathbf{r})\exp(-\tau^2\omega^2/2).$$

(4.21)

The function $\mathbf{f}(\mathbf{r}, t)$ in Eq. (4.9) can be expressed by

$$\boldsymbol{f}(\mathbf{r}, t) = \sum_{n=1}^{N}[\ \mathbf{F}^n\Delta(\mathbf{r} - \mathbf{Y}^n(t))]$$

(4.22)

where n is the index of the particle and N is the number of absorbing particles (RBCs) referring to the radius of clusters of RBC aggregates.

According to the immersed boundary method, we consider an compressible three-dimensional deformable structure in a RBC membrane immersed in an compressible fluid domain. In this regard, the combination of the fluid and structure is possible, provided that they do not intersect [2, 4, 183, 187]. Based on this method, the contri-

bution of each RBCs whose center of mass is located at $\mathbf{Y}^n$ to the flow at position r (which is considered as a distance between the source and the detector) is smoothed by a Gaussian distribution kernel. The choice of Gaussian kernel is a good assumption to study problems involving fluid-structure interactions in which an elastic structure is immersed in a viscous fluid. This method describes the fluid-membrane interaction between the flow field and deformable cells

$$\Delta(\mathbf{X}) = (2\pi h^2)^{-3/2} \exp\left[\frac{-(r-r')^2}{2h^2}\right] \frac{\exp(-t^2/2\tau^2)}{\sqrt{2\pi}} \tag{4.23}$$

where $X = (r - Y^n(t))$, and h is the standard deviation of the kernel, $h = \frac{R}{\sqrt{\pi}}$. Here, r' varies between 0 and R and chosen as Y^n.

The aggregating force between two cells represented by F^n in Eq. (4.22) is modeled by a Morse type potential function. The Morse type potential function was also employed to describe the interactions of RBCs [179,188]. The parameters of the Morse potential function for intercellular interaction are summarized in Table 4.1 [9–11,189,190] and Table 4.2 [1,2] (In Table 1, the physical properties are mapped onto the dimensionless properties for the consistency of the simulation with the experiment. The scaling procedure relates the model's non-dimensional units to the physical units [10].). Figure 4.2 shows the aggregation forces corresponding to the various aggregation strengths which are summarized in Tables 4.3 and 4.4. These red blood cell aggregation forces calculated from selected parameters show a good agreement with the experimental ones (Fig. 4.2) [3,12,191]. These experimental forces are in the range of 2-12 pN [12], 14-23 pN, and 43-169 pN [3,191]. The measurements of interaction forces between red blood cells in aggregates and the measurements on dextran-induced aggregation of red blood cells were obtained by optical tweezers and atomic force microscopy-based single cell force spectroscopy, respectively.

We use the following Morse function

$$f(r,t) = 2\beta D(e^{2\beta(r_0-d)} - e^{\beta(r_0-d)})(2\pi h^2)^{-3/2} \exp\left[\frac{-(r-r')^2}{2h^2}\right]\frac{\exp(-t^2/2\tau^2)}{\sqrt{2\pi}} \quad (4.24)$$

to detect the acoustic pressure of non-aggregated and aggregated erythrocytes, where β, D, r_0, and d are a scaling factor controlling the decay behavior of interaction of RBC, the coefficient of surface energy, the zero force separation, and the local distance between two surface elements of the cells, respectively. It is important to note that the number of absorbing particles (RBCs) depends on the radius of clusters of RBC aggregates (R). This number is expressed in terms of the radius of the defined region of interest since the amplitude of PA signal depends on radius of the absorber. In our case, $N = 1$. In our calculations, the interaction distance of the Morse potential regarding the immersed boundary method is calibrated with the distance between the source and detector in the case of the third source since our model couples the Navier-Stokes equation with the cell interaction and the bio-heat transfer equation. To see the contribution coming from the aggregation process on the photoacoustic wave, the interaction distance is the distance between detector and the absorber. For attractive forces, the value of the scaling force is negative when $r_0 < d$. Conversely, if the value of the force is positive when $r_0 > d$, the force is indicated by a repulsive force. The attractive force is crucial to represent an intercellular interaction through the Morse-type potential energy function. Under this intercellular interaction, the aggregation occurs either by increasing D or by decreasing β, which is shown in Figs. 4.2-4.4. Moreover, zero force length may raise the depletion thickness as well as equilibrium distance of the RBCs in aggregates. In Fig. 4.2, the strongest attractive force among three cases is observed in case 1. In order to examine the modified Morse function, aggregation forces which represent the different RBC aggregation as a function of separation between cell surfaces and the time scale of acoustic wave are illustrated in Figs. 4.3 and 4.4, respectively. The normalized amplitudes of modified aggregation forces (Figs. 4.3 and 4.4) exhibit a similar behavior, as shown in Fig. 4.2.
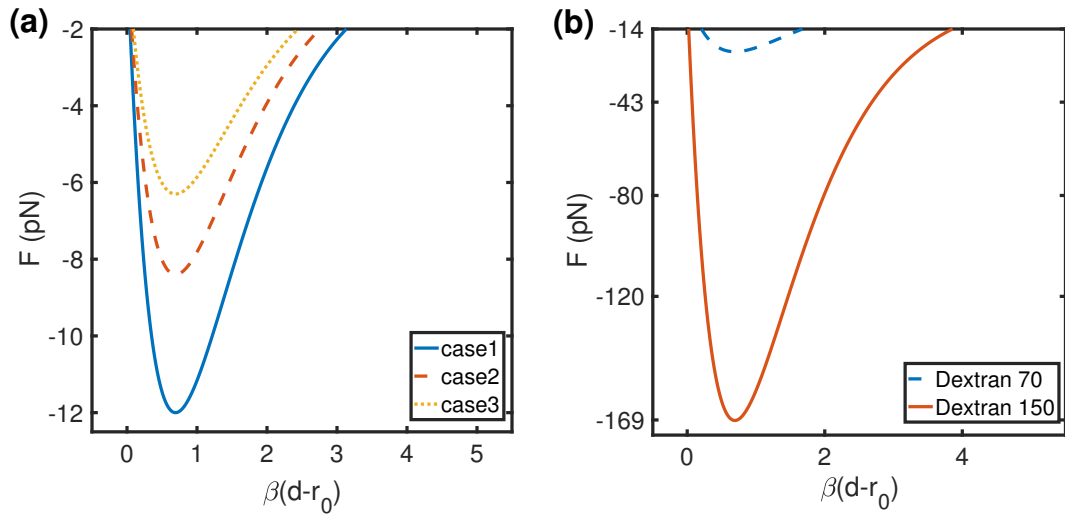
Figure 4.2. Aggregation force (F) corresponding to the various aggregation rates vs function of separation between cell surfaces (β(d-r_0)) for (a) case 1 [1,2]: $D = 3 \times 10^{-17}$ J/m^2, $\beta = 8 \times 10^5$ m^{-1}, $r_0 = 3$ μm; case 2 [1,2]: $D = 2.1 \times 10^{-17}$ J/m^2, $\beta = 8 \times 10^5$ m^{-1}, $r_0 = 2.5$ μm; case 3 [1,2]: $D = 2.1 \times 10^{-17}$ J/m^2, $\beta = 6 \times 10^5$ m^{-1}, $r_0 = 2$ μm, (b) Dextran 70 [3]: $D = 5.75 \times 10^{-17}$ J/m^2, $\beta = 6 \times 10^5$ m^{-1}, $r_0 = 2$ μm; Dextran 150 [3]: $D = 56.4 \times 10^{-17}$ J/m^2, $\beta = 8 \times 10^5$ m^{-1}, $r_0 = 3$ μm.
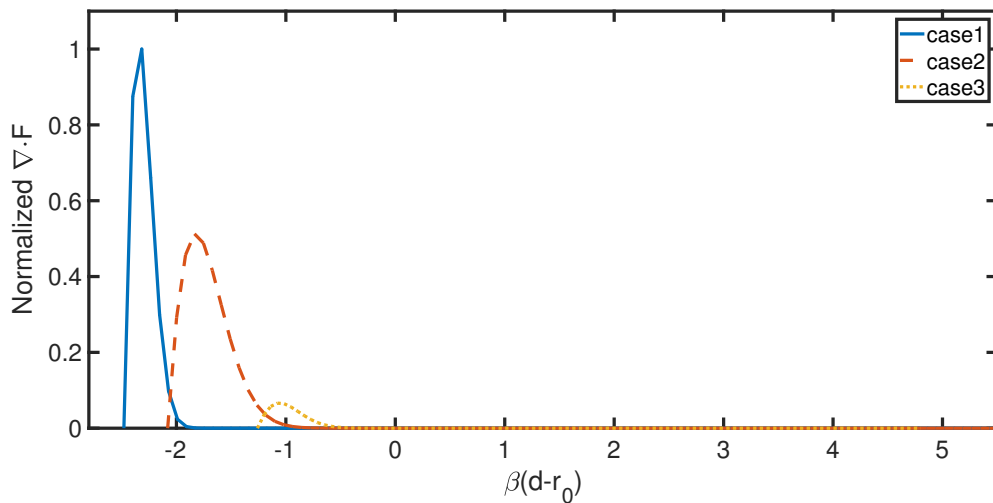
Figure 4.3. Normalized $\nabla \cdot$F (modified aggregation forces) vs function of separation between cell surfaces (β(d-r_0)) for case 1 [1,2]: $D = 3 \times 10^{-17}$ J/m^2, $\beta = 8 \times 10^5$ m^{-1}, $r_0 = 3$ μm; case 2 [1,2]: $D = 2.1 \times 10^{-17}$ J/m^2, $\beta = 8 \times 10^5$ m^{-1}, $r_0 = 2.5$ μm; case 3 [1,2]: $D = 2.1 \times 10^{-17}$ J/m^2, $\beta = 6 \times 10^5$ m^{-1}, $r_0 = 2$ μm.

Table 4.1. Model parameters [9–11].

Parameters	Simulations	Physical values
Intercellular interaction strength (D)	$1.976 - 88.92$	$5.2 \times 10^{-8} - 4.5 \times 10^{-6}$ J/m^2
Scaling factor (β)	$1.92 - 3.84$	3.84×10^{-6} m^{-1}
Zero force distance (r_0)	$0.49, 0.98$	0.49×10^{-6} m
Plasma viscosity (μ)	1.2×10^{-3}	$1.10 - 1.30$ cP

Table 4.2. Model parameters [1, 2].

Parameters	Simulations	Physical values
Energy depth (D) (J)	$2.1 \times 10^{-17}, 1 \times 10^{-25} - 1 \times 10^{-24}$	2.1×10^{-21}
Scaling factor (β) (m^{-1})	$8 \times 10^{5} - 1 \times 10^{7}$	3.84×10^{-6} (m^{-1})
Zero force distance (r_0) (m)	$3 \times 10^{-6}, 1 \times 10^{-11}$	0.49×10^{-6}
Plasma viscosity (μ) (cP)	1.2×10^{-3}	$1.10 - 1.30$

4.3. Solution of The Extended Photoacoustic Wave Equation for a Gaussian Radial Absorption Profile

In this section, we describe the radial profile by a Gaussian function with the standard deviation or beamwidth of the laser σ

$$p_0(\mathbf{r}) = p_0 \exp\left(-\frac{r^2}{2\sigma^2}\right)\theta(r)\theta(-r + R) \tag{4.25}$$

where θ is the Heaviside step function. Here, the initial pressure p_0 is created inside the object so that the initial pressure distribution can be defined as Eq. (6.28). The following integral can be written as a summation of three terms corresponding to three different sources as follows

$$\widetilde{p}(\mathbf{r}, \omega) = \int \widetilde{G}(\mathbf{r}, \mathbf{r}'; \omega)\widetilde{S}(\mathbf{r}', \omega)d^3r' \tag{4.26}$$

where S=S$_1$+S$_2$+S$_3$. The contribution coming from the first source is

Table 4.3. Constitutive parameters for the three various forces resulting from the RBC aggregation [1, 2, 12].

Parameters	Simulations		
	Case 1	Case 2	Case 3
Energy depth (D) ($\times 10^{-17}$) (J)	3	2.1	2.1
Scaling factor (β) ($\times 10^5$) (m^{-1})	8	8	6
Zero force distance (r_0) (μm)	3	2.5	2

Table 4.4. The model parameters for the measured dextran-induced aggregation forces of red blood cells [3].

Parameters	Simulations	
	Dextran 150	Dextran 70
Energy depth (D) ($\times 10^{-17}$) (J)	56.4	5.75
Scaling factor (β) ($\times 10^5$) (m^{-1})	8	6
Zero force distance (r_0) (μm)	3	2

$$\widetilde{p}_1(\mathbf{r}, \omega) = -\frac{ip_0}{4\pi}\frac{\omega}{c_s^2}\exp(\frac{-\tau^2\omega^2}{2})\int_0^{2\pi} d\phi \int_0^R (r')^2 dr' \int_{-1}^{+1} \frac{\exp[ik_1 \mid \mathbf{r} - \mathbf{r}' \mid]}{\mid \mathbf{r} - \mathbf{r}' \mid} d\mu' \quad (4.27)$$

where $\mid \mathbf{r} - \mathbf{r}' \mid = \sqrt{r^2 + r'^2 - 2rr'\mu'}$, $\mu' = \cos\theta'$, and

$$\int_{-1}^{+1} \frac{\exp[(ik_1)\sqrt{(r^2 + r'^2 - 2rr'\mu')}]}{\sqrt{(r^2 + r'^2 - 2rr'\mu')}} d\mu' = -\frac{1}{irr'k_1}[\exp[ik_1(r - r')] - \exp[ik_1(r + r')]].$$

So the solution due to the first source becomes
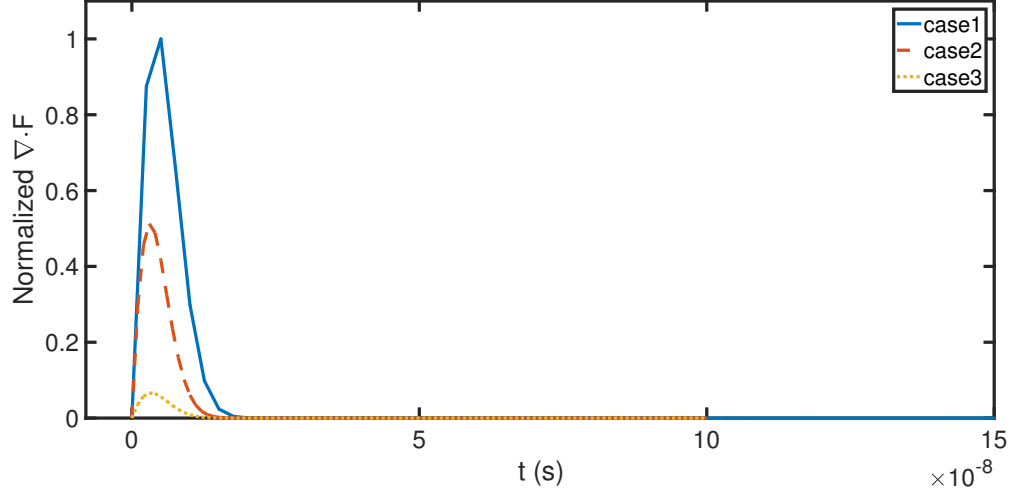
Figure 4.4. Normalized $\nabla \cdot \mathbf{F}$ which represents the different red blood cell aggregation conditions with different intercellular strengths vs time scale of acoustic wave, t(s) for case 1 [1, 2]: $D = 3 \times 10^{-17}$ J/m^2, $\beta = 8 \times 10^5$ m^{-1}, $r_0 = 3$ μm; case 2 [1, 2]: $D = 2.1 \times 10^{-17}$ J/m^2, $\beta = 8 \times 10^5$ m^{-1}, $r_0 = 2.5$ μm; case 3 [1, 2]: $D = 2.1 \times 10^{-17}$ J/m^2, $\beta = 6 \times 10^5$ m^{-1}, $r_0 = 2$ μm.

$$p_1(r, t) = \frac{p_0}{2\sqrt{2\pi} \ r c_s^2} \int_0^R dr' r' \exp\left(-\frac{r'^2}{2\sigma^2}\right)$$
$$\times \int_{-\infty}^{\infty} \exp\left[-\frac{\tau^2 \omega^2}{2} + ik_1(r \pm r') - i\omega t\right]\left[\frac{c_s \sqrt{1 - i\omega B}}{\omega}\right] \omega d\omega, \qquad (4.28)$$

Using the Taylor-series expansion

$$\sqrt{1 - i\omega B} = 1 - \frac{iB\omega}{2} + \frac{1}{8}(B\omega)^2 + O\left((B\omega)^3\right), \qquad (4.29)$$

we evaluate the integral in Eq. (6.32) [184, 192]

$$I = \int_{-\infty}^{\infty} \exp\left[-\frac{\tau^2 \omega^2}{2} + \left(\frac{i\omega(r \pm r')}{c_s \sqrt{1 - i\omega B}}\right) - i\omega t\right] d\omega$$
$$- \frac{iB}{2} \int_{-\infty}^{\infty} \omega \exp\left[-\frac{\tau^2 \omega^2}{2} + \left(\frac{i\omega(r \pm r')}{c_s \sqrt{1 - i\omega B}}\right) - i\omega t\right] d\omega. \qquad (4.30)$$

The exponential term can be further expanded [184, 192, 193]

$$\exp\left[\frac{i\omega(r\pm r')}{c_s\sqrt{1-i\omega B}}\right] \sim \exp\left[\frac{i\omega\left(r\pm r'\right)}{c_s}\right] - \frac{B\omega\left[\omega\left(r\pm r'\right)e^{\frac{i\omega(r\pm r')}{c_s}}\right]}{2c_s}. \tag{4.31}$$

Thus, we obtain [192, 193]

$$
\begin{aligned}
p_1(r,t) = &\frac{p_0}{2\sqrt{2\pi}}\frac{1}{rc_s}\int_0^R dr'r'\exp(-\frac{r'^2}{2\sigma^2})\\
&\times\left\{\int_{-\infty}^{\infty}\exp\left[-\frac{\tau^2\omega^2}{2}+\left(\frac{i\omega(r\pm r')}{c_s}\right)-i\omega t\right]d\omega\right.\\
&\left.-\frac{iB}{2}\int_{-\infty}^{\infty}\omega\exp\left[-\frac{\tau^2\omega^2}{2}+\left(\frac{i\omega(r\pm r')}{c_s}\right)-i\omega t\right]d\omega\right\}.
\end{aligned}\tag{4.32}
$$

Here, it is important to note that after a series of numerical calculation, we see that the contribution coming from the high order terms is negligible. This case can also be analyzed analytically. For large values of ω, the compactly supported function $\exp(-\tau^2\omega^2/2)$ dominates the higher order terms resulted from the series expansion. On the other hand, the physical parameters pulse duration (τ) and $B = \eta'/(\rho_0 c_s^2)$ are also on the orders of 10^{-9} and 10^{-12}, respectively so that the value of the integral is already very small for small values of ω. Therefore, based on the relatively small values of τ and B and the predominance of $\exp(-\tau^2\omega^2/2)$ term for large values of ω, the influence of the integral due to the higher order terms is negligible.

So that the $p_1(r,t)$ can be simplified as follows

$$p_1(r,t) = \left[\frac{p_0}{2\sqrt{2\pi}}\frac{1}{rc_s}\right]\left[J_{1a} + \frac{iB}{2}J_{1b}\right] \tag{4.33}$$

where

$$J_{1a} = \int_0^R dr' r' \exp(-\frac{r'^2}{2\sigma^2}) \left[\frac{\sqrt{2\pi} \exp(-\frac{(c_s t + r' - r)^2}{2\tau^2 c_s^2})}{\tau} - \frac{\sqrt{2\pi} \exp(-\frac{(-c_s t + r' + r)^2}{2\tau^2 c_s^2})}{\tau} \right] \quad (4.34)$$

and

$$J_{1b} = \int_0^R dr' r' \exp(-\frac{r'^2}{2\sigma^2}) \left[\frac{i\sqrt{2\pi} (-c_s t + r' + r) \exp(-\frac{(-c_s t + r' + r)^2}{2\tau^2 c_s^2})}{\tau^3 c_s} \right.$$
$$\left. + \frac{i\sqrt{2\pi} (c_s t + r' - r) \exp(-\frac{(c_s t + r' - r)^2}{2\tau^2 c_s^2})}{\tau^3 c_s} \right]. \quad (4.35)$$

Substituting the results of the integrals J_{1a} and J_{1b} into Eq. (6.33) enables to find the pressure due to $S_1(r, t)$

$$J_{1a} = \frac{\tau \sigma^2 c_s}{2(\sigma^2 + \tau^2 c_s^2)^{3/2}} \exp\left[-\frac{2R(r - c_s t) + 2(r - c_s t)^2 + R^2}{2\tau^2 c_s^2} - \frac{R^2}{2\sigma^2} \right]$$
$$\left(\sqrt{2\pi}\sigma(r - c_s t) \left\{ \text{erf}\left[\frac{\sigma^2(-r + R + c_s t) + R\tau^2 c_s^2}{\sqrt{2}\tau\sigma c_s \sqrt{\sigma^2 + \tau^2 c_s^2}} \right] \right.\right.$$
$$\times \exp\left[\frac{(r + R - c_s t)^2}{2\tau^2 cs^2} + \frac{\sigma^2(r - cst)^2}{2\tau^2 cs^2(\sigma^2 + \tau^2 c_s^2)} + \frac{R^2}{2\sigma^2} \right]$$
$$+ \text{erf}\left[\frac{\sigma^2(r + R - c_s t) + R\tau^2 c_s^2}{\sqrt{2}\tau\sigma c_s \sqrt{\sigma^2 + \tau^2 c_s^2}} \right] \exp\left[\frac{\frac{(\sigma^2(r + R - c_s t) + R\tau^2 c_s^2)^2}{\sigma^2(\sigma^2 + \tau^2 c_s^2)} + (r - c_s t)^2}{2\tau^2 c_s^2} \right] \right]$$
$$- 2\tau c_s \sqrt{\sigma^2 + \tau^2 c_s^2} \exp\left[\frac{(r - c_s t)^2}{2\tau^2 c_s^2} \right] \exp\left[\frac{2R(r - c_s t)}{\tau^2 c_s^2} \right] - 1 \right\} \right)$$
$$\times \theta(r - |R - c_s t|)\theta(-r + R + c_s t) \quad (4.36)$$

where $\text{erf}(x)$ is the error function. It is important to note that the value of the integral J_{1b} is sufficiently small compared to the integral J_{1a}.

The solution of the PA equation due to the second source in time domain can be evaluated by using the Taylor series expansion in the following $p_2(r, t)$ expression

similar to the calculation of $p_1(r, t)$

$$p_2(r, t) = \frac{\eta' \Gamma}{i\rho c_s^2} \int_0^R r' dr' \ \nabla^2 p_0(r')$$

$$\times \int_{-\infty}^{\infty} \exp\left[-\frac{\tau^2 \omega^2}{2} + ik_1(r \pm r') - i\omega t\right] \left[\frac{c_s \sqrt{1 - i\omega B}}{\omega}\right] d\omega. \tag{4.37}$$

Hence, p_2 simplifies to

$$p_2(r, t) = \frac{\eta' \Gamma}{i\rho c_s} \int_0^R r' dr' \ \nabla^2 p_0(r')$$

$$\times \left\{ \int_{-\infty}^{\infty} \frac{\exp\left[-\frac{\tau^2 \omega^2}{2} + \frac{i\omega(r \pm r')}{c_s} - i\omega t\right]}{\omega} d\omega - \right.$$

$$\left. \frac{iB}{2} \int_{-\infty}^{\infty} \exp\left[-\frac{\tau^2 \omega^2}{2} + \frac{i\omega(r \pm r')}{c_s} - i\omega t\right] d\omega \right\}. \tag{4.38}$$

The first integral with respect to ω in Eq. (4.38) can be calculated by using the residue theorem. Applying the residue theorem at z=0

$$J = \oint \frac{\exp\left[-\frac{\tau^2 z^2}{2} + \frac{iz(r \pm R)}{cs} - izt\right]}{z} dz, \tag{4.39}$$

$$J = \begin{cases} \pi i \lim_{z \to 0} z \frac{\exp\left[-\frac{\tau^2 z^2}{2} + iz\left(\frac{(r \pm R)}{c_s} - t\right)\right]}{z} & if \left(\frac{r \pm R}{c_s} - t\right) > 0 \\ -\pi i \lim_{z \to 0} z \frac{\exp\left[-\frac{\tau^2 z^2}{2} + iz\left(\frac{r \pm R}{c_s} - t\right)\right]}{z} & if \left(\frac{r \pm R}{c_s} - t\right) < 0. \end{cases}$$

$$\tag{4.40}$$

The contribution coming from integral J is zero so that $p_2(r,t)$ becomes

$$p_2(r,t) = \frac{B\eta'\Gamma p_0}{4\sqrt{2\pi}\rho r c_s} \int_0^R dr'r' \left[\frac{r'^2 \exp(-\frac{r'^2}{2\sigma^2})}{\sigma^4} - \frac{\exp(-\frac{r'^2}{2\sigma^2})}{\sigma^2} \right]$$
$$\times \left[\frac{\sqrt{2\pi} \exp[-\frac{(-c_s t+r'+r)^2}{2\tau^2 c_s^2}]}{\tau} - \frac{\sqrt{2\pi} \exp[-\frac{(c_s t+r'-r)^2}{2\tau^2 c_s^2}]}{\tau} \right]. \tag{4.41}$$

We can express $p_2(r,t)$ in the following form

$$p_2(r,t) = \left[\frac{B\eta'\Gamma p_0}{4\sqrt{2\pi}\rho r c_s} \right] \left(J_{2a} - J_{2b} \right) \tag{4.42}$$

where

$$J_{2a} = \int_0^R dr'r' \left[\frac{(r')^2 \exp(-\frac{r'^2}{2\sigma^2})}{\sigma^4} - \frac{\exp(-\frac{r'^2}{2\sigma^2})}{\sigma^2} \right]$$
$$\times \left[\frac{\sqrt{2\pi} \exp\left[-\frac{(-c_s t+r'+r)^2}{2\tau^2 c_s^2}\right]}{\tau} \right] \tag{4.43}$$

and

$$J_{2b} = \int_0^R dr'r' \left[\frac{(r')^2 \exp(-\frac{r'^2}{2\sigma^2})}{\sigma^4} - \frac{\exp(-\frac{r'^2}{2\sigma^2})}{\sigma^2} \right]$$
$$\times \left[\frac{\sqrt{2\pi} \exp[-\frac{(c_s t+r'-r)^2}{2\tau^2 c_s^2}]}{\tau} \right]. \tag{4.44}$$

Moreover, the third PA wave, $p_3(r,t)$ due to the third source corresponding to aggregation force is

$$p_3(r,t) = \frac{c_s\tau}{4i\sqrt{2\pi}r} \int_0^R r'dr' \; \nabla \cdot f(r',\omega)$$
$$\times \left\{ \int_{-\infty}^{\infty} \frac{\exp[-\frac{\tau^2\omega^2}{2} + \frac{i\omega(r\pm r')}{c_s} - i\omega t]}{\omega} d\omega \right.$$
$$\left. - \frac{iB}{2} \int_{-\infty}^{\infty} \exp\left[-\frac{\tau^2\omega^2}{2} + \frac{i\omega(r \pm r')}{c_s} - i\omega t \right] d\omega \right\}. \tag{4.45}$$

The first integral over ω in Eq. (4.45) has the same form as shown in Eq. (4.38), and it can be evaluated by the contour integration method. We can rewrite Eq. (4.45) in the following form which yields the pressure wave of non-aggregated and aggregated erythrocytes

$$p_3(r,t) = \frac{c_s \tau B}{4\sqrt{2\pi r}} \left(J_{3a} - J_{3b} \right) \tag{4.46}$$

where

$$J_{3a} = -\frac{\beta D [e^{2\beta(r_0-d)} - e^{\beta(r_0-d)}]}{\pi h^5} \int_0^R dr' r'(r-r') \exp\left[-\frac{(r-r')^2}{2h^2} \right]$$
$$\times \left[\frac{\sqrt{2\pi} \exp\left[-\frac{(-c_s t + r' + r)^2}{2\tau^2 c_s^2} \right]}{\tau} \right] \tag{4.47}$$

$$J_{3b} = -\frac{\beta D [e^{2\beta(r_0-d)} - e^{\beta(r_0-d)}]}{\pi h^5} \int_0^R dr' r'(r-r') \exp\left[-\frac{(r-r')^2}{2h^2} \right]$$
$$\times \left[\frac{\sqrt{2\pi} \exp\left[-\frac{(c_s t + r' - r)^2}{2\tau^2 c_s^2} \right]}{\tau} \right]. \tag{4.48}$$

By evaluating the integral in Eq. (4.47), we obtain

$$
\begin{aligned}
J_{3a} =& \frac{\beta D \left(e^{\beta(r_0-d)} - 1\right)}{\pi\tau h^5} \\
& \times \left\{ \frac{\tau h^2 c_s}{2\left(\tau^2 c_s^2 + h^2\right)^{5/2}} \exp\left[-\frac{r(r - tc_s)}{\tau^2 c_s^2 + h^2} - \frac{\frac{r^2}{c_s^2} + t^2}{2\tau^2} + \beta(r_0 - d) - \frac{r^2}{2h^2} \right] \right. \\
& \times \left[2\tau h^2 c_s \sqrt{\tau^2 c_s^2 + h^2}(tc_s - 2r) \exp\left[\frac{\tau^2 r^2 c_s + h^2 rt}{\tau^4 c_s^3 + \tau^2 h^2 c_s} \right] \right. \\
& + \exp\left(\frac{\tau^4 r^2 c_s^4 + 2\tau^2 h^2 rtc_s^3 + h^4 r^2 + h^4 t^2 c_s^2}{2\tau^4 h^2 c_s^4 + 2\tau^2 h^4 c_s^2} \right) \sqrt{2\pi} h \\
& \times \left(h^2 \left(c_s^2 \left(\tau^2 + t^2\right) + 2r^2 - 3rtc_s \right) + \tau^2 c_s^2 \left(\tau^2 c_s^2 - 2r^2 + rtc_s\right) \right) \\
& \left. \left. \times \operatorname{erf}\left[\frac{\tau^2 rc_s^2 - h^2(r - tc_s)}{\sqrt{2}\tau hc_s \sqrt{\tau^2 c_s^2 + h^2}} \right] \right] \right] \\
& - \frac{\tau h^2 c_s}{2\left(\tau^2 c_s^2 + h^2\right)^{5/2}} \exp\left[-\frac{r(r - tc_s)}{\tau^2 c_s^2 + h^2} - \frac{r^2 + R^2 + t^2 c_s^2}{2b^2 c_s^2} + \beta(r_0 - d) - \frac{r^2 + R^2}{2h^2} \right] \\
& \times \left(2\tau c_s \sqrt{\tau^2 c_s^2 + h^2} \left(\tau^2 Rc_s^2 + h^2(-2r + R + tc_s)\right) \right. \\
& \times \exp\left(\frac{r(r - tc_s)}{\tau^2 c_s^2 + h^2} + \frac{tc_s(r + R) - rR}{\tau^2 c_s^2} + \frac{rR}{h^2} \right) \\
& + \exp\left[\frac{\tau^4 c_s^4 \left(r^2 + R^2\right) + 2\tau^2 h^2 c_s^2 \left(rtc_s + R^2\right) + h^4 \left(r^2 + R^2 + t^2 c_s^2\right)}{2\tau^2 h^2 c_s^2 \left(\tau^2 c_s^2 + h^2\right)} \right] \\
& \times \sqrt{2\pi} h \left(h^2 \left(c_s^2 \left(\tau^2 + t^2\right) + 2r^2 - 3rtc_s \right) + \tau^2 c_s^2 \left(\tau^2 c_s^2 - 2r^2 + rtc_s\right) \right) \\
& \left. \left. \times \operatorname{erf}\left[\frac{\tau^2 c_s^2(r - R) - h^2(r + R - tc_s)}{\sqrt{2}\tau hc_s \sqrt{\tau^2 c_s^2 + h^2}} \right] \right) \theta(r - |R - c_s t|)\theta(-r + R + c_s t) \right\}.
\end{aligned}
$$

$$(4.49)$$

Here, the Heaviside step function, θ, is introduced to take into consideration the propagation time when observation point is outside the PA absorber [185, 186]. The integrals J_{3a} and J_{3b} contribute significantly to the PA signal. We note that the calculation of the integral J_{3a} is very similar to the one of the integral J_{3b}.

4.4. Numerical/Simulation Parameters

The behavior of a normalized PA wave produced by a RBC as a function of normalized time is illustrated in Fig. 4.5 for two different pulse durations (τ=1 and 5 ns) and beamwidths ($\sigma = 6$ and 8 μm). The PA wave stemming from the first source is calculated from Eq. (6.33). In Fig. 4.5, the effects of the laser beamwidth and pulse duration on the PA signal are observed. The density, and the speed of sound within the cell, the radius of absorber are taken as $\rho = 1000$ kg/m^3, c_s=1520 m/s, R=8 μm [194], respectively. Fig. 4.6 shows the power spectrum of the PA signal given in Fig. 4.5. Eventhough the change in the PA amplitude is small in the time domain, it becomes more visible in the frequency domain. Fig. 4.7 illustrates the effects of the laser beamwidth and pulse duration on the PA signal for the detector position (2 mm away from the center of the absorber [195, 196]) regarding the feasibility of experimental realization in the presence of the first source. Fig. 4.8 and Fig. 4.9 show the effects of the plasma viscosity on the normalized PA wave, an ultrasonic detector located at r =2R and 500 μm, respectively [195, 197]. In Figs. 4.8-4.15, the shear and bulk viscosities are taken as $\eta = 1.2$, 1.3 mPa.s, $\zeta = 4.5$, 5, 6, 18.4, and 22.9 mPa.s, respectively [3, 7, 8, 198] as can be seen in the following section.

4.5. Results

The integrals J_{1a}, J_{1b}, J_{2a}, and J_{2b} given by Eqs. (6.35), (4.35), (4.43), and (4.44) are evaluated numerically and the pressure wave is found as a summation of p_1 and p_2 corresponding to the first and second sources, respectively. However, the contribution coming from the second source is negligible compared to the first one. The pressure waves from the first and second sources can be applied for the suspension of RBCs in an compressible fluid. Our results show that the magnitude of PA signal does not change with different plasma viscosity values as shown in Fig. 4.8, as expected, in the presence of first and second source terms. Moreover, Fig. 4.9 shows that the amplitude of PA wave is decreasing with the distance from absorber, r=500 μm when fiber optic sensing systems are considered [195].
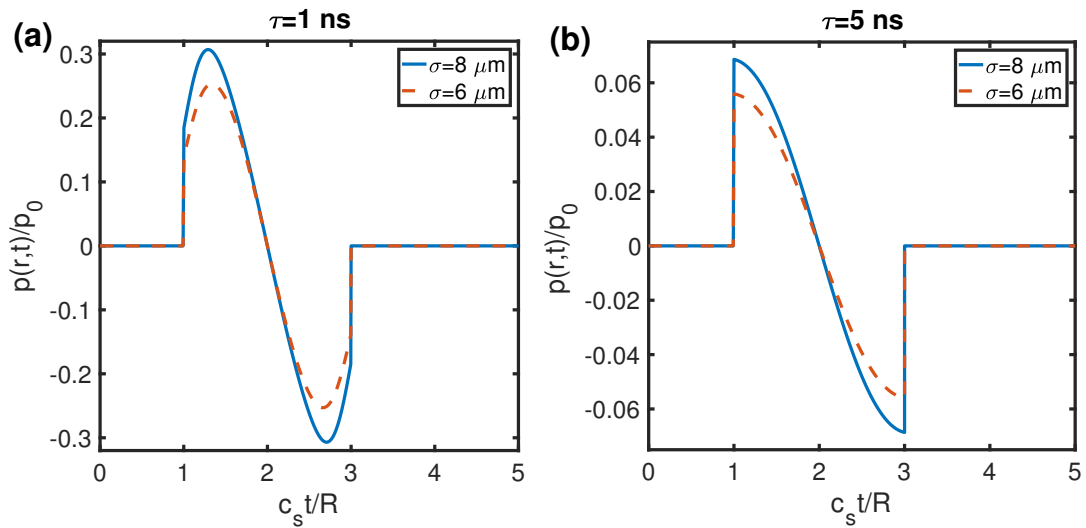
Figure 4.5. Normalized PA wave p(r,t)/p$_0$ generated by first source vs normalized time c$_s$t/R, an ultrasonic detector located at position r = 2R for the two different pulse durations (a) τ = 1 and (b) 5 ns with different beamwidths σ = 6 μm (dashed line) and 8 μm (solid line), where R = 8 μm.
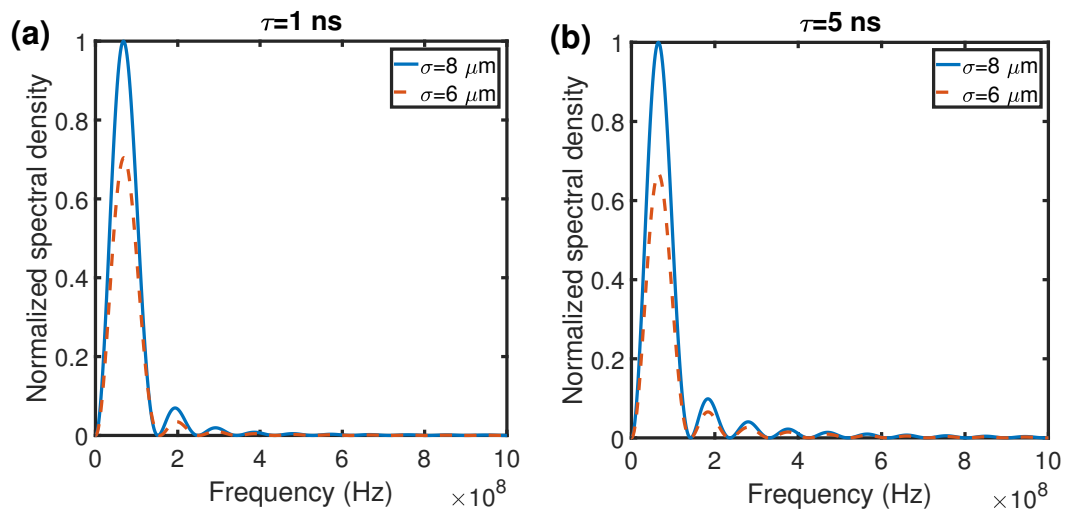
Figure 4.6. Normalized power spectral density of the photoacoustic wave in Fig. 4.5, an ultrasonic detector located at the position r = 2R for the two different pulse durations (a) τ = 1 and (b) 5 ns with the different beamwidths σ = 6 μm (dashed line) and 8 μm (solid line), where R = 8 μm.
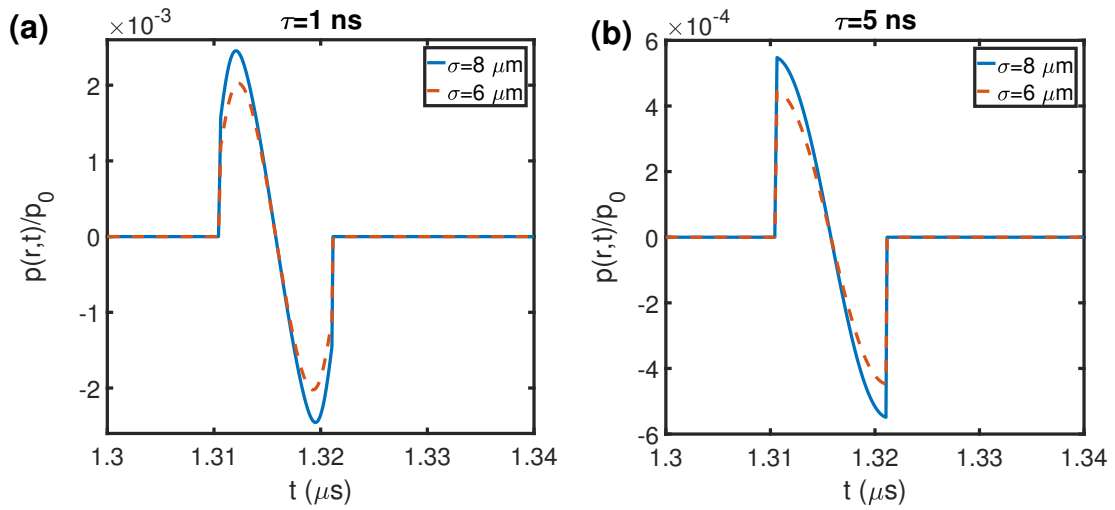
Figure 4.7. Normalized PA wave p(r,t)/p₀ vs time (μs), an ultrasonic detector located at position r = 2 mm. (a) τ = 1 with different beamwidths σ = 8 μm (dashed line) and 6 μm (solid line), where R = 8 μm and (b) 5 ns with different beamwidths σ = 8 μm (dashed line) and 6 μm (solid line), respectively
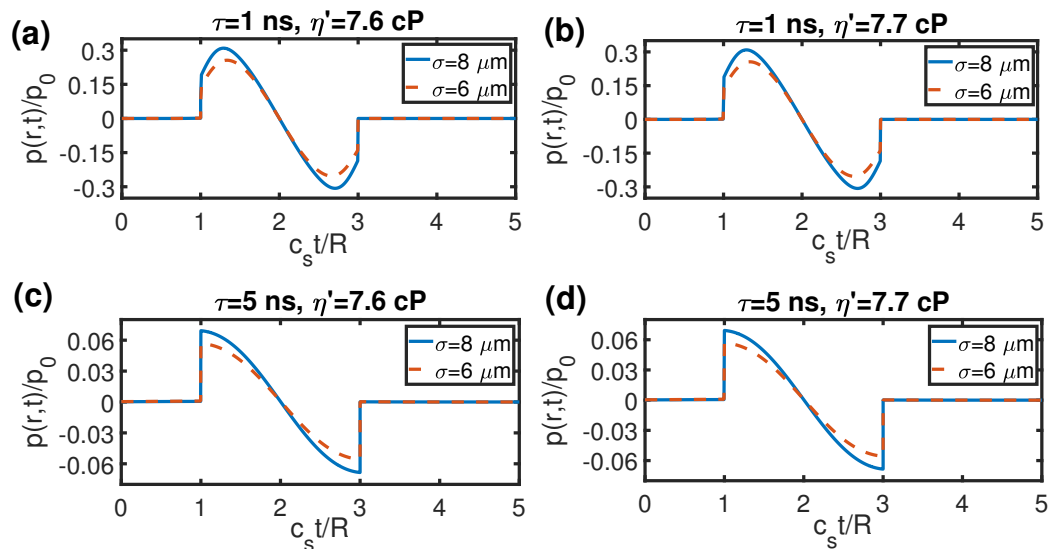
Figure 4.8. The effects of viscosity on normalized PA wave p(r,t)/p₀ vs normalized time c_st/R, an ultrasonic detector located at r = 2R (a)-(b) τ = 1,(c)-(d) 5 ns with different beamwidths σ = 6 (dashed line) and 8 μm (solid line), where R = 8 μm ((a)-(c) η=1.2 cP, ζ=6 cP, η'=7.6 cP and, (b)-(d) η=1.3 cP, ζ=6 cP, η'=7.7 cP) [4,5].
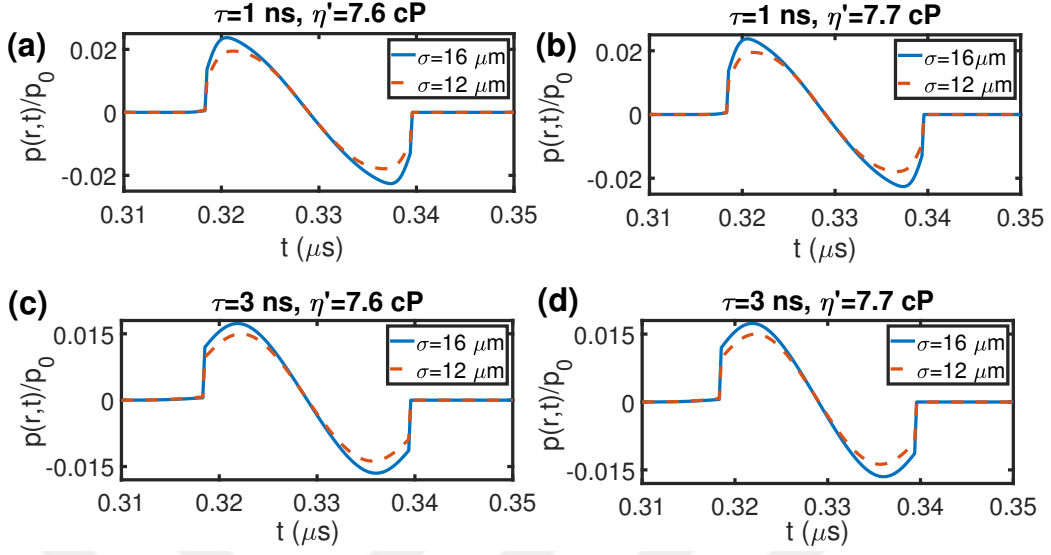
Figure 4.9. The effects of viscosity on normalized PA wave p(r,t)/p$_0$ vs time (μs), an ultrasonic detector located at r = 500 μm (a)-(b) τ = 1 and (c)-(d) 3 ns with different beamwidths σ = 16 (dashed line) and 14 μm (solid line), where R = 16 μm ((a)-(c) η=1.2 cP, ζ=6 cP, η'=7.6 cP and, (b)-(d) η=1.3 cP, ζ=6 cP, η'=7.7 cP) [4,5].

The aggregation interaction is described by the Morse potential consisting of a short-range repulsive force when $d < r_0$ and a long-range attractive force for $d > r_0$ [188,199]

$$E = D(e^{2\beta(r_0-d)} - 2e^{\beta(r_0-d)}). \tag{4.50}$$

The corresponding force, $F = -\partial E/\partial r$, is obtained from the Morse potential. In our calculations, the energy depth D is used in units of Joule and given in Tables 2 [1,2].

In this paper, the force is approximated with the several parameters involved in the detection of the PA signal, and the immersed boundary method is used to eliminate the effect of the fluid-cell interaction.

Different aggregating conditions are created by changing the surface energy (D), the scaling factor which is related to the thickness of the depletion layer or interactive distance (β), and zero-force length (r_0) which are shown in Tables 4.3 and 4.4. In these conditions, the aggregation strength is directly related to amount of surface energy,
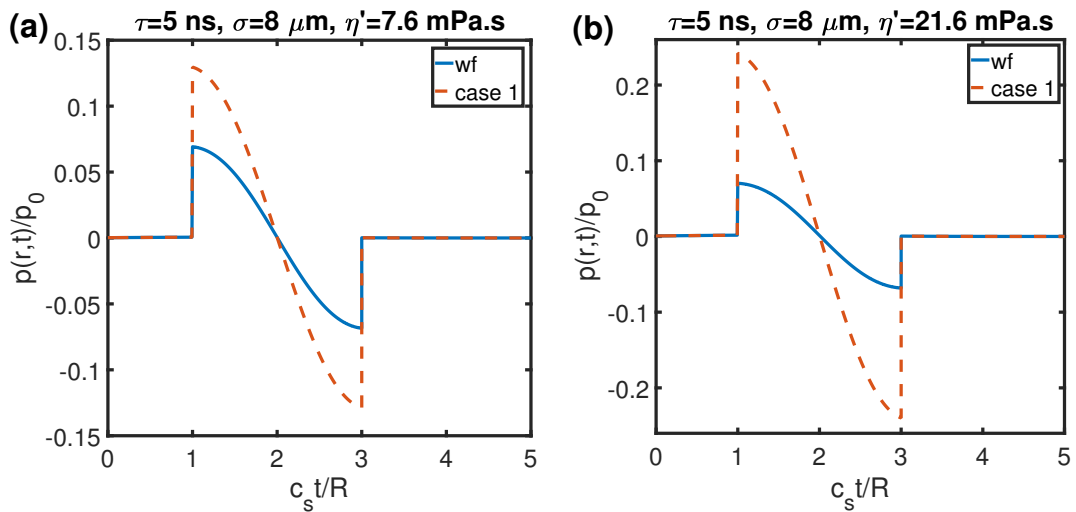
Figure 4.10. The effects of viscosity on normalized PA wave p(r,t)/p$_0$ generated by three sources for high level of aggregation force (case 1) (dashed line) and non-aggregation force (i.e., without force (wf)) (solid line) vs normalized time c_st/R, (a)-(b) τ = 5 ns with σ = 8 μm for both cases, where R = 8 μm [4–6].

which is expressed by the interaction force between RBCs. The parameters of the Morse potential in Table 4.3 used in this study were taken from the works presented by Yazdani *et al.* [2] and Fenech *et al.* [1], and the ranges of forces shown in Fig. 4.2(a) were fitted with the experimental data [12]. Moreover, the ranges of forces in Table IV were taken from studies presented by Neu *et al.* [191] and Steffen *et al.* [3], as shown in Fig. 4.2(b). In Fig. 4.10, the PA pressure wave generated by three sources increases with RBC aggregation (case 1 represents the high aggregation among three cases in Table 4.3, which is shown in Fig. 4.2). Moreover, our results demonstrate that high whole-blood viscosity has a role to play in erythrocyte aggregation since the amplitude of PA signal increases when the whole-blood viscosity is higher, as shown in Fig. 4.10 for case 1. When we compare the three cases, cases 2 and 3 show a lower aggregation. The influences of laser parameters and the levels of RBC aggregation on PA wave are shown in Figs. 4.11 and 4.12. These Figs. also show that the short pulse duration results in large wave amplitude, and the amplitude decreases as beamwidth diminishes for these cases. The aggregation for cases 2 and 3 is low and the force in the case 2 is close to the one in case 3. We examine the cases of Dextran 70 and Dextran 150 in Figs. 4.13 and 4.14. In Fig. 4.15, we also analyze the cases 1
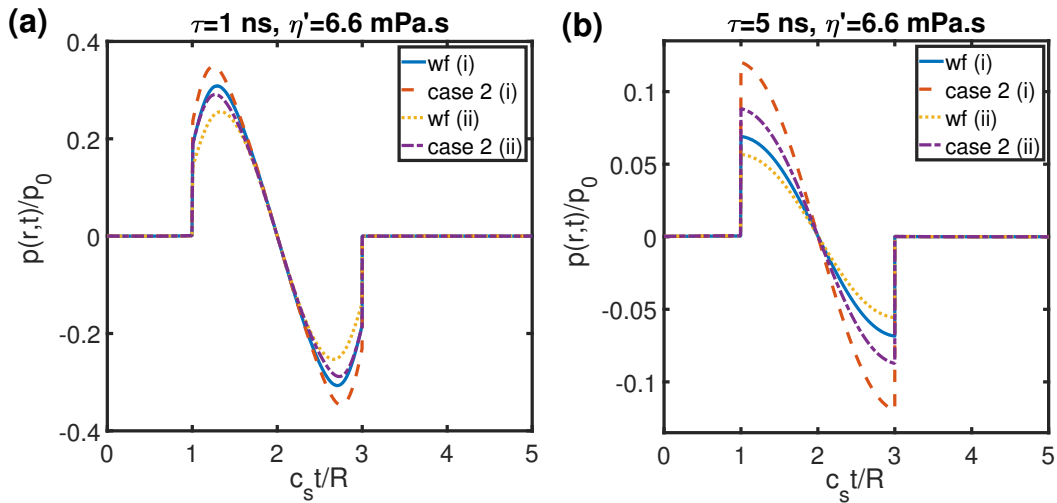
Figure 4.11. Normalized PA wave p(r,t)/p$_0$ generated by three sources for case 2 (dashed line) and without force (wf) (solid line) vs normalized time c$_s$t/R (a) $\tau = 1$ and (b) 5 ns with different beamwidths (i) and (ii) represent $\sigma = 6$ and 8 μm, respectively.) [4, 5].

and 3 allowing to differentiate and characterize their aggregation levels by observing the PA signal amplitude regarding the chosen force corresponding to the values of function of separation between cell surfaces ($\beta(d - r_0)$) as shown in Fig. 4.13. Here, the same points ($\beta(d - r_0)$) for each case correspond to various aggregation forces as shown in Fig. 4.14(d). Our theoretical simulations show that PA signal amplitude increases linearly with increasing aggregation force, which are in excellent agreement with literature data [24, 176, 200, 201]. We use the measured interaction forces for types of Dextran solutions inducing the aggregation in order to validate our analytical approach. Moreover, our results suggest that PA can be used to differentiate red cell aggregation process in detail by using a known interaction force between cells. Firstly, the accuracy of the extended photoacoustic transport model for the characterization of red blood cell morphology in microchannel flow is analyzed with the experimental values in Figs. 4.13-4.15 by taking into consideration the chosen force values for each case (the cases of Dextran 70 and Dextran 150, case 1 and case 3). Moreover, the solution of the extended photoacoustic wave equation for a Gaussian radial absorption profile make it possible to explicitly observe the effect of laser parameters on the PA wave.
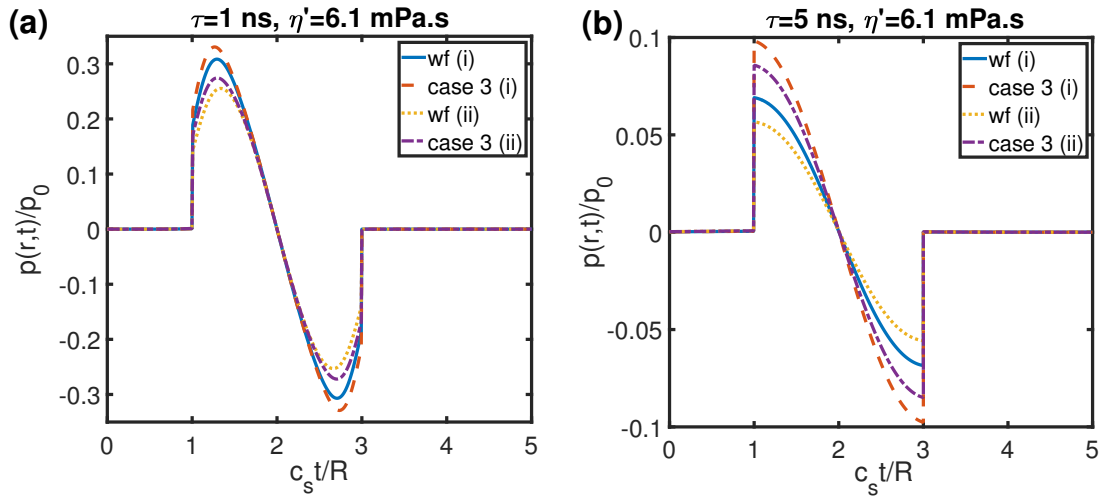
Figure 4.12. Normalized PA wave p(r,t)/p₀ generated by three sources p(r,t)/p₀ for case 3 (dashed line) and without force (wf) (solid line) vs normalized time c_st/R, (a) $\tau = 1$ and (b) 5 ns with different beamwidths (i) and (ii) represent $\sigma = 6$ and 8 μm, respectively; where R = 8 μm (η=1.2 mPa.s, ζ=4.5 mPa.s, η'=6.1 mPa.s) [4,5].
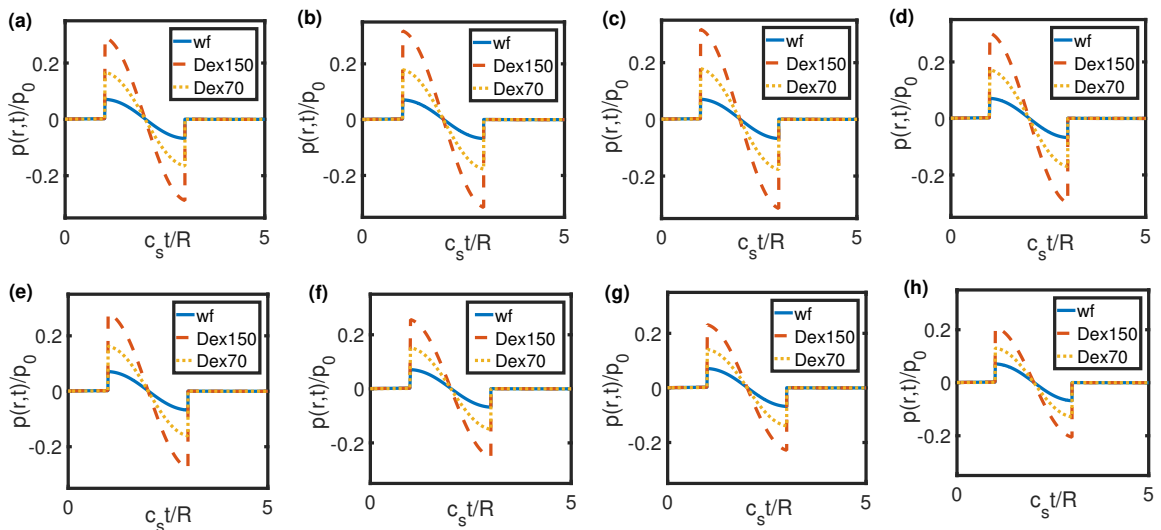
Figure 4.13. Normalized PA waves p(r,t)/p₀ generated by three sources p(r,t)/p₀ for without force (solid line), Dextran 150 (dashed line), and Dextran 70 (dashed line) regarding the chosen force at the values of function of between cell surfaces $\beta(d - r_0)$ = (a) 0.4, (b) 0.6, (c) 0.8, (d) 1, (e) 1.2, (f) 1.4, (g) 1.6, (h) 1.8 vs normalized time.
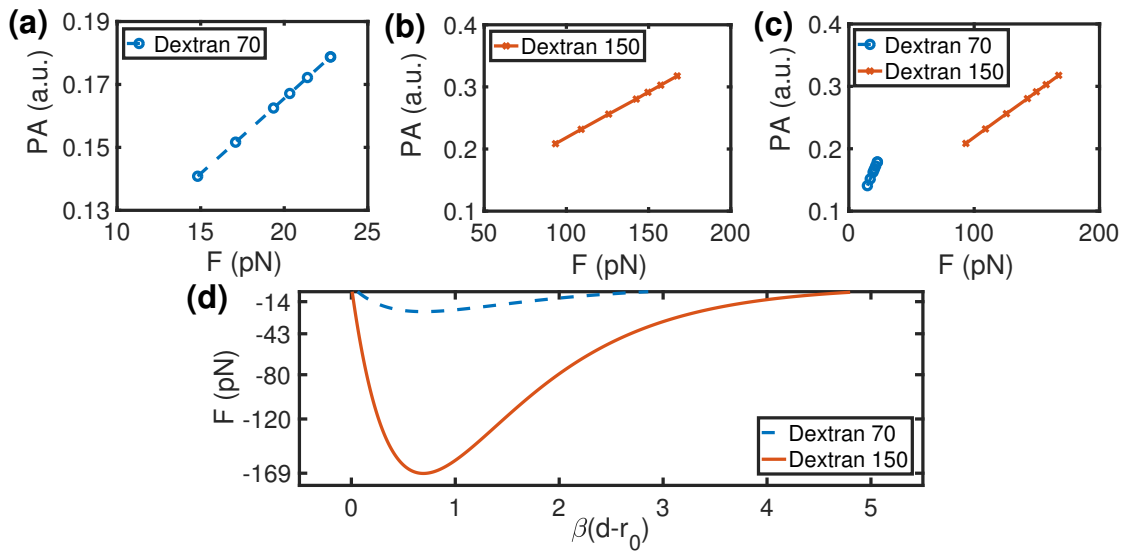
Figure 4.14. Normalized PA wave p(r,t)/p$_0$ for (a) Dextran 70 , (b) Dextran 150 , (c) both Dextran 70 , and Dextran 150 vs the chosen force at the values of function of between cell surfaces, (d) F corresponding to the various aggregation rates vs function of separation between cell surfaces ($\beta(d - r_0)$) for Dextran 70 [3, 7, 8] and 150 [3, 8].
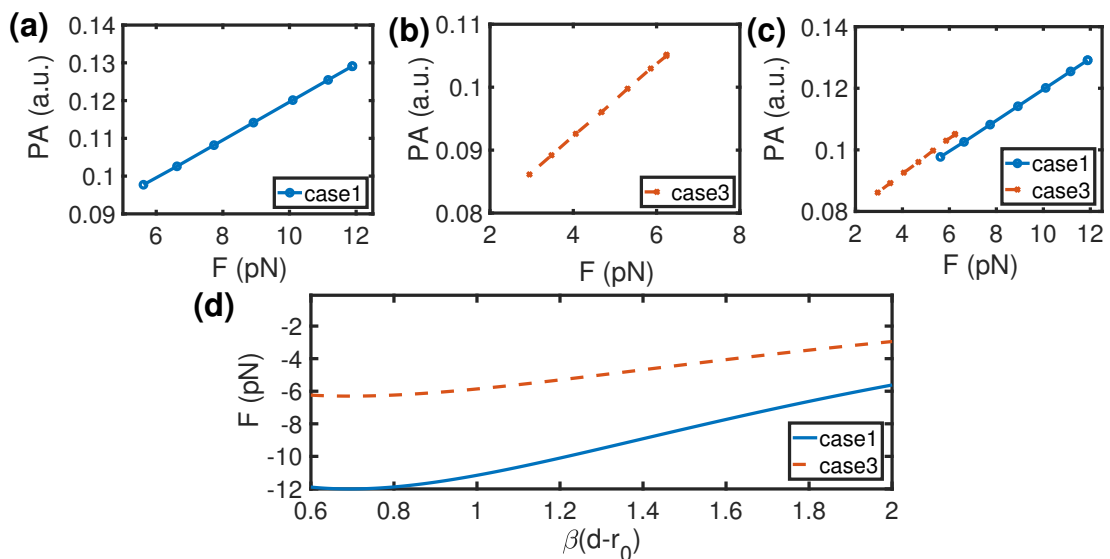
Figure 4.15. Normalized PA wave for (a) case 1 (solid line), (b) case 3 (dashed line), (c) both case 1 (solid line) and case 3 (dashed line) vs the chosen force values, (d) aggregation force (F) corresponding to the various aggregation rates vs function of separation between cell surfaces ($\beta(d - r_0)$) for case 1 and case 3 [1, 2].

4.6. Discussion

The PA imaging may have a great potential for anatomical, functional and molecular imaging of RBCs. In this work, the level of aggregation of RBCs in human blood is assessed and the morphology of blood cells is studied for the detection of RBCs using PA waves obtained analytically. To see the feasibility of the proposed extended photoacoustic transport model including a modified Morse type potential function, an analysis of the amplitude of PA signal is conducted by using the measured aggregation forces [3, 12, 191].

We compare our theoretical results with the previous experimental and simulation studies for the PA detection of RBC aggregation and see that our results are in good agreement with the literature [3, 12, 172, 173, 191]. Our numerical results show that the PA signal amplitude increases with the level of aggregation. Some experimental-simulation studies presented that the PA signals could be used to identify the presence of varying degrees of aggregation [24, 176]. However, many other factors such as effects of flow, intervening tissues, ultrasound transducer receiver bandwidth are essential for the experimental confirmation of this study [176]. In order to analyze PA radiofrequency (RF) signals produced by RBC aggregates, Hysi *et al.* reported the feasibility of detecting these PA RF spectral changes by incorporating a finite transducer in detection of PA signals in his theoretical and experimental study [24]. In our model, the combined Navier-Stokes and PA equation system is solved to find the PA wave by utilizing the immersed boundary method for fluid-structure interaction. Furthermore, our analytical approach shows the effect of the whole blood viscosity on the aggregation processes in the case of third source due to the intercellular interaction force and it also allows to analyze each source separately (If we want to include the interaction force for more than one RBC, then H would be expressed as the summation of the contributions resulted from each RBC.).

In this paper, we solve a combined heat conduction and Navier-Stokes equation system utilizing the Morse-type potential energy function for the characterization of human re d cell. The fluid flow containing RBCs in microvessel is modeled by an

extended Navier-Stokes equation with the immersed boundary method proposed by Peskin *et al.* [202]. The immersed boundary method has been utilized to model the flow of RBCs in blood plasma or to describe the blood plasma and RBC membrane interaction between the flow field and deformable cells [183]. We modified the immersed boundary method with respect to the location of PA detector and radius of PA source in order to obtain the PA wave coming from RBC aggregation. Furthermore, our solution makes it possible to observe the effect of laser parameters on the PA wave because the temporal profile is taken as Gaussian rather than a point like Dirac delta function. To validate our method with another one presented by Erkol *et al.*'s method [186], we also show that the PA signal decreases when the beamwidth decreases and shorter pulse duration leads to a larger wave amplitude as expected. In this regard, adjustment of laser parameters can be very useful for the application of the detection of RBCs.

Another advantage of our method is that it provides comprehensive solutions since the spatiotemporal profile of the laser is taken Gaussian (rather than point source) and RBC aggregation and plasma parameters are taken into consideration. It is well known that blood rheology and viscosity are related to hematocrit (Ht), RBC aggregation, shear induced deformation of RBCs, and plasma viscosity [203–206]. In recent years, several studies have demonstrated that the level of RBC aggregation increases when the plasma fibrinogen concentration increases, which shows the capability of PA for dynamic monitoring of rheological parameters in circulating blood [190, 207–209]. Our results show that aggregation is associated with the whole blood plasma viscosity after RBC aggregation because pressure wave amplitude is promoted by the alteration of whole blood viscosity in the case of third source due to the intercellular interaction force. The plasma viscosity may increase up to five-fold in a unfavorable situation ranging from inflammatory diseases to plasma cell dyscrasias [210, 211]. Therefore, the plasma viscosity is significant in specific cases only although this influence is relatively small in general cases [212–214]. For an application, we studied the red blood cell aggregation in a microcirculatory system. Our detailed analytical solution of the extended photoacoustic transport model combined with a modified Morse type potential function accounts for the dynamics of aggregate formation. Hence, the distinctive features of the photoacoustic waves enable to understand diseased or damaged RBCs

having abnormal shapes and sizes, which can result from a variety of diseases. Our detailed solution of PA wave to detect RBC aggregation is obtained by solving the combined Navier-Stokes and bio-heat transfer equations. This study also presents the spectral features of the PA signals by considering the interaction between RBCs modeled by the Morse potential. We think that our work can be helpful to improve hybrid simulation approach for not only the characterization of red blood cell morphology but also for cancer cell lines in the microchannel flow. To describe and analyze the mechanical processes inside a microfluidic device, our hybrid model can pave the way toward the development of new physical models in the rapidly advancing field of lab-on-chip technology and photoacoustics. As a future work, in order to analyze the influence of the deformation of the membrane on pressure wave, we will implement the spring network approach beside the Morse potential.

4.7. Experiment

4.7.1. Measurement of Interaction Forces Between Red Blood Cells via Optical Tweezers

In order to characterize red blood morphology in microchannel flow mentioned Chapter 3, the methods used to measure aggregation force between RBC cells are represented by following steps.

Sample Preparation for The First Experimental Study: To perform the calibration methods, 5 μm polystyrene spheres were diluted in filtered distilled water. 200 μl of silica particles in filtered water was put between the glass slide with well and cover slide. Moreover, the blood suspension was prepared by adding a drop of whole blood into isotonic solution at a ratio 1:1000.

Sample Preparation for Second Experimental Study: Fresh red blood cells were drawn from people with paroxysmal nocturnal hemoglobinuria disease and healthy ones in measurement day from Istanbul University Faculty of Medicine. Samples were collected into 10 mL EDTA and heparin tubes. These tubes were transported to

Bogazici University in a blood transportation box which contains ice packs to ensure acceptable temperature during for samples transportation. Each sample was diluted at a ratio of 1:1000 using isotonic serum solution. Cover slides to cover the samples were coated with human serum albumin solution whose concentration is 1mg/ 1mL.

Experimental Setup: To observe the behaviour of interaction scheme for two red blood cells, the experiments were performed with a commercial optical tweezer, as shown in Figure 4.16. Furthermore, the experiments will be performed with the second set up for hybrid PAM/OT to measure PA signal and interaction force in microfluidic devices, simultaneously. The second set up is described in Chapter 6.
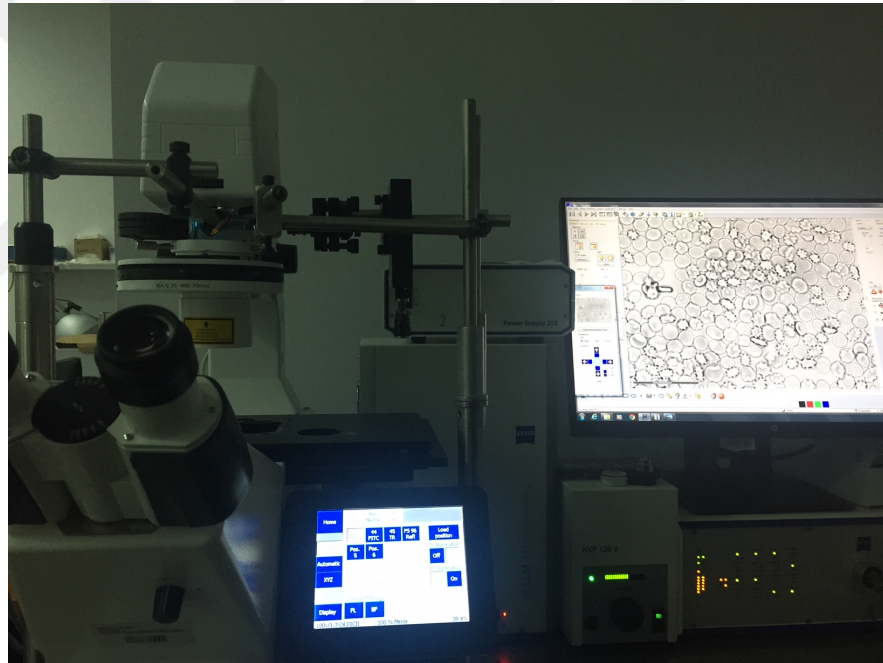
Figure 4.16. The photograph of the commercial Zeiss PALM optical tweezer.

Calibration of the optical tweezers: The stiffness of an optical trap changes uniquely according to various optical trapping (OT) systems. In order to determine the trap stiffness for a commercial (ZEISS PALM MicroTweezers) optical tweezer system, a 5 μm silica particle trapped by the optical tweezers was moved through the medium (distilled water) so that the force measurement will subsequently be achieved by moving the stage with a stationary laser beam. The viscosity of the medium results in a force acting on the bead, which displaces it from the focus of the laser beam. This force acts on the bead like a linear spring, i.e. the deflection from the position of rest is

directly related to the force. According to Stokes' law, the following expressions enable the important relationship between force, viscosity, deflection and the velocity of the movement:

$$F = kx \tag{4.51}$$

and

$$F_{stokes} = 6\pi r \eta v, \tag{4.52}$$

where k, x, r, η, v are defined as trap stiffness, deflection, radius of bead, viscosity of medium, and the velocity. By using these two equations, the trap stiffness, k was calculated, measuring bead radius, velocity, viscosity and deflection at different laser powers. During the application of various laser trapping powers, the trap stiffness was calculated by finding the slopes of lines from Figure 4.17 that represents the relationship between deflection and speed. In order to carry out an appropriate calibration, the trap stiffnesses of silica particles were calculated at the same height to avoid any contribution of spherical aberration on trap stiffness that depends on the distance from the coverslip for each trapping. After that, the trap stiffness for our system was determined as 18.70xP+ pN/μm for the laser powers P ranging from 450 mW to 750 mW, that can be seen in Figure 4.17. Moreover, Table 4.5 is summarized power dependence of stiffness. In Figure 4.18, the trap stiffness of the optical trap in water was shown to be directly proportional to the laser power, as expected.

Firstly, the sample preparation for the first experimental study was used. In this experiment, while most of the blood cells were settled down, some of them were seen floating lively under the microscope. After completing the calibration procedure as mentioned above, one red blood cell was trapped, and the behavior of the graph representing deflection towards x-axis vs time was obtained, shown in Figure 4.19. Note that the particle was not disrupted by other particles in a boundary of the trapping region. To observe the interaction force between two RBCs, the trapped RBC was
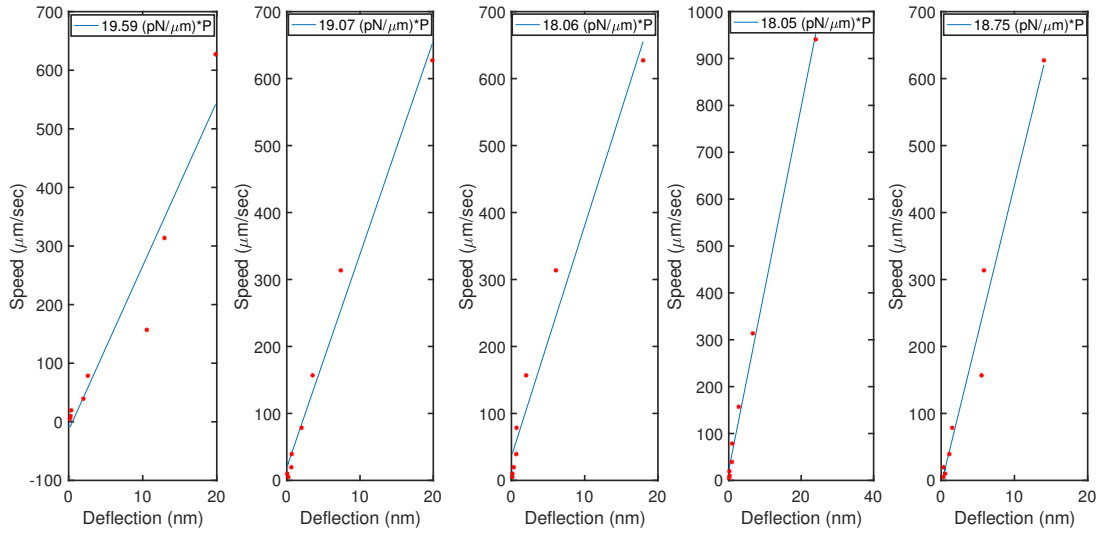
Figure 4.17. The relationship between deflection vs speed. Each graph is obtained at different laser trapping powers.
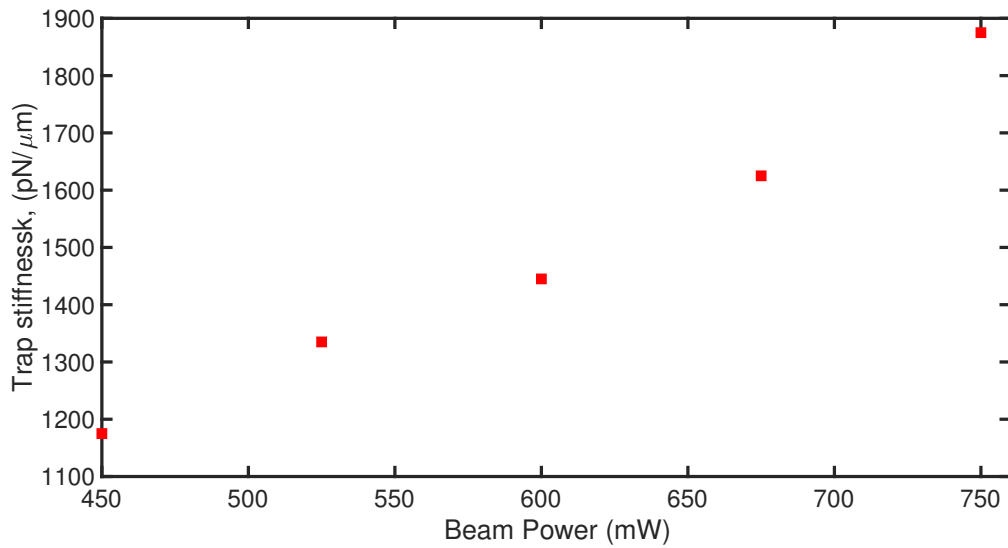
Figure 4.18. Linear graph of the trap stiffness versus beam powers.
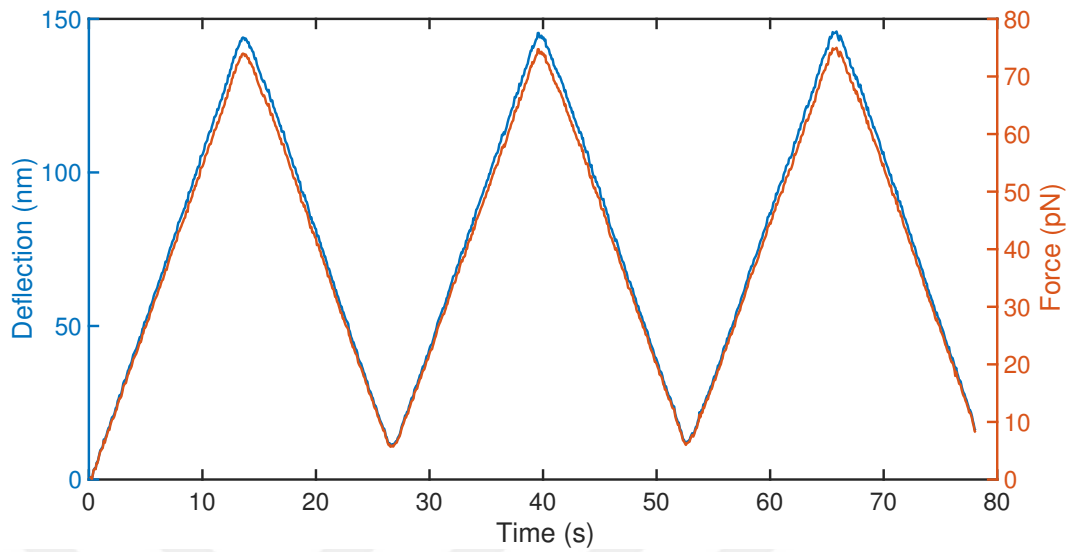
Figure 4.19. The behaviour of the deflection and the calculated force as a function of time.
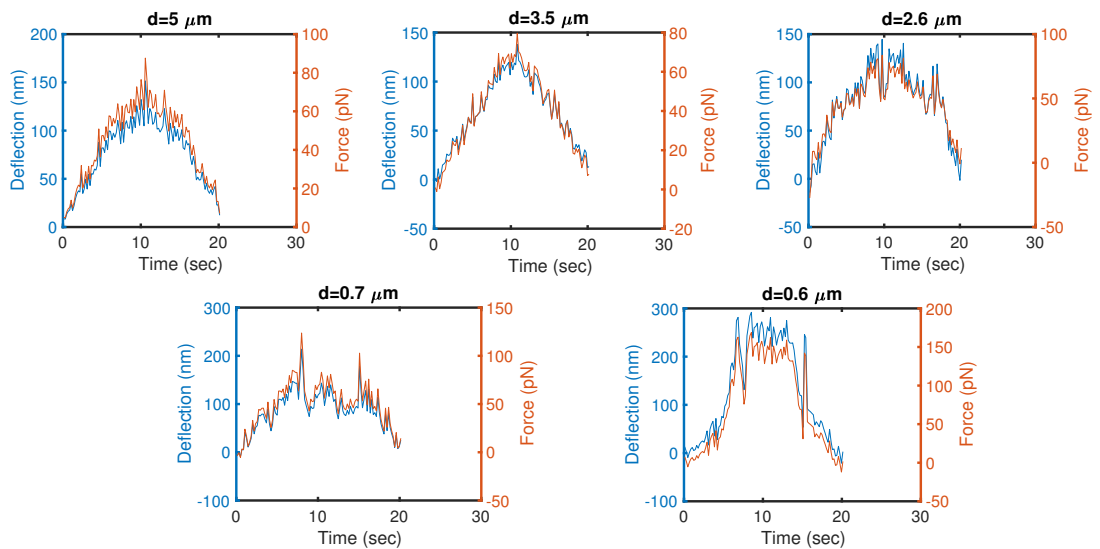
Figure 4.20. The behaviour of the deflection and the calculated force as a function of time when the distance between two RBCs decreases from 5 μ m to 0.6 μ m.
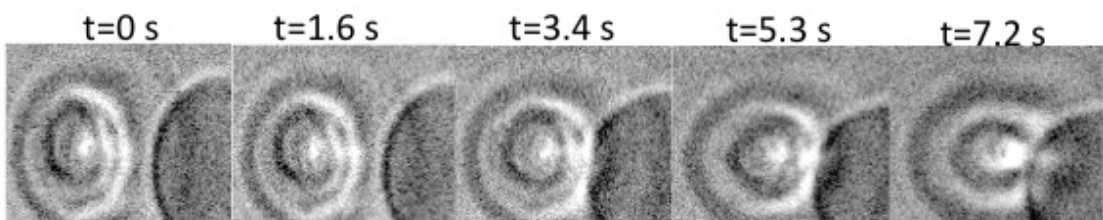
Figure 4.21. Stages of aggregation process with time.

Table 4.5. Trap stiffness for various beam power of a 5 μ m trapped polystyrene bead for x-direction.

Beam Power (mW)	Trap stiffness, k (pN/μ m)
450	1175
525	1335
600	1445
675	1625
750	1875

moved to close one of the adherent cells on a glass slide. Here, the force was measured between two red blood cells as a function of the distance between their surface. The distance between two surfaces of RBCs were determined as 5, 3.5, 2.6, 0.7, 0.6 μm. As can be seen in the Figure 4.20, when d=0.6, the interaction force could be measured clearly. We know that the net force on the trapped particle provides the deflection. The net force on the trapped RBC can be given as below:

$$F_{net} = F_{trap} + F_{Agg}. \tag{4.53}$$

The aggregation force range is changed according to zero force distance regarding each blood sample. [9] The trapped particle stays under the attractive force when it almost touches the other one. The design of the experiment includes the movement of the beam along the x-axis to the right with velocity 1 μm/s for 10 s and to the left with the same velocity for the same time, shown in Figure 4.20. This means that the particle should follow a linear motion about 10 seconds and then when two particles are close to each other, the net force will increase. Because the total movement is 10 μm, the trapped cell should travel more than 9 μm within the other cell. During these times, a net force is supposed to be constant unless a sudden rotation or unexpected shape change takes place in any of the cells. Then whenever the trapped particle gets out of the aggregation field, that is to say, a little far away from the second trapped cell,

it follows the linear motion again, this time in a negative direction. This behavior explains the graph in Figure 4.19. Figure 4.21 was obtained from the experiment at d=0.6 μm, and the images recorded by CCD in this figure represents the schematic sequences of interaction force. The blood suspensions were obtained from a patient with endometriosis which is prone to familial aggregation.

For the second experimental study, the albumin was used to avoid adhesion and morphological changes in the cells resulted from their interaction with the glass surface. To measure the interaction force between two cells, a double-beam tweezer was used. In that case, the first trapped RBC through the first beam was moved through the second particle which was fixed by the second beam. In the experiment, the particle moved along the x-axis to the right with velocity v =0.4 μm/s for 13 seconds, and two the left for the same velocity for the same seconds. This movement was repeated three times. After evaluating these two methods mentioned above, the results are similar, but the results obtained from the second method do not include the morphological changes in the cells coming from their interaction with the glass surface, so using the second method is a correct way for measuring the aggregation force. Figures 4.22a and Figures 4.22b show the interaction force between two cells taking from a control group of paroksismal noktürnal hemoglobinüri (PNH) patient and PNH patient, respectively. The aggregation levels were extracted from the linear behavior of the cells. As can be seen in Figure 4.22c, we observed the specific aggregation behavior in PNH patient and measured as 160 pN.
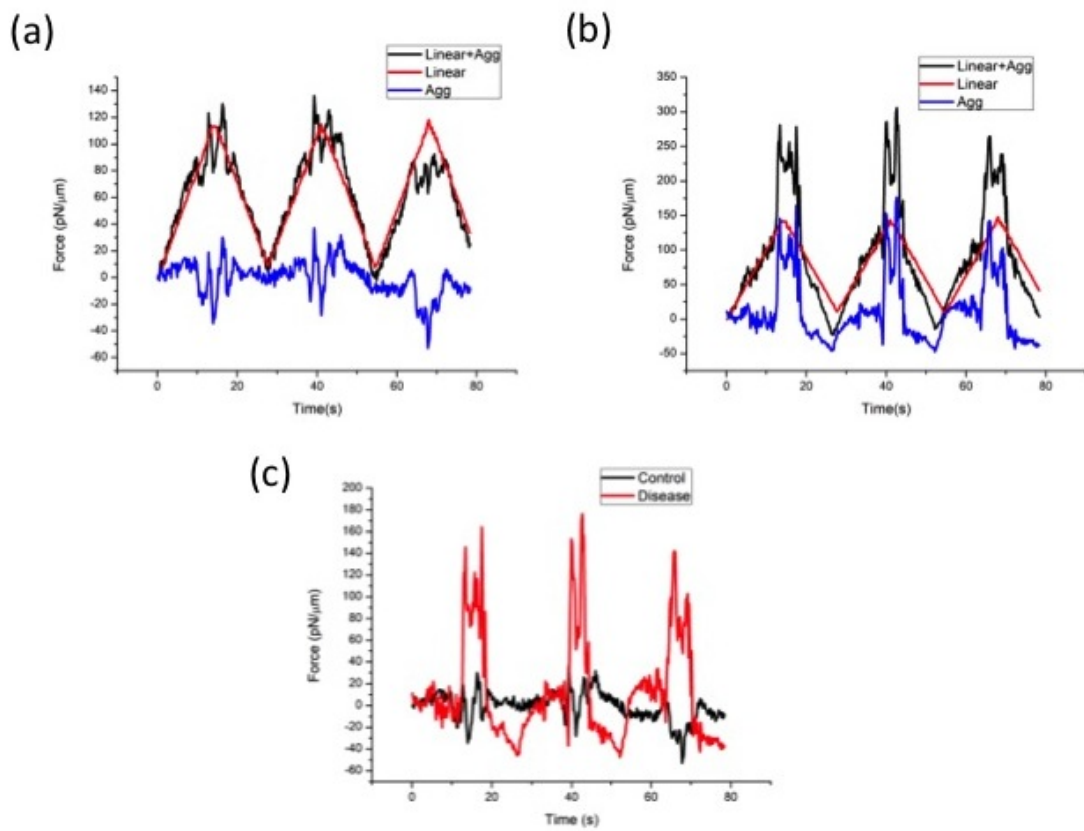
Figure 4.22. The interaction force between two cells taking from (a) healthy control groups, (b) PNH patient, (c) the comparison of aggregation levels which belong to these two groups.

5. A PHOTOACOUSTIC MICROSCOPY SYSTEM FOR MOLECULAR IMAGING OF ANGIOGENESIS

Non-invasive photoacoustic imaging technique can monitor molecular processes associated with the tumor angiogenesis. By this way, evaluation of novel antiangiogenic and proangiogenic therapies as well as early detection of the disease can be possible. The expressions of some specific MMPs are essential for angiogenesis and have been found to be upregulated in every type of human cancer and correlates with stage, invasive, metastatic properties and poor prognosis [33, 34]. In order to detect a specific enzyme involved in angiogenesis, some smart probes which are activated by this enzyme can be used in this study.

5.1. Classification of MMPs

According to the latest research, there are 28 matrix metalloproteinases in a human body which are named as MMP-1, MMP-2, MMP-3, MMP-7, MMP-8, MMP-9, MMP-10, MMP-11, MMP-12, MMP-13, MMP-14, MMP-16. These are classified into five main groups: Collagenases, Gelatinases, Stromelysins, Matrilysins, Membrane-Type MMPs. The important groups are shown in Figure 5.1 [215].

5.1.1. Collagenases

It includes the first family of MMPs, comprising of MMP-1, MMP-8, MMP-13, and MMP-18. The ability is to cleave interstitial collagens I, II, and III at a specific site, three-fourths from the N terminus. Moreover, they can digest many ECM and non-ECM molecules [215].

5.1.2. Gelatinases

It includes two MPPs, MMP-2 and MMP-9 which are called gelatinase A and gelatinase B, respectively. The ability is to digest the denatured collagens, gelatins, as well as to degrade all components of ECM. Note that gelatinases is an essential factor to target for cancer therapy because of their massive upregulation in malignant tissues [215].

5.1.3. Stromelysins

It includes two MPPs, MMP-3 and MMP-10 which are called stromelysin 1 and stromelysin 2, respectively. Both stromelysins 1 and 2 have 2 Specificity of Binding with Matrix Metalloproteinases 37 similar substrate specificity. Besides MMP-3 and MMP-10, MMP-11 is also called stromelysin 3, but it is usually grouped with other MMPs due to the fact that its sequence and substrate specificity significantly differ from those of MMP-3.

5.1.4. Matrilysins

It includes two MPPs, MMP-7 and MMP-26 which are called Matrilysin 1 and Matrilysin 2, respectively. The ability of Matrilysins (MMP-7 and MMP-26) is to digests a number of ECM components.

5.1.5. Membrane-Type MMPs

Six MMPs, namely, MMP-14, MMP-15, MMP-16, MMP-17, MMP-24, and MMP-25, are named as membrane-type MMPs (MT-MMPs) belong to this group. The ability is to activate pro-MMP-2, except MT4.

The seven MMPs, MMP-12, MMP-19 to MMP-23, and MMP-28, have not been classified. But all of them play a great role in the degradation of ECM. MMPs have critical role in cancer progression.
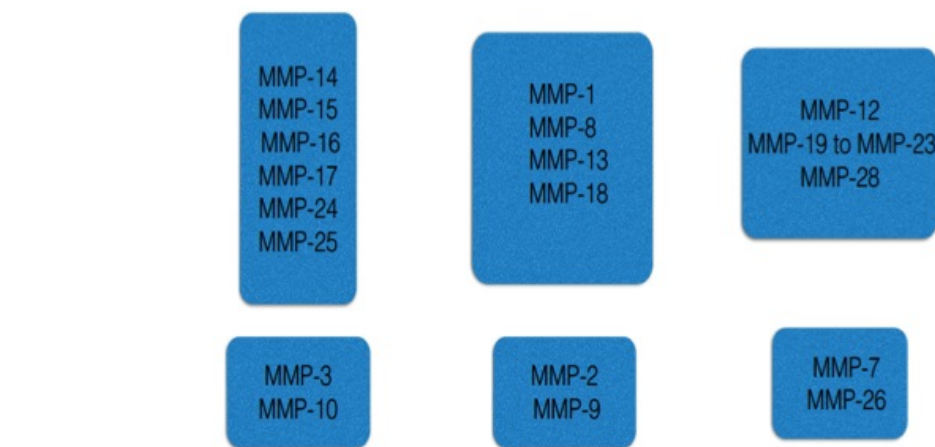
Figure 5.1. The representative table for classification of MMPs.

5.2. Roles of MMPs in Angiogenesis

The expressions of some specific MMPs are essential for angiogenesis and have been found to be upregulated in every type of human cancer and correlates with stage, invasive, metastatic properties and poor prognosis. The expression of MMPs by the tumor cells themselves or by surrounding stromal cells enables to remodel the ECM and release ECM- and/or membrane-bound growth factors, thus a favorable microenvironment in order to establish primary tumor occurs. While tumor grows, an angiogenic switch opens in which the balance of proangiogenic factors (e.g., bFGF and VEGF) overcomes the expression of angiogenic inhibitors. For examples, the gelatinases can degrade basement membrane components and cause the tumor cells to invade into the adjacent stroma in the case of up-regulation of MMP expression. The breakdown of the basement membranes related to capillaries and lymphatic vessels is actualized and the conditions permit the tumor cells to enter the circulation. Both MMP-2 and MMP-9 have been demonstrated that they are the induction of the angiogenic switch in different cancer models [32].

5.3. Multispectral Photoacoustic Imaging Detection of Matrix Metalloproteinasesin Vitro

Photoacoustic (PA) imaging has been used to obtain noninvasively higher spatial resolution and deeper penetration depth compared with most optical imaging techniques. In PA imaging, light which is absorbed by certain endogenous molecules, such as hemoglobin, or exogenous contrast agents, e.g. small molecule dyes, gold nanoparticles, single-walled carbon nanotubes (SWNT), copper nanoparticles etc., converted into heat, resulting in thermoelastic expansion and thus ultrasonic (US) waves. [15–18, 216, 217] The US waves, which scatter much less in biological tissue compared to optical waves, are recorded by transducers and the detected photoacoustic signals generated are used to obtain a map of the absorbed energy in the medium. It allows for a high-spectroscopic contrast of optical modalities with high ultrasonic resolution in deep tissues [72–75].

Photoacoustic microscopy has the ability of identification of cancer cells in vitro and in vivo, and paves the way to enhance cellular details such as anatomical, biomechanical, and functional properties. [218, 219] However, it is a challenge to image most cancer cells which lack sufficient endogenous contrast using photoacoustic microscopy. In order to allow new applications of photoacoustic imaging, and enhance sensitivity, exogenous contrast agents including dyes, plasmonic nanoparticles are needed besides hemoglobin, melanin. [43, 220] Although there are significant works on photoacoustic contrast agents in the literature, a new generation of targeted contrast agents is essential to increase PA imaging signal at the site of target expression. [42] Exploring new biomarkers with the properties such as stability, biocompatibility, specificity for a biological target of interest brings a significant promise to obtain a great extent resolution and depth limitation of photoacoustic imaging. [221, 222] For these reasons, novel tissue-simulating phantoms have been utilized increasingly to investigate specific contrast agents and to make them ideal and promising contrast agents before conducting animal experiments. [223–235]

Numerical materials with stable optical and acoustic properties are used to create phantoms for requirement of routine quality control to understand reproducibility over time, image reconstruction performance, optimization of signal-to-noise ratio, comparison the detection limits and spectral accuracy of different system designs, understanding the maximum achievable depth of penetration for in vivo imaging within the fast-growing field of photoacoustics [226, 236]. Some accurate tissue-mimicking phantoms such as gelatin based and bovine gelatin phantoms are constructed by adding India ink, whole blood, copper/nickel chloride and fluorescent dyes (Direct Red 8, Evans blue) in order to provide optical absorbing for increasing numbers of both preclinical and clinical applications of combined PA and US imaging. [225, 229, 235, 237] Although these materials for photoacoustic phantoms, based on hydrogels, are optically transparent, and have acoustic characterization of sound speed similar to biological tissue, as well as enable ease of preparation, these types of phantoms have a limited re-use capability owing to their low- temperature stability at physiological conditions, resulting in structural integrity loss. [235] Another drawback of using agar and agarose gel as phantom is that the concentrations of these materials used show the changes in the speed of sound. Moreover, some absorbers such as copper or nickel ions were discovered to react with aqueous gels. [237]

Poly(vinyl alcohol) (PVA) gels were described as solid photoacoustic breast phantoms by Kharine *et al.* [231]. A variety of procedures were employed for gel reinforcement by increase in the cross-linking between the polymer chains to construct a higher dimensional network structure. However, the phantom which is only sensitive to humidity takes a long time to prepare through repeated freeze-thaw cycling. [223] This phantom is prepared with an adjustable amount of scattering inclusion, but it was rather heterogeneous due to differential heating and cooling rates. [230] Instead of using water-based materials (gelatin, agarose) and PVA gels as photoacoustic phantoms, polyvinyl chloride plastisol (PVCP) that is synthesized from vinyl chloride monomers and insoluble in water is considered as a further phantom material. Spirou *et al.* first presented the utility of PVCP phantoms in a PA context. [228] The PVCP based tissue-mimicking phantom has a long-term stability with structural rigidity, as well as its Gruneisen parameter is greater than expected in tissue, which benefits to increase

the signal-to-noise ratio of the photoacoustic measurements. Besides these advantages, it has a higher acoustic attenuation than tissue, and the total time for its preparation method is non-trivial [225].

A polydime-thylsiloxane (PDMS), a silicone-based polymer, can be incorporated into phantoms with wide range of geometries for photoacoustic applications. Compared to solid phantoms on the base of hydrophilic gels such as gelatin, agarose, agar-agar, the PDMS phantom has the unique capability to evaluate water-soluable materials such as dyes, contrast agents which enhance photoacoustic imaging. While creating microchannels within hydrogel structures is a great challenge, the PDMS has elastomeric properties and optical transparency that make it possible to design the microfluidic channels and chambers with various geometries by using soft lithographic techniques. PDMS stiffness and hardness could be adjusted by changing the ratio of pre-polymer base to curing agent, hence the PDMS phantom is a promising tool to achieve to obtain Young's modulus for various types of tissues. Therefore, the PDMS is regarded as suitable for phantom in respect to image quality assessment of photoacoustic microscopy. [40, 41, 238, 239]

The purpose of this work presented here is to design and develop a polydime-thylsiloxane (PDMS) device for evaluation of the performance of a multispectral PA imaging system using MMP680 and MMP750 probe senses which are labeled as activatable "smart" probes. The presence of both MMP-2 and MMP-9 defined as the induction of the angiogenic switch in tumor angiogenesis is investigated with PAM by means of activation-dependent absorption changes. [33, 34, 240] We create a novel thin PDMS that has various channel widths and depths to mimic blood vessels and evaluate two photoacoustic smart probes in vitro by loading a series of monolayers of different cell lines in vitro that would cleave and activate the probes into the microchannel. The image of smart probe accumulation in vitro with the help of smart microfluidic platforms in the field of photoacoustic is the first study in the literature. The study may help pave the way for investigating the efficiency in the development of new photoacoustic contrast agents, as well as new drug candidates, and monitor treatment response in vitro before conducting animal experiments.

5.3.1. Absorption Spectrum of Optimal MMPSense680 and MMPSense750 Concentrations

MMPSense680 and MMPSense750 contrast agents were purchased from PerkinElmer, Inc (Waltham, MA). MMPSense 680 is protease activatable fluorescents in vivo imaging agent that is activated by important several MMPs including MMP-2, -3, -9, -13. MMPSense 750 is activated by not only the groups of MMPs mentioned for MMPSense 680, but also MMP-7, -12. Although these probes are used for in vivo application, they can be used for in vitro if the optimal concentrations of them are discovered. In order to find out the optimal concentrations, the probes were activated using 100 μ M Trypsin. It produces similar cleavage behavior with MMP-9. After 4 h incubation at room temperature, the absorption spectrum of both the activated and inactive control solution for both contrast agents were measured in double concave microscope blank glass slides using a VIS–NIR spectrometer (AvaSpec-ULS3648), as shown in Figure 5.2 and Figure 5.3, respectively, which in turn was used as an input spectrum to be used for multispectral post-processing of PA signals. The measured absorption spectra of both MMPSense680 and MMPSense750 have differences between the inactive and active states. Compared with MMPSense 680, MMP Sense 750 is efficiently accumulated in cells because of the enhanced permeability effect. Therefore, it is more convenient for the evaluation of the potential therapeutic efficacy of drugs targeting.
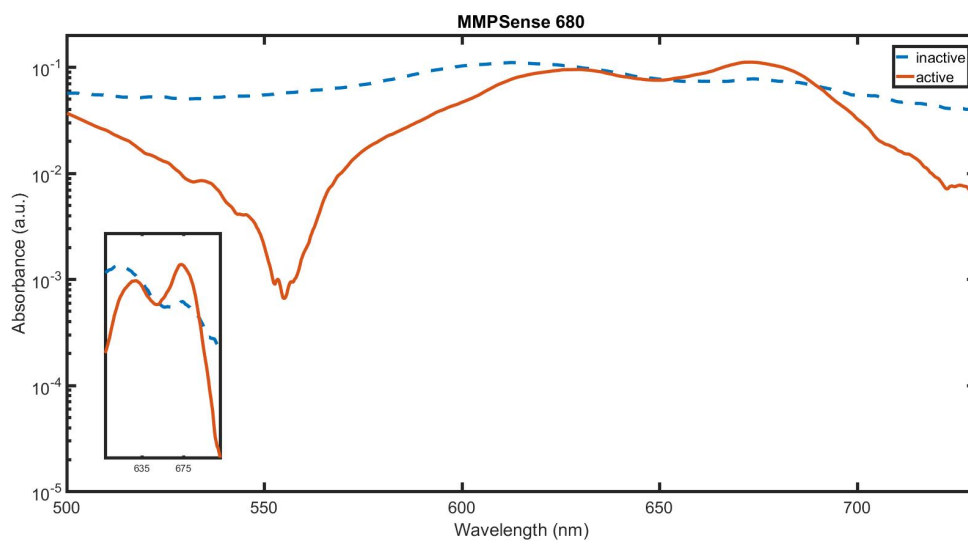
Figure 5.2. Measured absorbence spectrum of inactive (dotted line) versus activated (solid gray line) MMPSense^{TM} 680 probe.
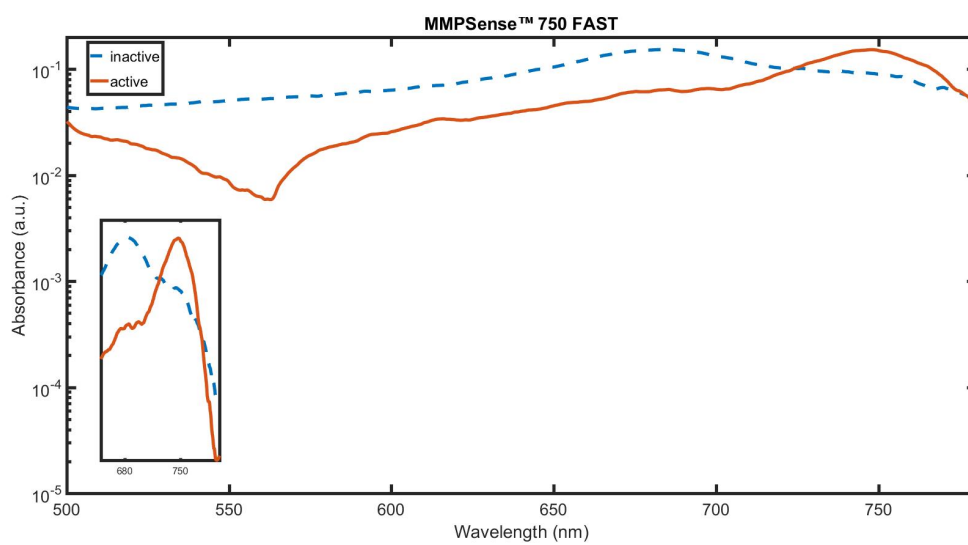
Figure 5.3. Measured absorbence spectrum of inactive (dotted line) versus activated (solid gray line) MMPSense^{TM} 680 probe.

5.3.2. Confocal Microscopy

HT-1080 cell seeding on coverslip containing 6-well plate is done. After 4hrs incubation in 37 °C CO^2 containing incubator, concentration 1 and concentration 2 MMPSense 680 is added to separate wells containing cells. Fixation is done with 4 % PFA. DAPI staining (for nucleus staining) is done as 0.02. Coverslips are closed on a lamel containing a mounting medium. Cells under two glass slides are observed under confocal microscopy at 638 nm. MMP-2 positive (HT-1080, human fibrosarcoma, MeWo, skmel28) from MMP-2 negative (THP-1 (Undifferentiated)) cell cultures testing of an MMP-activatable is shown in Figure 5.4. Each figures (The Figures 5.6-5.14) illustrate two channel separately and then a merged channels. Compared with the negative and positive control groups which are untreated Thp-1, ht1080, MeWo, skmel28, and treated Thp-1, ht1080, MeWo, skmel28, we observed the signals coming from treated ht1080, MeWo, and skmel28, as expected. Moreover, the confocal analysis shows that MMP-2, 3, and 9 were observed regarding with the human protein atlas, shown in Figure 5.5. Figure 5.9 shows that strong MMP680 fluorescence signals were observed in the cytoplasm of MMP2-positive Ht1080 cells after 4 h of incubation. Moreover, the same experiment was repeated for microfluidic devices, and the similar results were obtained.

5.3.3. Cell Culturing and Sample Preparation

The human malignant cancer cell lines Ht1080, THP-1, Sk-Mel-28, MeWo, Hela have obtained the American Type Culture Collection (ATCC). Cells were grown in Dulbecco's modified Eagle medium (DMEM) containing 10 % fetal bovine serum (FBS). MEM Non-Essential Amino Acids Solution and Penicillin-Streptomycin mixture were added to the medium to increase cell growth and viability and prevent contamination, respectively. For cell maintenance, cells were cultured on 100 mm tissue culture dishes with 10 mL growth medium at 37 °C in a % 0.05 trypsin with EDTA every two days. For loading of PDMS, cell lines were counted using Countless II FL Automated Cell Counter with a hemocytometer. In order to prepare a certain concentration of cells, the counted cells were centrifuged at 2000 rpm for 2 minutes and diluted with the
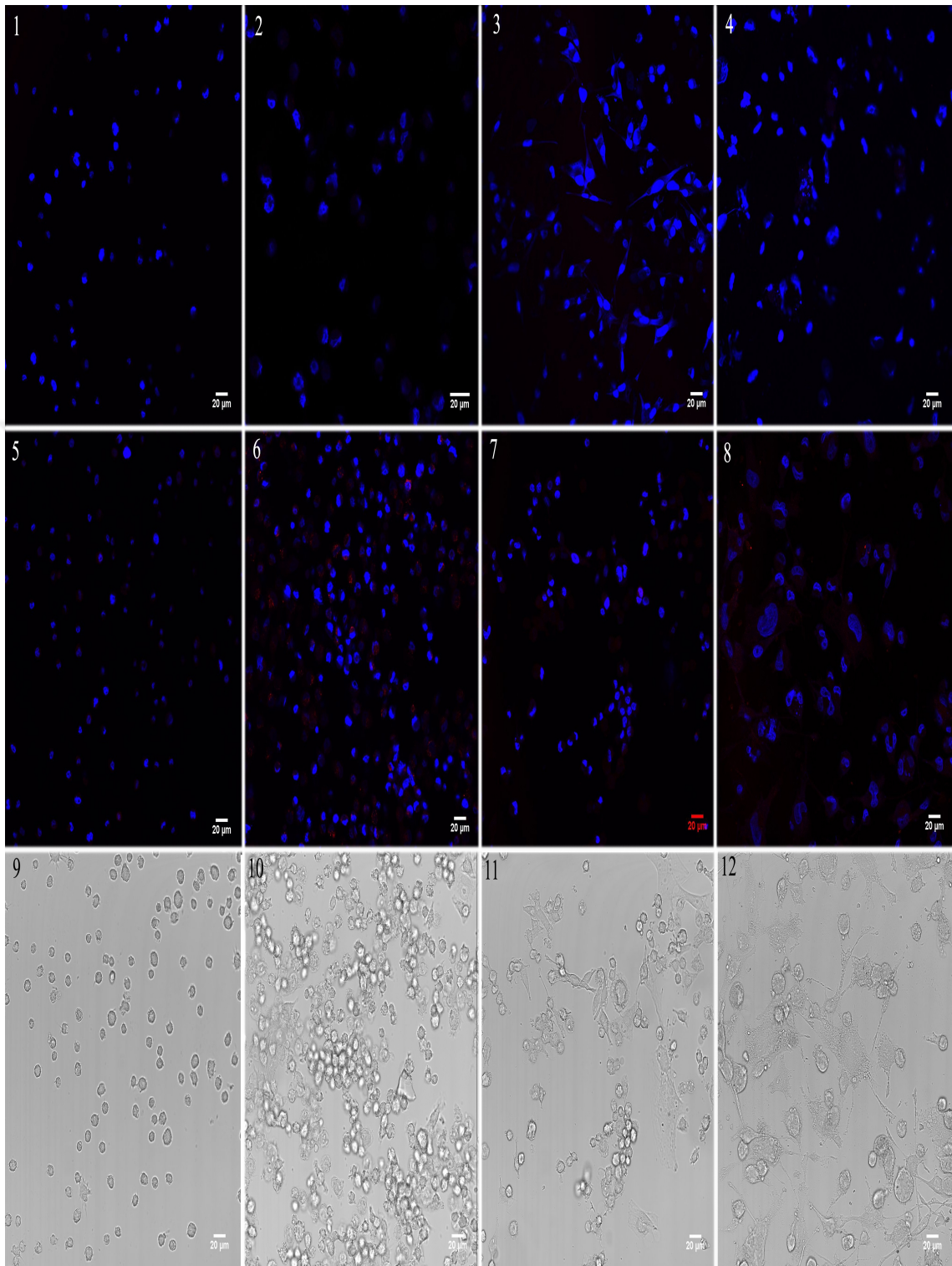
Figure 5.4. The first column of figures shows the confocal image of control groups (1.Thp-1, 2.ht1080, 3.MeWo, 4.Skmel-28), the second column of the figure shows the treated cells with MMPSense 680 probe (1. Thp-1+ MMPSense680, 2. Ht1080+ MMPSense680, 3. MeWo+ MMPSense680, Skmel28+ MMPSense680), the third column of the figure shows the the dark field image (1. Thp-1, 2. Ht1080, 3. MeWo, 4. Skmel28). The probe, cell nuclei are indicated in blue and red, respectively.
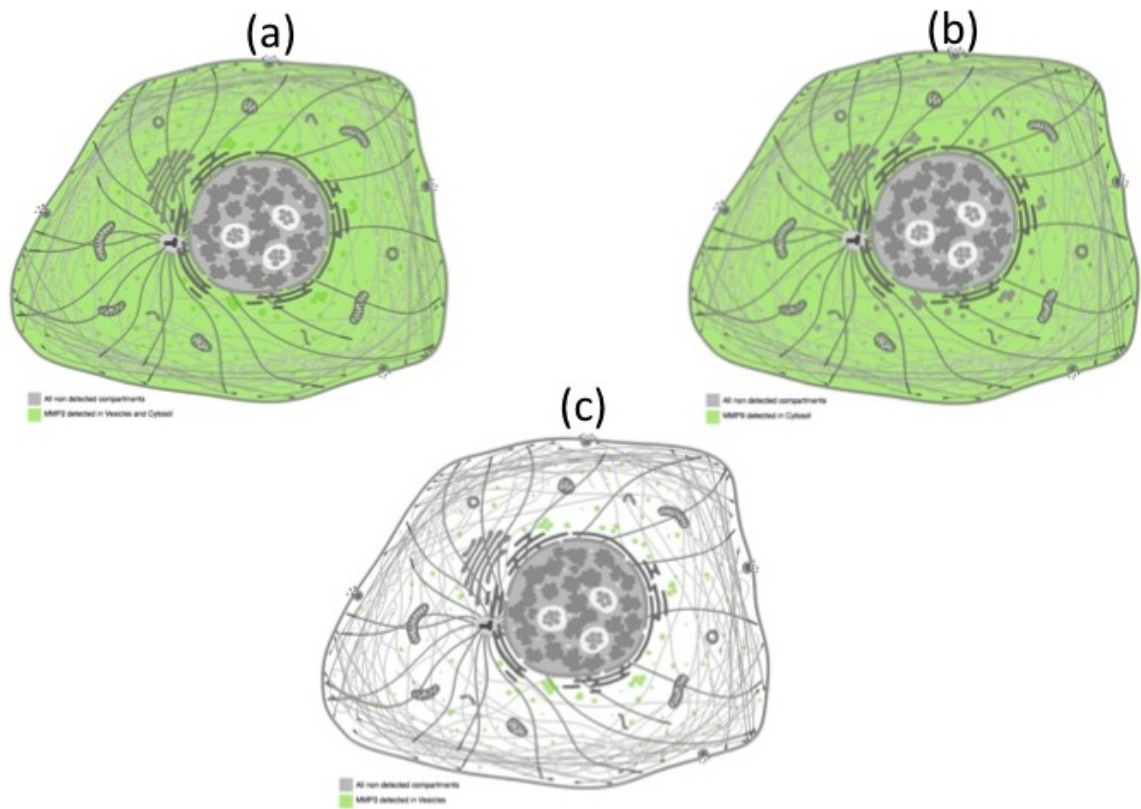
Figure 5.5. The humon protein atlas for (a) MMP2, (b) MMP9, and (c) MMP3. Note that the colour-coded with green represents that MMP2, MMM3 and MMP9 detected in vesicles and cytosol.

Figure 5.6. Photoconversion of DAPI to red fluorescence. Fixed and permeabilized Thp-1 cells stained with DAPI were imaged by confocal microscopy. Note that the excitation/ emission were 638 nm/643-717 nm

Figure 5.7. Photoconversion of DAPI and MMP680 probe in the Thp-1 cells. Note that the excitation/ emission were 638 nm/643-717 nm
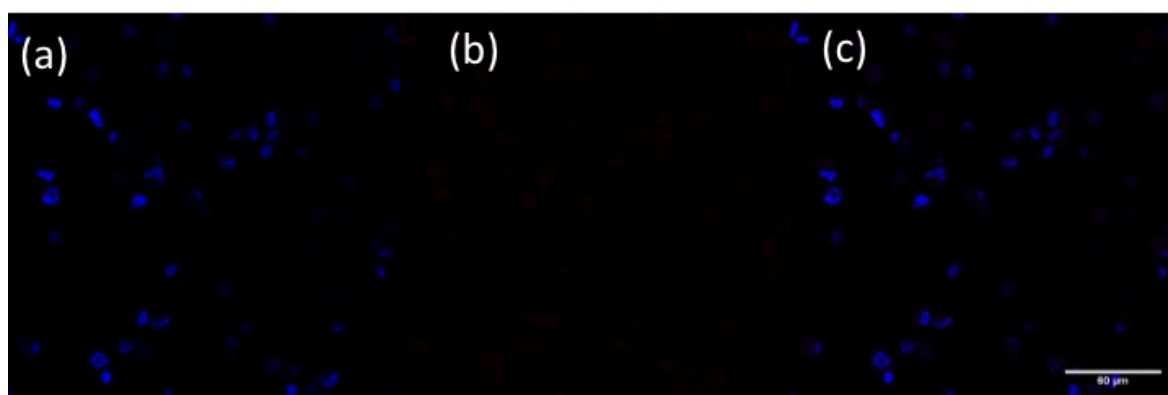
Figure 5.8. Confocal microscopy images of ht1080 cells stained by DAPI dyes for control group (a) dapi, (b) MMPSense 680 probe, and (c) merged merged images of DAPI with MMP680Sense probe. Note that the excitation/ emission were 638 nm/643-717 nm.
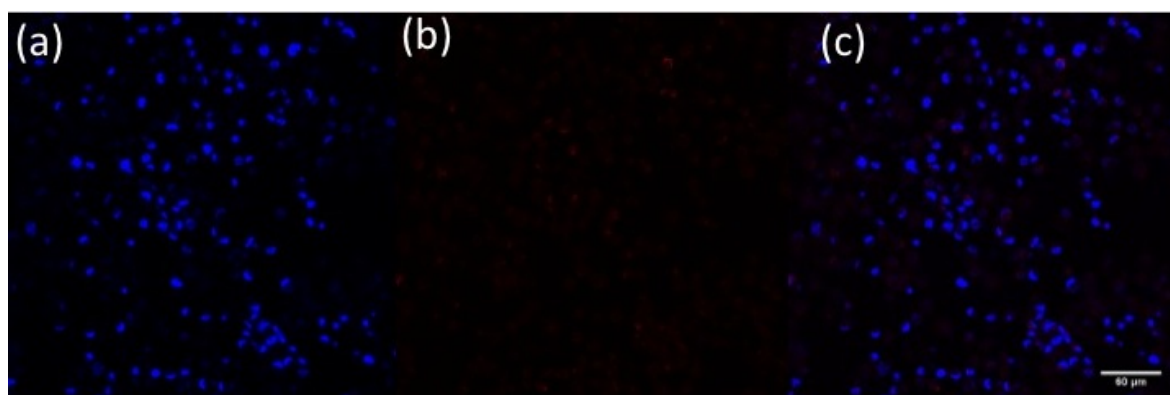
Figure 5.9. Confocal microscopy images of ht1080 cells stained by DAPI dyes after adding MMPSense 680 (a) dapi, (b) MMPSense 680 probe, and (c) merged images of DAPI with MMP680Sense probe. Note that the excitation/ emission were 638 nm/643-717 nm
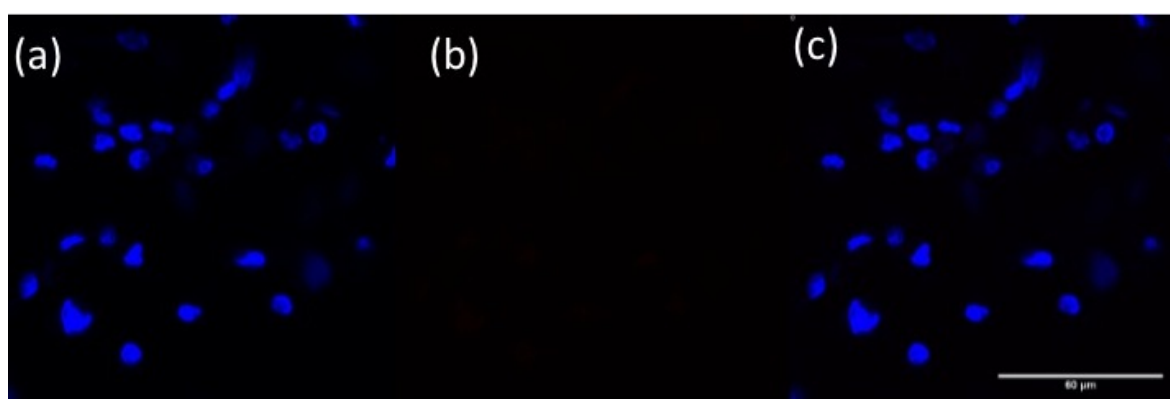
Figure 5.10. Confocal microscopy images of MeWo cells stained by DAPI dyes for control group (a) dapi, (b) MMPSense 680 probe, and (c) merged images of DAPI with MMP680Sense probe. Note that the excitation/ emission were 638 nm/643-717 nm.
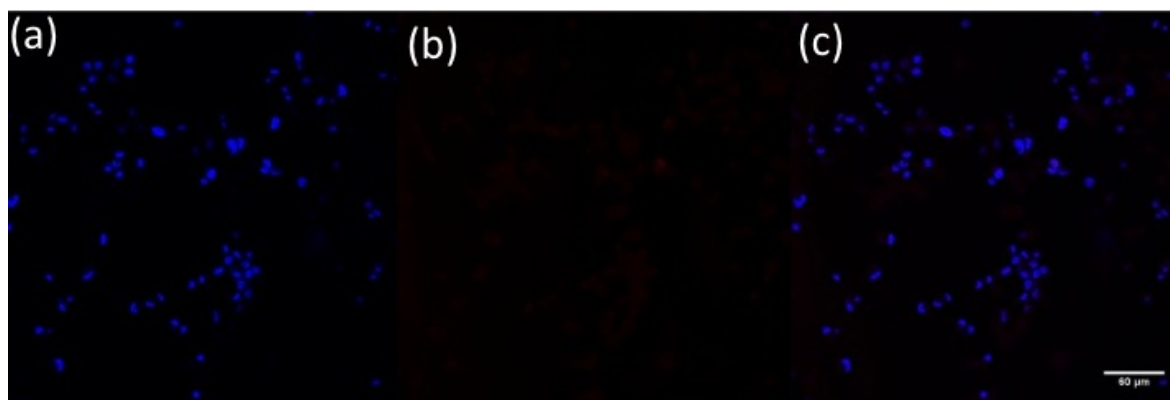
Figure 5.11. Confocal microscopy images of MeWo cells stained by DAPI dyes after adding MMPSense 680 (a) dapi, (b) MMPSense 680 probe, and (c) merged images of DAPI with MMP680Sense probe. Note that the excitation/ emission were 638 nm/643-717 nm.

corresponding volume of PBS.

5.3.4. Results and Discussion

We investigated the PA signal intensity for two group of cells within two channels, shown in Figure 5.15. The part of the probe is activated to penetrate the cell wall and accumulated in the cells after the cleavage needed to be labeled with a chromophore that shows the greatest photoacoustic signal. In order to detect the activated probe, the photoacoustic signals coming from cell clustering were acquired at wavelengths of 680 nm. Although the cells were washed with PBS twice, the inactivated probe may be available in cell medium. This undesirable situation was observed under confocal microscopy. Therefore, the photoacoustic signals were acquired at wavelengths of 630 nm. If the inactive probe is available, it produces higher PA signal at the wavelength of 630 nm than the PA signals coming from the activated probe at the wavelength of 680 nm. In this case, subtraction of the image taken at 680 nm (Figures 5.16d,e) and 630 nm resulted in an image (Figures 5.16b,f) is a correct way to detect the activated probe by MMP-2,3, or 9, shown in Figure 5.16g.

The detection of MMPs in the cells was realized by using acoustic microscopy. We used optic microscopy to confirm the position of Ht1080 cells inside the plate. Figure
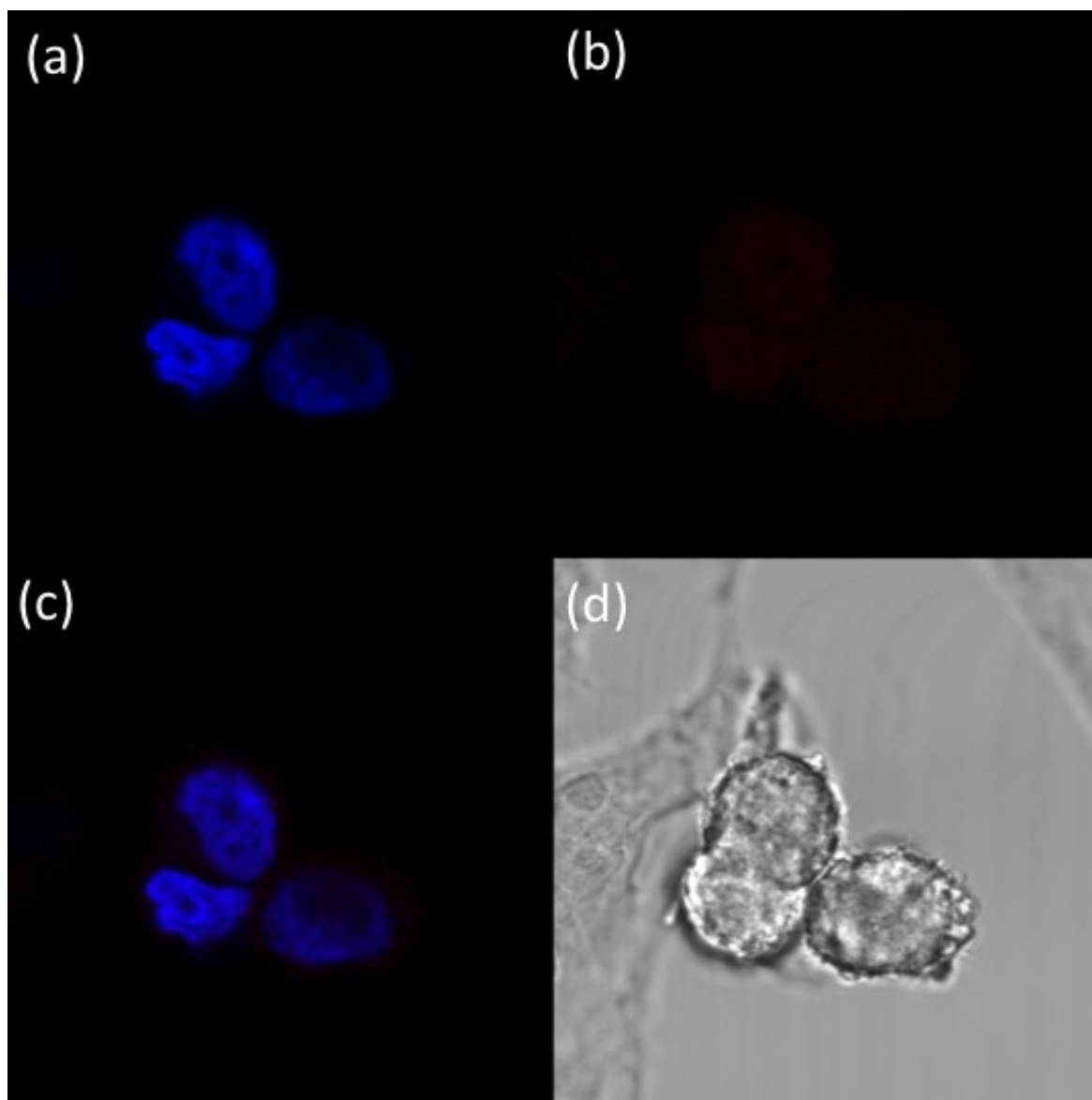
Figure 5.12. Confocal microscopy images of MeWo cells stained by DAPI dyes after adding MMPSense 680 (a) dapi, (b) MMPSense 680 probe, and (c) merged images of DAPI with MMP680Sense probe, (d) dark field image of MeWo. Note that the excitation/ emission were 638 nm/643-717 nm.
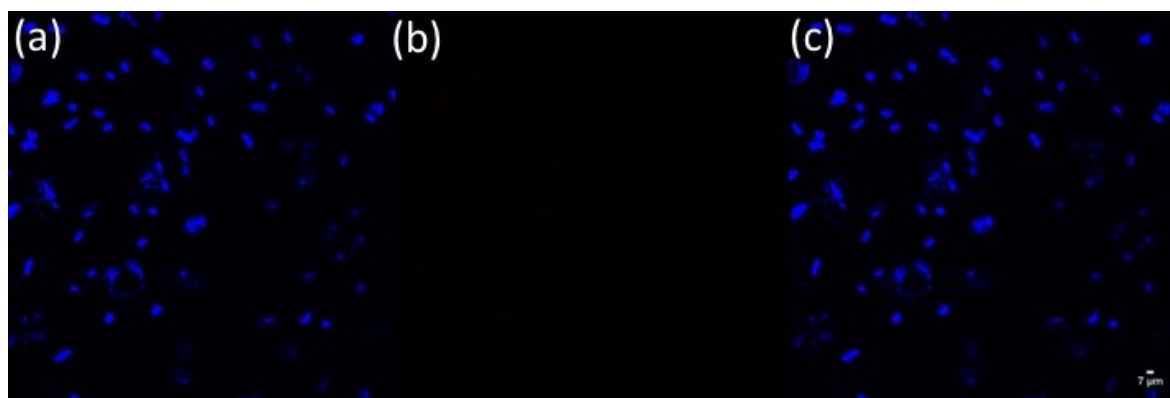
Figure 5.13. Confocal microscopy images of skmel28 cells stained by DAPI dyes for control group (a) dapi, (b) MMPSense 680 probe, and (c) merged images of DAPI with MMP680Sense probe. Note that the excitation/ emission were 638 nm/643-717 nm.
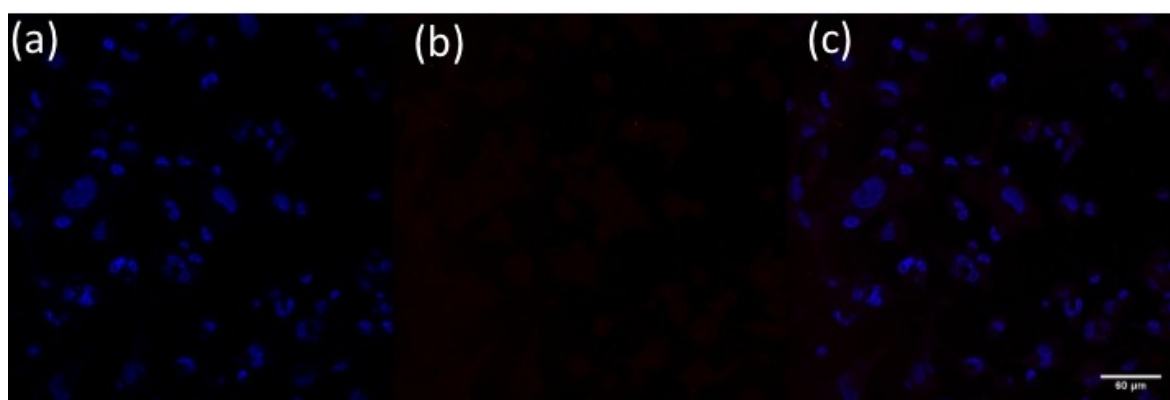
Figure 5.14. Confocal microscopy images of skmel28 cells stained by DAPI dyes after adding MMPSense 680 probe (a) dapi, (b) MMPSense 680 probe, and (c) merged images of DAPI with MMP680Sense probe. Note that the excitation/ emission were 638 nm/643-717 nm.
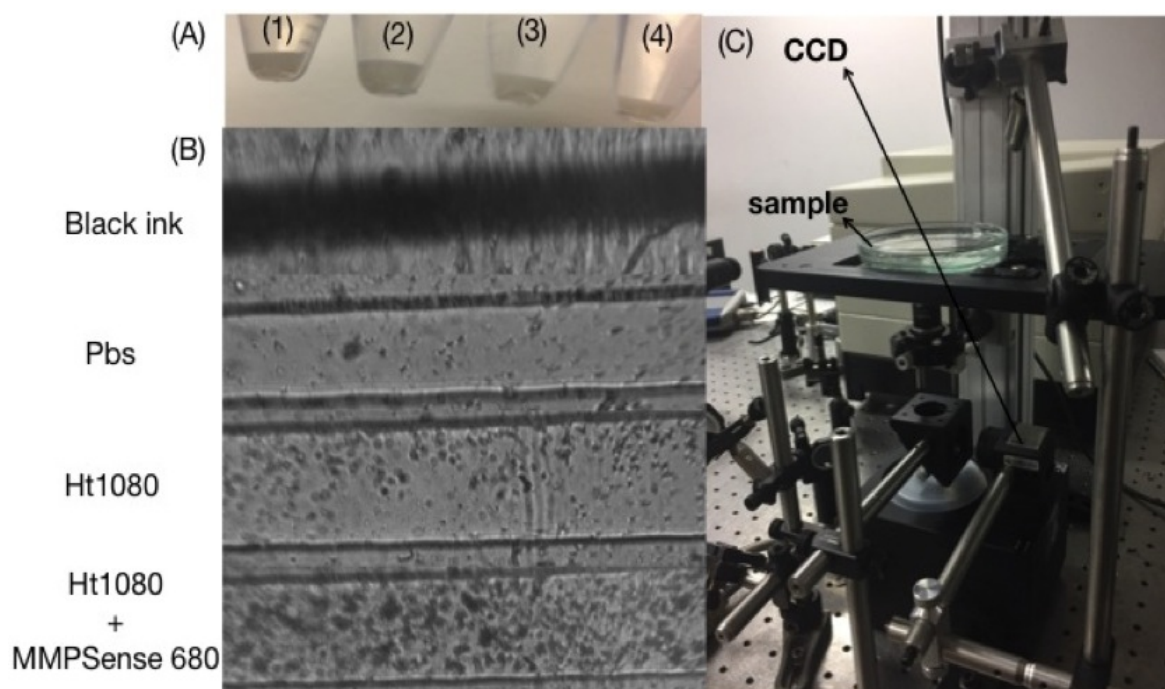
Figure 5.15. (A) Images of (1) Ht1080, (2)Skmel28 (3)MeWo (4) Thp-1 pellets, (B) CCD images of microfludic devices loading black ink, Pbs, Ht1080, and the activated Ht1080 with MMPSense680 probe, (C) the photoacoustic set up provided optical view via CCD.

5.17a obtained from optic microscopy was closely matched with the image (5.17b) scanned by acoustic microscopy with 320 MHz transducers. We also used confocal microscopy to evaluate control and activated group by the probe, and then obtained images from both of them by using acoustic microscopy. While two specific range of acoustic impedance was observed in the control groups, three particular range of acoustic impedance were observed. The activated cells with the decreased impedance were appeared, in the treated cells, as can be seen in Figure 5.18. Moreover, the standard deviation for the control group extracting from both confocal and acoustic microscopy was calculated low than the activated group (Figure 5.19). The results show that the level of MMPs in cancer cell lines may determine by the value of acoustic impedance.
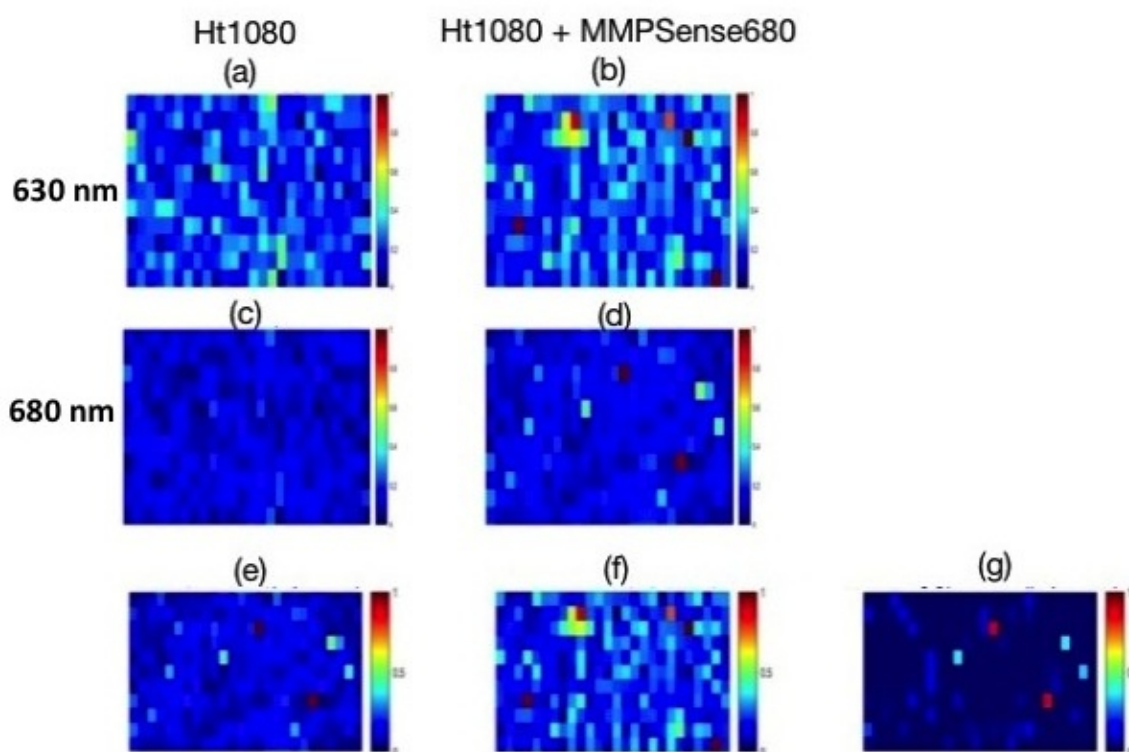
Figure 5.16. Photoacoustic imaging of the MMPSense680 probe accumulation in cells loading in a microfluidic device. The image of cells in the absence of the probe at (a) 680 nm,(c) 630 nm; The image of cells in the presence of the probe at (d),(e) 680 nm; (b),(f) 630 nm ; (g) Subtraction of the images taken at 680 nm and 730 nm resulted in an image with distinct signal coming from the cells incubated with the cleaved probe (PAM images acquired over a scan area of 500 μm x 200 μm with a 20 μm step size).
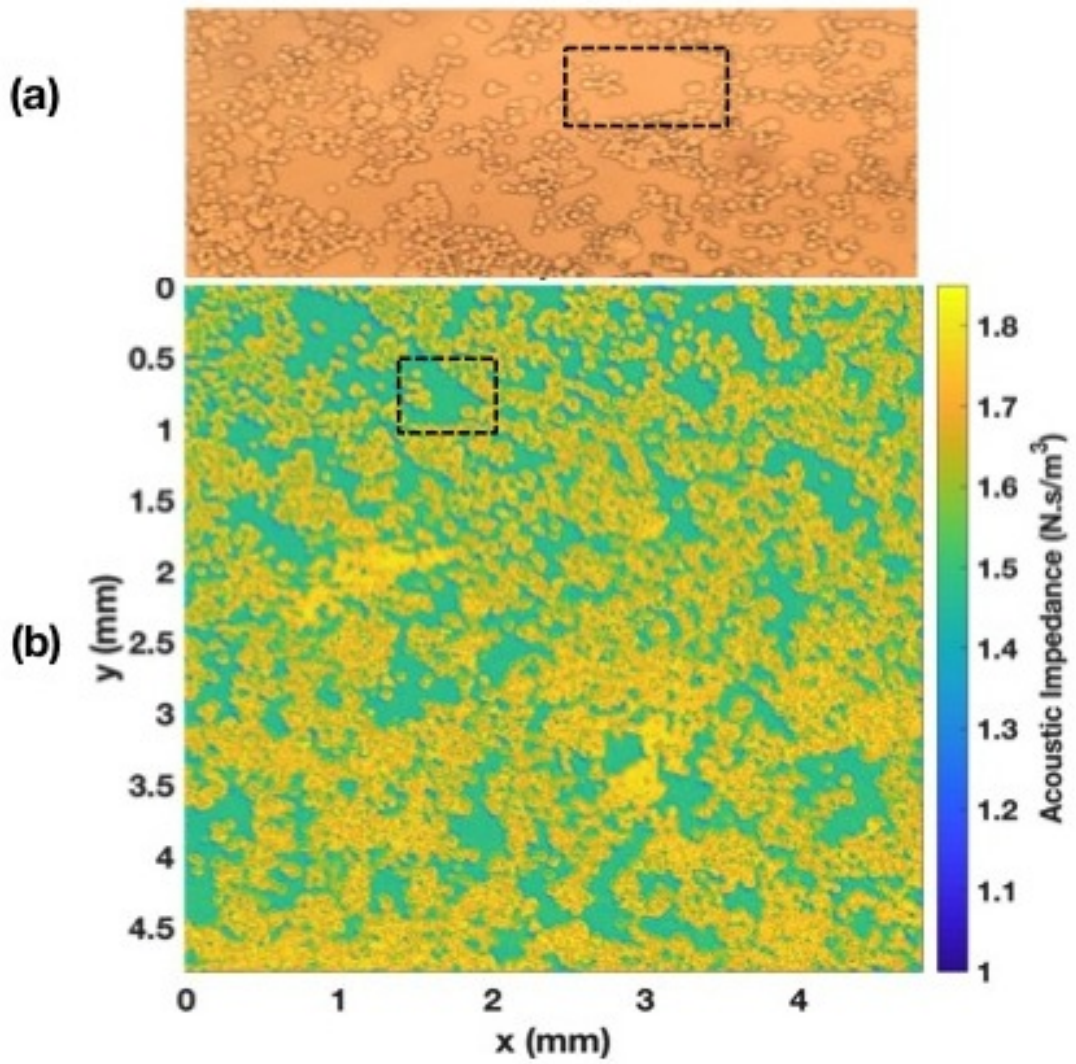
Figure 5.17. (a) Optic (b) acoustic image of the cells. Here, the similarities were depicted by the marked area.
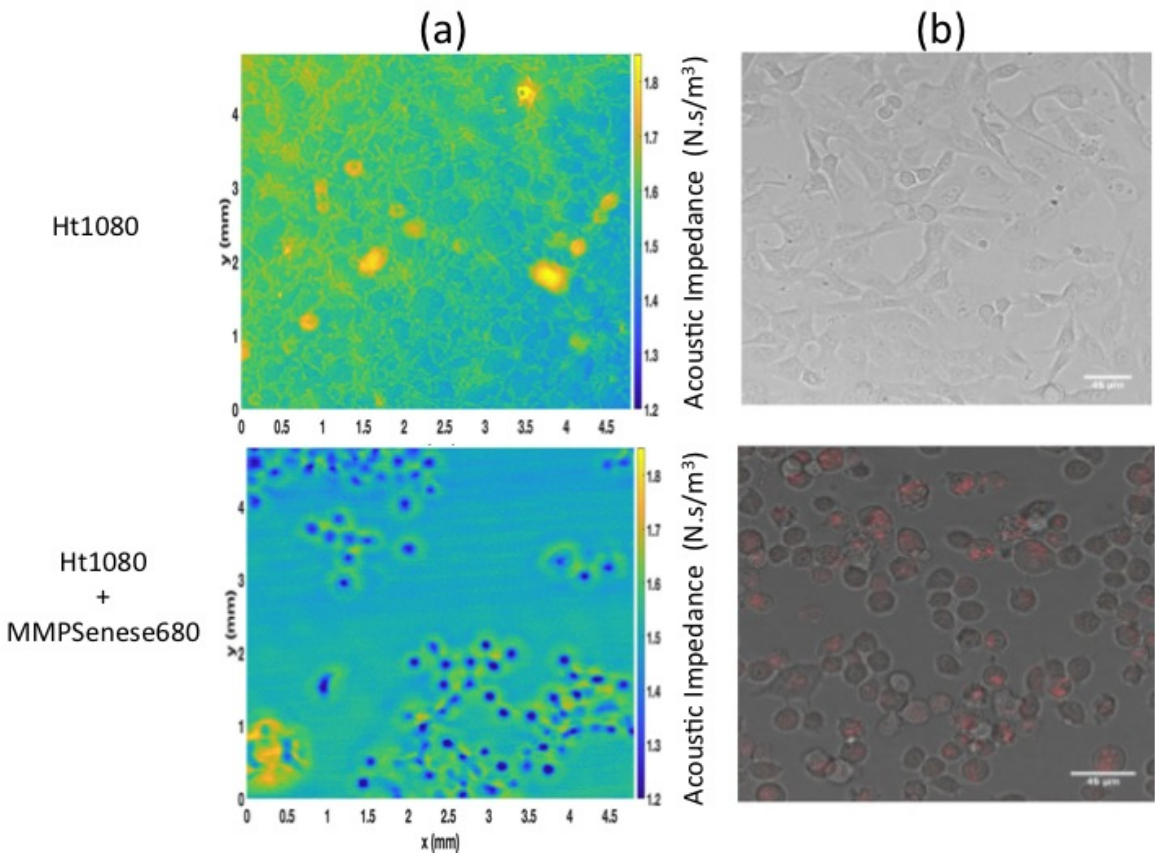
Figure 5.18. (a) The acoustic (b) confocal image of Ht1080 cells activated by probe, (c)the acoustic and (d) confocal image of the control goup.
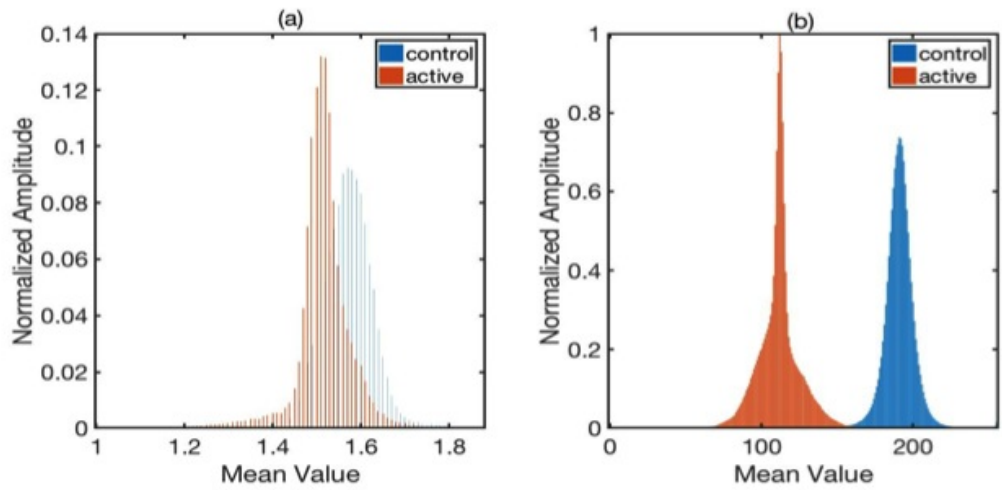
Acoustic M.	Area	Mean	StdDev	Confocal M.	Area	Mean	StdDev
Control	90000	1.572	0.055	Control	1048576	190.995	9.771
Active	90000	1.516	0.066	Active	1058576	111.666	12.259

Figure 5.19. The histogram extracting from (a) acoustic images (Figure 5.18a-c) (b) confocal images (Figure 5.18b-d) including both the activated and the control cells.

6. PHOTOACOUSTIC SIGNAL ENHANCEMENT WITH CONTROLLABLE GENERATION AND MANIPULATION OF MICRO-BUBBLES

6.1. Bubble Dynamics

The Rayleigh- Plesset and the Keller equations are used for describing motions of a spherically symmetric single bubble. Rayleigh analyzed the oscillations of large bubbles such that the surrounding liquid is incompressible and inviscid; thus the bubble remains spherical, surface tension is trivialized. The equation was modified according to effects of viscosity, surface tension, and an incident sound wave by Piesset, Noltingk and Neppiras, and Poritsky. After that, Keller modified the equation to include the effects of acoustic radiation by treating the surrounding compressible liquid [241].

6.2. The Change of Bubble Size as a Function of Time at Different Laser Power for Different Liquids

Our experiment shows the bubble could be successfully generated on the black marker line due to the temperature increase induced by the CW laser irradiation. In this work, the glass slide with a black line is submerged in a petri dish filled with liquid in an the open environment at the room temperature. The laser source is a high power laser diode (wavelength 1064 nm) with a continuously adjustable power up to 1.25 W before the 100X objective lens. The experiments considering the bubble's dynamic behavior were performed with both a custom-built and a commercial (ZEISS PALM MicroTweezers) optical tweezers systems. Both systems enable very similar findings with different working performance. The experiment was repeated for various laser powers, from low to high, until a micro-bubble appeared, in order to estimate the temperature threshold of the micro-bubble formation.
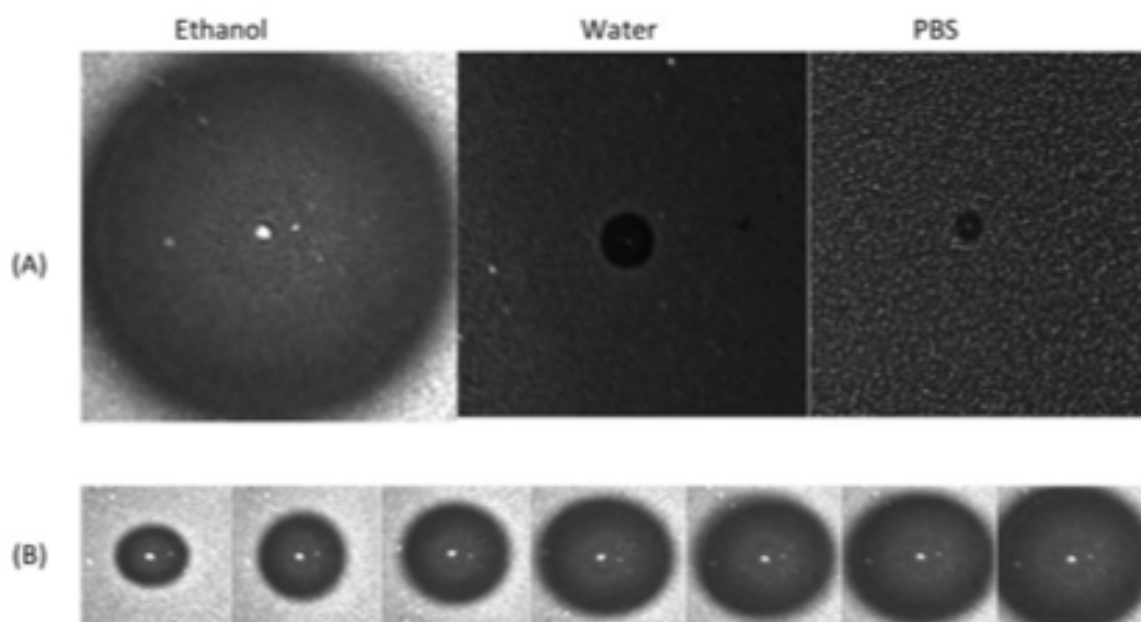
Figure 6.1. (A) The bubbles generated on the on the black marker line with dimension of 1 mm in diameter, in the different liquids including water, ethanol, and PBS, respectively. (B) The growing process of bubble generated in the ethanol.

A bubble growing process in the aqueous fluid is shown in Figure 6.1. When the laser is turned on, the bubble starts to form in the center of the black marker line, grows gradually as the time passes by (t=10s) as shown Figure 6.1A, and finally saturates and maintains a stable state after a period of growing time as shown in Figure 6.1B. Moreover, the bubble tends to rise to the water level under the irradiation of laser. However, if the laser is turned off at any time after the bubble appeared, the bubble maintains stable state for a long period of time, particularly including water or flushed away in the ethanol as shown Figure 6.3. One key factor for bubble formation is the laser power, which is directly associated with the start-up time and the growing velocity of the bubble. Figures 6.3-6.4 show that the radius and the growing rates of bubble increase linearly with the increasing laser power.

The growth rates and saturated rates are different for different solutions such as water, ethanol, and phosphate buffered saline (PBS, pH 7.4). As shown in Figure 6.1, the bubble generated in ethanol has the largest growth rate and its saturated size is the biggest among of the three solutions. Here, the power of the laser source is the
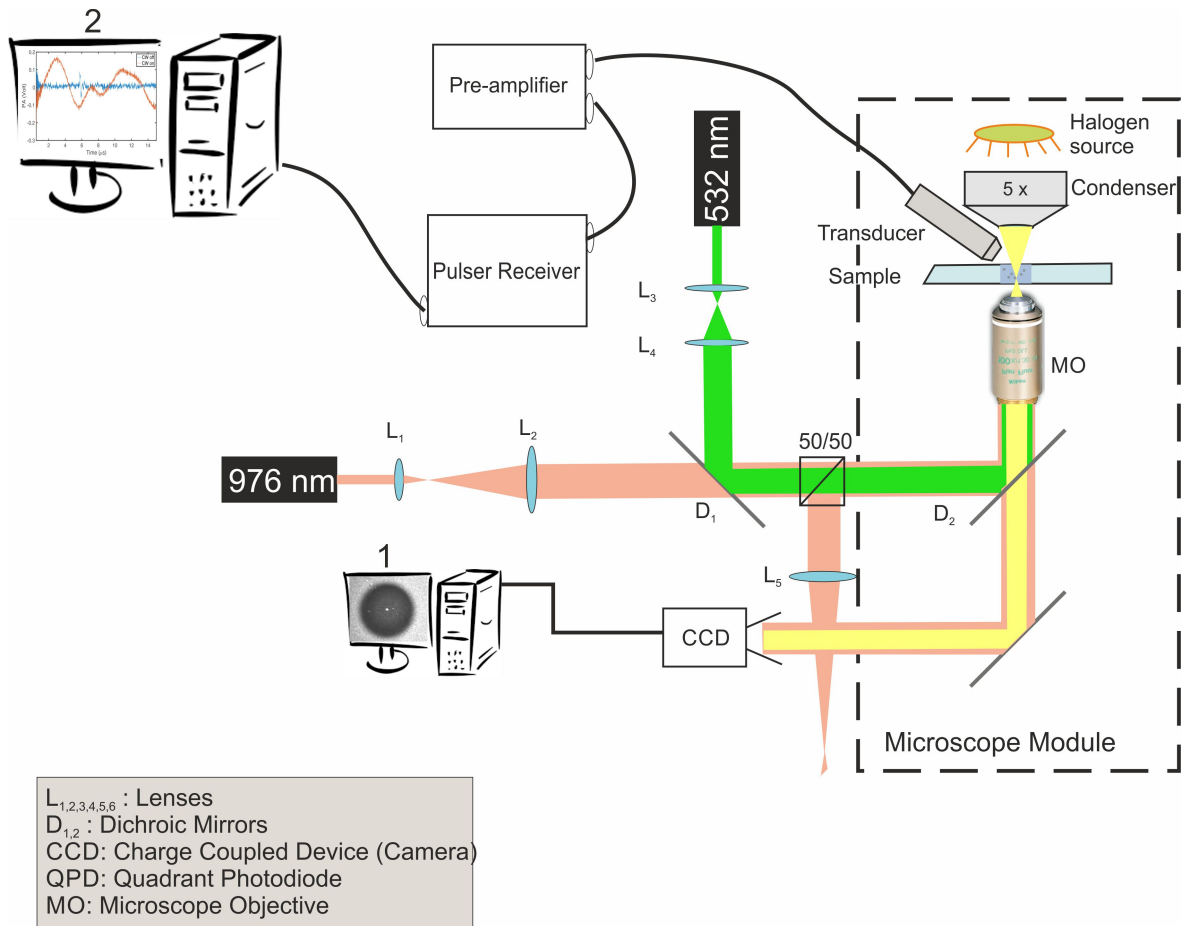
Figure 6.2. (A) The bubbles generated on the black marker line with a dimension of 1 *m*m in diameter, in the different liquids including water, ethanol, and PBS, respectively. (B) The growing process of the bubble generated in the ethanol.

same for these three types of liquids. Moreover, Figure 6.3 illustrates the change of bubble size as a function of time at the same percentage (10 %) of the output power for two mediums (ethanol and water). In the presence of the laser illumination at this power, the occurrence of ethanol heated above its boiling point induces to generate a large bubble as shown in Figures 6.3a and b. The formation of the bubble in the presence of phosphate buffered saline (PBS, pH = 7.4) is slightly different. The bubble starts to form and grows. After a period of start-up time, it shrinks in a while. Then, it saturates and maintains a stable state after the laser is off as shown in Figure 6.4. Thus, the size of the bubble could be adjusted by tuning the working time, the power of the laser source, and types of the fluids. Figures 6.5a-b show the bubble formation and PA signal under CW laser illumination simultaneously, as well as Figures 6.5c-d represent the PA changes under CW laser illumination. Figures 6.5c-d illustrate PA

signal when the CW laser is on and off respectively. Note that the behavior of the PA signal is changed with the emission originating from each bubble. The figure 6.6 illustrates different shape of PA signal under bubble formation, compared between Figures 6.5 and 6.6.
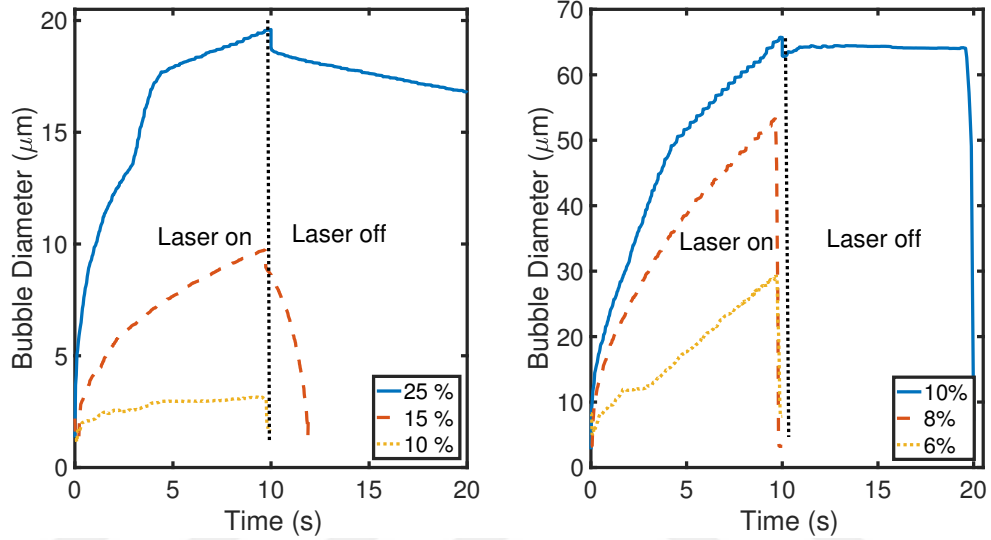
Figure 6.3. The change of bubble size as a function of time at different laser power for different solutions (a) de-ionized water and (b) ethanol.
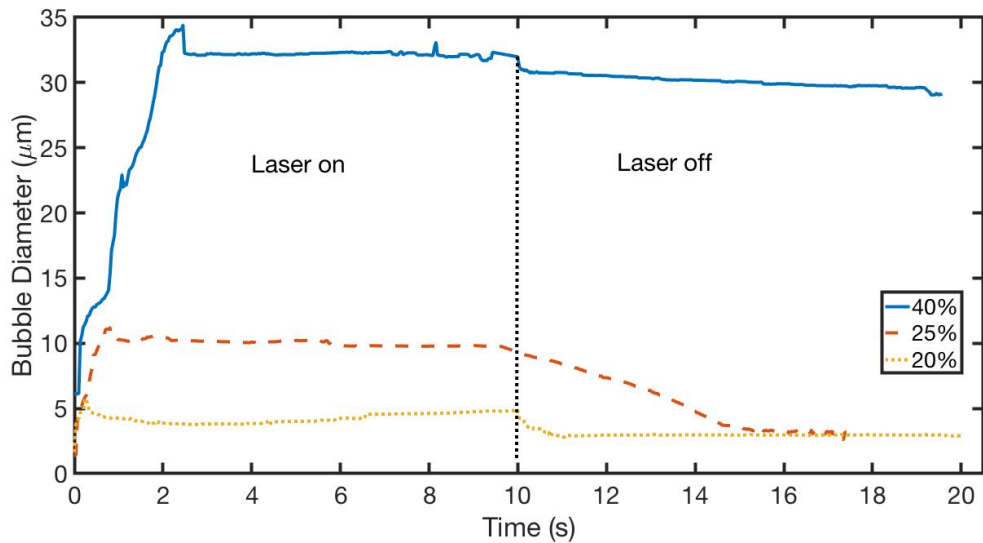
Figure 6.4. The change of bubble size as a function of time at different laser power for phosphate buffered saline (PBS).

In this work, the bubbles are formed within the laser-illuminated region. The generated bubble can easily be moved and transported controlled by the focal spot.
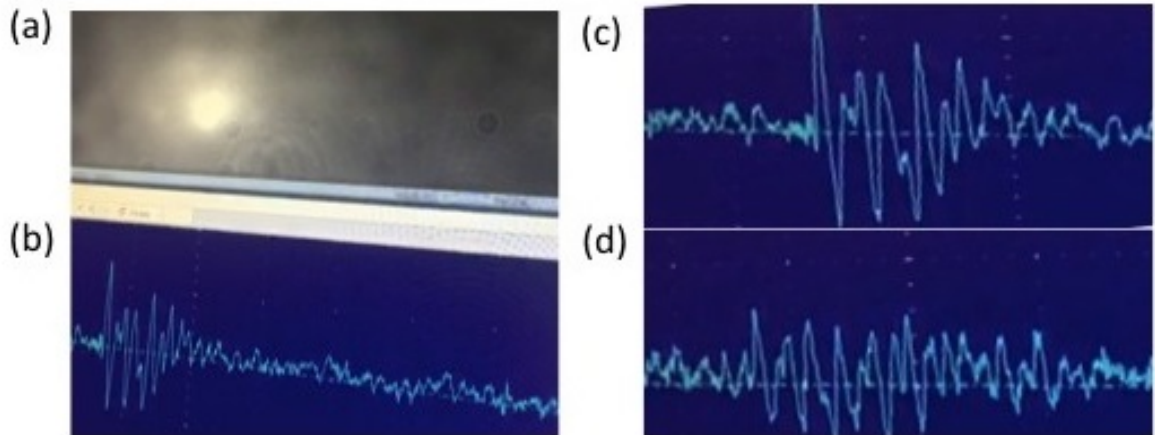
Figure 6.5. (a)-(b) the photograph of the bubble formation and PA signal under CW laser illumination simultaneously, (c)-(d) PA signal when the CW laser is on and off.
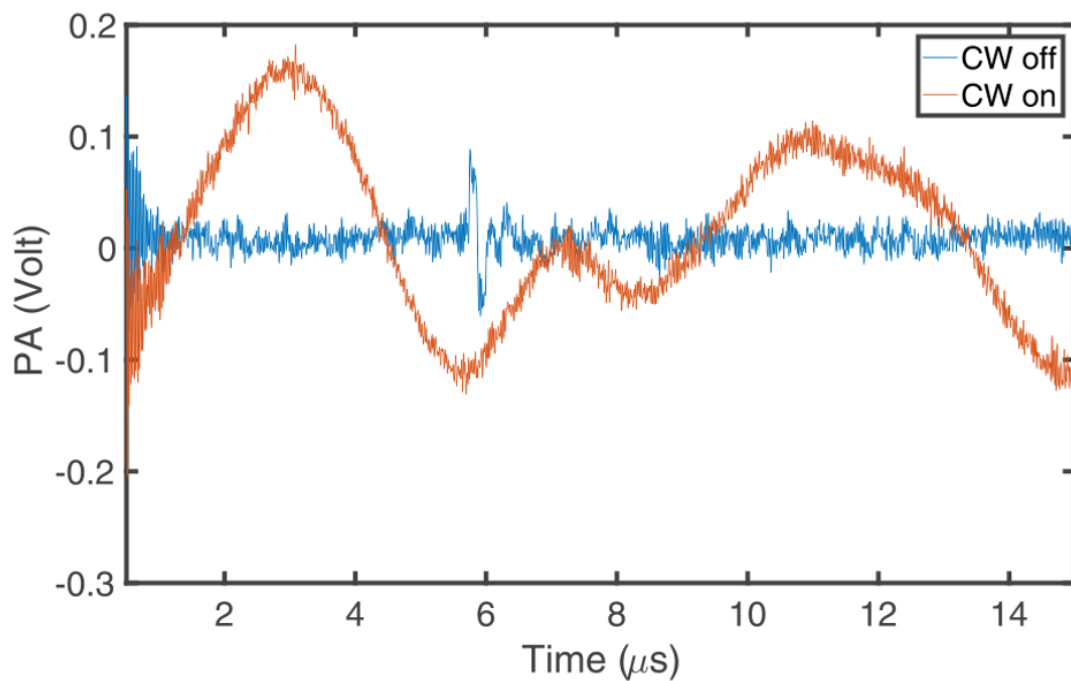
Figure 6.6. Comparision of the PA signal in absence of bubble (bubble line) and the presence of bubble (red line).

The results are extended for applications associated with the precise manipulation, sorting and specific delivery in nano- and micro-engineering problems providing a new method for control of photoacoustic signal generation by using novel fiber laser with adjustable parameters.

6.3. Analytical Modeling for the Influence of Temperature Rise by the Formation of CW Laser-induced Bubbles on Photoacoustic Generation

The propagation of pressure waves in bubble is based on the following wave equation,

$$(\nabla^2 - \frac{1}{c_s^2}\frac{\partial^2}{\partial t^2})p(\mathbf{r}, t) = -\rho n(r)\frac{\partial^2 \beta}{\partial t^2}(r, t) \tag{6.1}$$

where ρ and c are the density and speed of sound of the host liquid, respectively; and β is the local fraction of gas volume given by $\beta = \frac{4}{3}\pi R^3 n$. Here, R describes the instantaneous radius of the bubbles and n is their number per unit volume. Considering a mixture containing bubbles of different size, the number of bubbles per unit volume under equilibrium radius between a and a $+$ da located in the neighborhood of the point x is given by dN=f(a; x)da. Then, the volume fraction is;

$$\beta(\mathbf{x}, t) = \frac{4}{3}\pi \int_0^\infty R^3(a; \mathbf{x}; t)f(a; \mathbf{x})da \tag{6.2}$$

where R (a; x,t) is the radius at time t of a bubble located at position x and it has an equilibrium radius a. During the propagation of the waves, f can be considered constant.

The time derivative of β, given by following equation

$$\frac{\partial \beta}{\partial t} = 4\pi \int_0^\infty R^2 \frac{\partial R}{\partial t} f da. \tag{6.3}$$

Then in the linear approximation, Equation 6.3 can be represented in the form;

$$\frac{\partial \beta}{\partial t} = 4\pi \int_0^\infty a^2 \dot{R} f da \tag{6.4}$$

and

$$\frac{\partial^2 \beta}{\partial^2 t} = 4\pi \int_0^\infty a^2 \ddot{R} f da. \tag{6.5}$$

Based on the numerical simulation and experimental results, we propose the following extended PA equation in the presence of a laser-induced bubble;

$$(\nabla^2 - \frac{1}{c_s^2}\frac{\partial^2}{\partial t^2})p(\mathbf{r}, t) = -\frac{\beta(T)}{c_p}\frac{\partial H}{\partial t}(r, t) - \frac{t_B}{c_p T}\frac{\partial^2 H}{\partial t^2}(r, t) - \rho n(r)\frac{\partial^2 \beta}{\partial t^2}(r, t) \tag{6.6}$$

In case of a monodisperse bubble population with an equal equilibrium radius, f is defined as

$$f = n\delta(a - \bar{a}). \tag{6.7}$$

Substituting Equations 6.7 and 6.5 into Equation 6.6 enable to obtain the extended equation as follows

$$(\nabla^2 - \frac{1}{c_s^2}\frac{\partial^2}{\partial t^2})p(\mathbf{r}, t) = -\frac{\beta(T)}{c_p}\frac{\partial H}{\partial t}(r, t) - \frac{t_B}{c_p T}\frac{\partial^2 H}{\partial t^2}(r, t) - \rho n(r)4\pi\bar{a}^2\ddot{R}. \tag{6.8}$$

Thus, Equation 6.8 can be written in the following form

$$(\nabla^2 - \frac{1}{c_s^2}\frac{\partial^2}{\partial t^2})p(\mathbf{r}, t) = S(r, t) \tag{6.9}$$

where *S(r,t)* is the source term which can be described by

$$S(r, t) = -\frac{\beta(T)}{c_p}\frac{\partial H}{\partial t}(r, t) - \frac{t_B}{c_pT}\frac{\partial^2 H}{\partial t^2}(r, t) - \rho n(r)4\pi\bar{a}^2\ddot{R}. \tag{6.10}$$

Using the Fourier convention, $\{p(\mathbf{r}, t), S(r, t)\} = \frac{1}{\sqrt{2\pi}}\int_{-\infty}^{\infty}\{\widetilde{p}(\mathbf{r}, \omega), \widetilde{S}(\mathbf{r}, \omega)\}\exp(-i\omega t)d\omega$, the wave equation can be expressed in the frequency domain

$$\nabla^2\widetilde{p}(\mathbf{r}, \omega) + \frac{w^2\widetilde{p}(\mathbf{r}, \omega)}{c_s^2} = S(\mathbf{r}, t). \tag{6.11}$$

The solution of Equation 6.8 can be found by utilizing the Green's function approach [60]. The Green's function for Equation 6.11 is given by

$$\widetilde{G}(\mathbf{r}, \mathbf{r}'; \omega) = -\frac{1}{4\pi \mid \mathbf{r} - \mathbf{r}' \mid}\exp(ik_1 \mid \mathbf{r} - \mathbf{r}' \mid) \tag{6.12}$$

where $k_1^2 = \frac{w^2}{c_s^2}$. Here, the temporal and radial parts of the heating function can be expressed by

$$H(\mathbf{r}, t) = A(\mathbf{r})I(t). \tag{6.13}$$

The Gaussian temporal profile can be described by

$$I(t) = \frac{\exp(-t^2/2\tau^2)}{\sqrt{2\pi\tau^2}} \tag{6.14}$$

where τ is the pulse duration of the laser. Moreover, the radial part of the heating function can be written as

$$A(\mathbf{r}) = \frac{p_0(\mathbf{r})c_p}{c_s^2\beta}. \tag{6.15}$$

Substituting Eqs. (6.14) and (6.15) into Eq. (6.13) leads to

$$S_1(\mathbf{r}, t) = \frac{-p_0(\mathbf{r})}{c_s^2} \frac{\partial}{\partial t}\left[\frac{\exp(-t^2/2\tau^2)}{\sqrt{2\pi\tau^2}}\right] = \frac{1}{\sqrt{2\pi}\tau^3}\frac{p_0(\mathbf{r})}{c_s^2}t\exp(-t^2/2\tau^2). \tag{6.16}$$

After applying the Fourier transform to S_1 yields

$$\widetilde{S}_1(\mathbf{r}, \omega) = \frac{1}{\sqrt{2\pi}\tau^3}\frac{p_0(\mathbf{r})}{c_s^2}\int_{-\infty}^{+\infty}t\exp(-t^2/2\tau^2)\exp(iwt)dt = \frac{p_0(\mathbf{r})iw}{c_s^2}\exp(-\tau^2w^2/2). \tag{6.17}$$

Substituting Equations (6.14) and (6.15) into Equation (6.13) leads to

$$\begin{aligned}S_2(\mathbf{r}, t) &= \frac{-t_Bp_0(\mathbf{r})}{\beta c_s^2 T}\frac{\partial^2}{\partial t^2}\left[\frac{\exp(-t^2/2\tau^2)}{\sqrt{2\pi\tau^2}}\right]\\ &= \frac{-t_Bp_0(\mathbf{r})}{\beta c_s^2 T}\left(\frac{t^2 e^{-\frac{t^2}{2\tau^2}}}{\sqrt{2\pi}\,(\tau)^5} - \frac{e^{-\frac{t^2}{2\tau^2}}}{\sqrt{2\pi}\,(\tau)^3}\right).\end{aligned} \tag{6.18}$$

The Fourier transform of $S_2(\mathbf{r},$t$)$

$$S_2(\mathbf{r}, w) = \frac{-t_B p_0(\mathbf{r})}{\beta T c_s^2} \int_{-\infty}^{+\infty} \left(\frac{t^2 e^{-\frac{t^2}{2\tau^2}}}{\sqrt{2\pi} (\tau)^5} - \frac{e^{-\frac{t^2}{2\tau^2}}}{\sqrt{2\pi} (\tau)^3} \right) e^{itw} dt$$
$$= \frac{t_B p_0(\mathbf{r})}{\beta T c_s^2} w^2 \left(\exp(-\frac{\tau^2 w^2}{2}) \right). \tag{6.19}$$

The radius at time t of a bubble located at position x for a third source term in Equation (6.10) can be proposed;

$$R = \text{A1} \cos(tw) + \text{A2} \sin(tw). \tag{6.20}$$

The Equation (6.20) represents the best fitting to experimental data. Then, the third source is written as

$$S_{3a} = -\rho n(r) 4\pi \bar{a}^2 (-\text{A1} w_0^2 \cos(tw_0) - \text{A2} w^2 \sin(tw_0)). \tag{6.21}$$

Morover, R(t) is proposed as follows

$$R_2(t) = A_0 + A_1 cos(w_0 t) + A_2 sin(w_0 t) + A_3 cos(2w_0 t) + A_4 sin(2w_0 t) \tag{6.22}$$

for second fit to experimental data. Substituting Equation 6.22 into the third source leads to

$$S_{3b} = - \rho n(r) 4\pi \bar{a}^2 (-\text{A1} w_0^2 \cos(tw_0) - \text{A2} w_0^2 \sin(tw_0) - 4\text{A3} w_0^2 \cos(2tw_0) \qquad (6.23)$$
$$- 4\text{A4} w_0^2 \sin(2tw_0)).$$

Applying the Fourier transform to S_{3a} yields

$$\widetilde{S_3 a}(\mathbf{r}, \omega) = -\rho n(r) 4\pi \bar{a}^2 \int_{-\infty}^{+\infty} dw \exp(iwt)[-\text{A1} w_0^2 \cos(tw_0) - \text{A2} w_0^2 \sin(tw_0)]. \quad (6.24)$$

The Equation 6.24 can be written in following form,

$$\widetilde{S_3 a}(\mathbf{r}, \omega) = \frac{-\rho n(r) 4\pi \bar{a}^2 w_0^2}{2} \int_{-\infty}^{+\infty} dt \exp(iwt)(-\text{A1}(\exp(itw_0) + \exp(-itw_0))$$
$$- \frac{\text{A2}}{i}(\exp(itw_0) - \exp(-itw_0)). \qquad (6.25)$$

Using the definition of the Dirac delta function given by Equation 6.26,

$$\int_{-\infty}^{+\infty} \exp(-i(w - w_0)t) dt = 2p\delta(w - w_0). \qquad (6.26)$$

The third source is given by

$$\widetilde{S_3a}(\mathbf{r}, \omega) = \frac{-\rho n(r)4\pi\bar{a}^2 w_0^2}{2}\left[(-\text{A1} - \frac{\text{A2}}{i})\delta(-w_0 - w) + (-\text{A1} + \frac{\text{A2}}{i})\delta(w_0 - w)\right].$$

$$(6.27)$$

6.3.1. Solution of the Modified Photoacoustic Wave Equation for a Gaussian Radial Absorption Profile

In this section, we describe the radial profile by a Gaussian function with the standard deviation or beamwidth of the laser σ

$$p_0(\mathbf{r}) = \exp\left(-\frac{r^2}{2\sigma^2}\right)\theta(r)\theta(-r + R) \qquad (6.28)$$

where θ is the Heaviside step function. The following integral can be written as a summation of three terms corresponding to three different sources as follows

$$\widetilde{p}(\mathbf{r}, \omega) = \int \widetilde{G}(\mathbf{r}, \mathbf{r}'; \omega)\widetilde{S}(\mathbf{r}', \omega)d^3r' \qquad (6.29)$$

where $S = S_1 + S_2 + S_3$. The contribution coming from the first source is

$$\widetilde{p_1}(\mathbf{r}, \omega) = -\frac{ip_0}{4\pi}\frac{\omega}{c_s^2}\exp(\frac{-\tau^2 w^2}{2})\int_0^{2\pi} d\phi \int_0^R (r')^2 dr' \int_{-1}^{+1}\frac{\exp(ik_1 \mid \mathbf{r} - \mathbf{r}' \mid)}{\mid \mathbf{r} - \mathbf{r}' \mid}d\mu' \quad (6.30)$$

where $\mid \mathbf{r} - \mathbf{r}' \mid = \sqrt{r^2 - r'^2 - 2rr'\mu'}$, $\mu' = \cos\theta'$, and

$$\int_{-1}^{+1}\frac{\exp[(ik_1)\sqrt{(r^2 - r'^2 - 2rr'\mu')}]}{\sqrt{(r^2 - r'^2 - 2rr'\mu')}}d\mu' = -\frac{1}{irr'k_1}[\exp[ik_1(r - r')] - \exp[ik_1(r + r')]].$$

So the solution due to the first source becomes

$$p_1(r,t) = \frac{p_0}{2\sqrt{2\pi}} \frac{1}{rc_s^2} \int_0^R dr'r' \exp(-\frac{r'^2}{2\sigma^2})$$
$$\times \int_{-\infty}^{-\infty} \exp[-\frac{\tau^2 w^2}{2} + ik_1(r \pm r') - i\omega t]d\omega, \qquad (6.31)$$

and the solution due to the second source becomes

$$p_2(r,t) = \frac{p_0}{2\sqrt{2\pi}} \frac{t_\beta}{r\beta c_s T} \int_0^R r' \exp(-\frac{r'^2}{2\sigma^2})$$
$$\times \int_{-\infty}^{-\infty} \exp[-\frac{\tau^2 w^2}{2} + ik_1(r \pm r') - i\omega t]wd\omega dr'. \qquad (6.32)$$

The equation 6.32 is written in the following form

$$p_2(r,t) = \left[\frac{p_0}{2\sqrt{2\pi}} \frac{t_\beta}{r\beta c_s T}\right](J_{2a} - J_{2b}) \qquad (6.33)$$

where

$$J_{2a} = \int_0^R dr'r' \exp(-\frac{r'^2}{2\sigma^2})\left[-\frac{i\sqrt{2\pi}\,(-r + tVs + r')\,e^{-\frac{(-r+Vst+r')^2}{2\sigma^3 Vs^2}}}{\sigma^3 Vs}\right] \qquad (6.34)$$

and

$$J_{2b} = \int_0^R dr'r' \exp(-\frac{r'^2}{2\sigma^2})\left[\frac{i\sqrt{2\pi}\,(r - tVs + r')\,e^{-\frac{(r-Vst+r')^2}{2Vs^2}}}{\sigma^3 Vs}\right]. \qquad (6.35)$$

By evaluating the integral in Equation 6.34, we obtain

$$
\begin{aligned}
J2a = & -\frac{i\sqrt{2\pi}}{\left(\tau^2\right)^{3/2}\mathrm{Vs}}\left(\frac{\sigma^2 b^2 \mathrm{Vs}^2 e^{-\frac{(t\mathrm{Vs}-r)^2}{2\tau^2\mathrm{Vs}^2}}}{2\left(\sigma^2+\tau^2\mathrm{Vs}^2\right)^{5/2}}\right. \\
& \times \left(\sqrt{2\pi}ab\mathrm{Vs}\left(\sigma^2+\mathrm{Vs}^2\left(\tau^2-t^2\right)-r^2+2rt\mathrm{Vs}\right)\right. \\
& \mathrm{erf}\left(\frac{\sigma(r-t\mathrm{Vs})}{\sqrt{2}\tau\mathrm{Vs}\sqrt{\sigma^2+\tau^2\mathrm{Vs}^2}}\right)\exp\left(\frac{\sigma^2(t\mathrm{Vs}-r)^2}{2\tau^2\mathrm{Vs}^2\left(\sigma^2+\tau^2\mathrm{Vs}^2\right)}\right) \\
& \left.+2\tau^2\mathrm{Vs}^2\sqrt{\sigma^2+\tau^2\mathrm{Vs}^2}(t\mathrm{Vs}-r)\right)-\frac{\sigma^2\tau^2\mathrm{Vs}^2\exp\left(-\frac{R^2}{2\sigma^2}-\frac{(-r+R+t\mathrm{Vs})^2}{2\tau^2\mathrm{Vs}^2}\right)}{2\left(\sigma^2+\tau^2\mathrm{Vs}^2\right)^{5/2}} \\
& \times \left(\sqrt{2\pi}\sigma\tau\mathrm{Vs}\left(\sigma^2+\mathrm{Vs}^2\left(\tau^2-t^2\right)-r^2+2rt\mathrm{Vs}\right)\mathrm{erf}\left(\frac{\sigma^2(r-R-t\mathrm{Vs})-\tau^2 R\mathrm{Vs}^2}{\sqrt{2}\sigma\tau\mathrm{Vs}\sqrt{\sigma^2+\tau^2\mathrm{Vs}^2}}\right)\right. \\
& \times \exp\left(\frac{\left(\sigma^2(-r+R+t\mathrm{Vs})+\tau^2 R\mathrm{Vs}^2\right)^2}{2\sigma^2\tau^2\mathrm{Vs}^2\left(\sigma^2+\tau^2\mathrm{Vs}^2\right)}\right) \\
& \left.\left.\left.+2\sqrt{\sigma^2+\tau^2\mathrm{Vs}^2}\left(\sigma^2 R+\tau^2\mathrm{Vs}^2(-r+R+t\mathrm{Vs})\right)\right)\right)\right).
\end{aligned}
\tag{6.36}
$$

We note that the calculation of the integral J_{2b} is very similar to the one of the integral J2b. These integrals contribute significantly to the PA signal.

The solution due to the third source becomes

$$
\begin{aligned}
p_{3a}(r,t) = & \frac{-\rho n(r)4\pi\bar{a}^2 c_s\omega_0}{2ir}\int_0^R r'\left(-A_1-\frac{1}{i}\right)\frac{\delta(-\omega_0-\omega)}{\omega}\exp[ik_1(r\pm r')-i\omega t] \\
& -\left(A_1-\frac{A_2}{i}\right)\frac{\delta(\omega_0-\omega)}{\omega}\exp[ik_1(r\pm r')-i\omega t]\Bigg)d\omega dr'.
\end{aligned}
\tag{6.37}
$$

We can rewrite Equation 6.37 in the following form which yields the pressure wave emitting from bubble,

$$p_{3a}(r,t) = \frac{-\rho n(r)4\pi\bar{a}^2 c_s w_0}{2ir}(J_{3a}(r,t) + J_{3b}(r,t)) \tag{6.38}$$

where

$$J_{3a}(r,t) = \frac{-\rho n(r)4\pi\bar{a}^2 c_s w_0}{2ir}\int_0^R r'\left(A_1 + \frac{A2}{i}\right)\exp[ik_1(r \pm r') + i\omega t]dr' \tag{6.39}$$

and

$$J_{3b}(r,t) = \frac{-\rho n(r)4\pi\bar{a}^2 c_s w_0}{2ir}\int_0^R r'\left(-A_1 + \frac{A2}{i}\right)\exp[ik_1(r \pm r') - i\omega t]dr'. \tag{6.40}$$

By evaluating the integral in Equations 6.39 and 6.39, we obtain

$$p_3 a(r,t) = 8i\pi a^2 \mathrm{Vs}^2 e^{\frac{ir\omega_0}{\mathrm{Vs}}}(A2\cos(t\omega_0) - A1\sin(t\omega_0))$$
$$\times \frac{R\omega_0\cos\left(\frac{R\omega_0}{\mathrm{Vs}}\right) - \mathrm{Vs}\sin\left(\frac{R\omega_0}{\mathrm{Vs}}\right)}{r\omega_0}. \tag{6.41}$$

6.4. Numerical Results and Discussion

We inferred the parameters from our mathematical model with experimentally determined values. Figure 6.3-6.4 represents the temporal profile of bubble motion. We extracted this profile by using our custom software written in MATLAB which imports video files that have already been saved during experiments. The videos were captured

Table 6.1. Constitutive parameters for the two various bubble having different resonance frequences.

Parameters (P)	Simulation P. I	Simulation P. II
A1 (m)	10	10
A2 (m)	10	10
R (μ m)	10	50
ω (MHz)	0.4	5
$\sigma(\mu$ m)	10	10
τ (ns)	5	5
r (mm)	2	2

by the camera which provides the record at 24 frames per second. The software allows for a user to a threshold, crop images and select the region of interest (ROI) and frames to be processed. The image processing toolbox is used to detect the bubble in every frame. Measuring the detected diameter of the bubble in every frame and plotting it versus time, we obtained the dynamics of the microbubbles. Although the characterization and amplitude of PA signal change in the presence of bubble forming under CW laser and the bubble triggered by pulse laser, the fitted experimental data does not correlate with our experiment values since the performance of the camera used in our experiment does not produce an adequate frame rate for observing behavior of bubble at the time scale of the occurrence of photoacoustic signal. However, if the simulation parameters from the literature are used, the mathematical model yields consistent results. The parameters in Table 6.1 took from the literature. The Figure 6.7 illustrates the PA signal generated from an absorber like RBC, and Figure 6.8 represents the nonlinear PA signal due to a temperature increase in the case bubble formation. Figures 6.9 and 6.10 represent the characterization and enhancement of the PA signal in the case of the bubbles in terms of their resonance frequency.
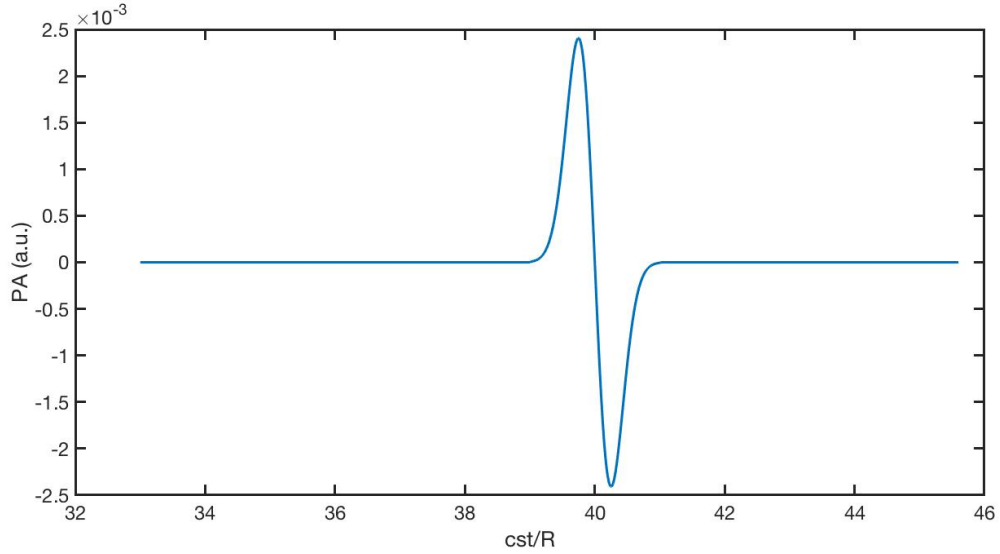
Figure 6.7. Normalized PA wave p(r,t)/p0 generated by first source vs normalized time cst/R, an ultrasonic detector located at position r=2 mm, σ=10 μm, τ=5 ns.
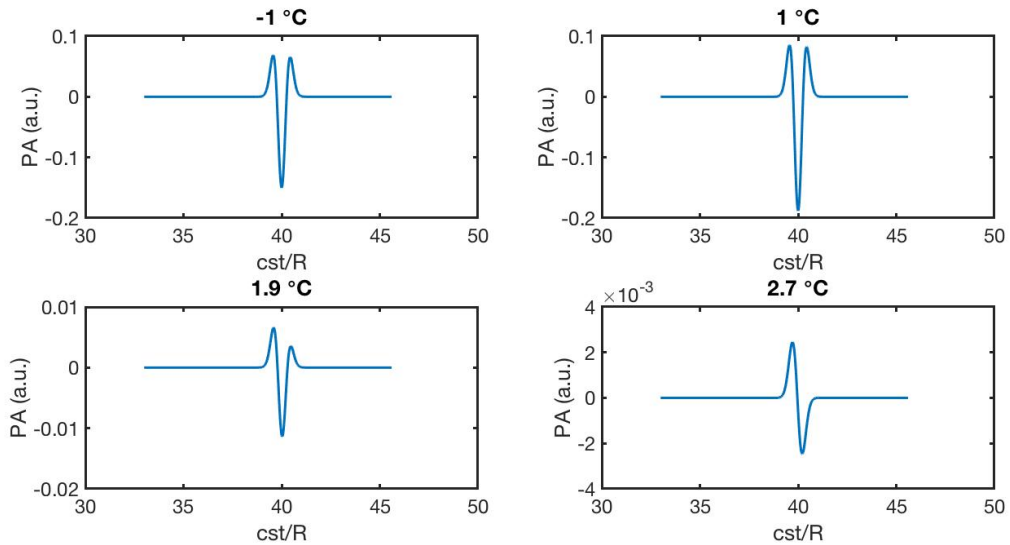
Figure 6.8. Normalized PA wave p(r,t)/p0 on the temperature dependence of the generated pressure amplitudes regarding the contribution of second source vs normalized time cst/R, an ultrasonic detector located at position r=2 mm, σ=10 μm, τ=5 ns.
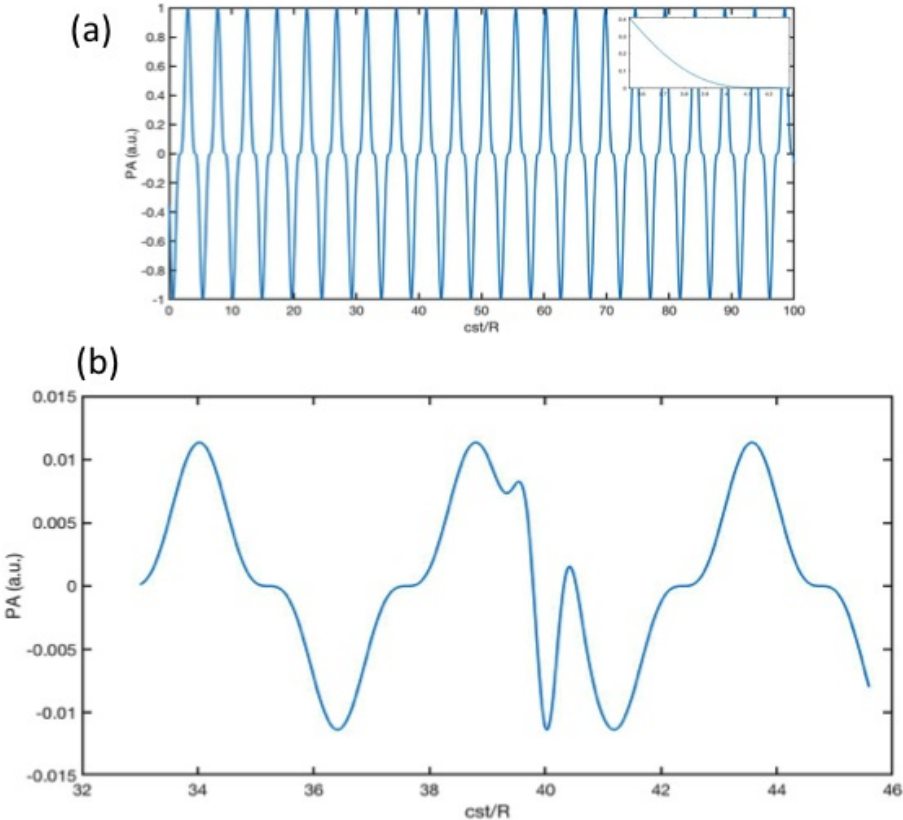
Figure 6.9. (a)The pressure emitting from the bubble with 0.4 MHz vs time scale of photoacoustic wave, (b) The photoacoustic wave resulting from the first and second contribution, an ultrasonic detector located at position r=2 mm.
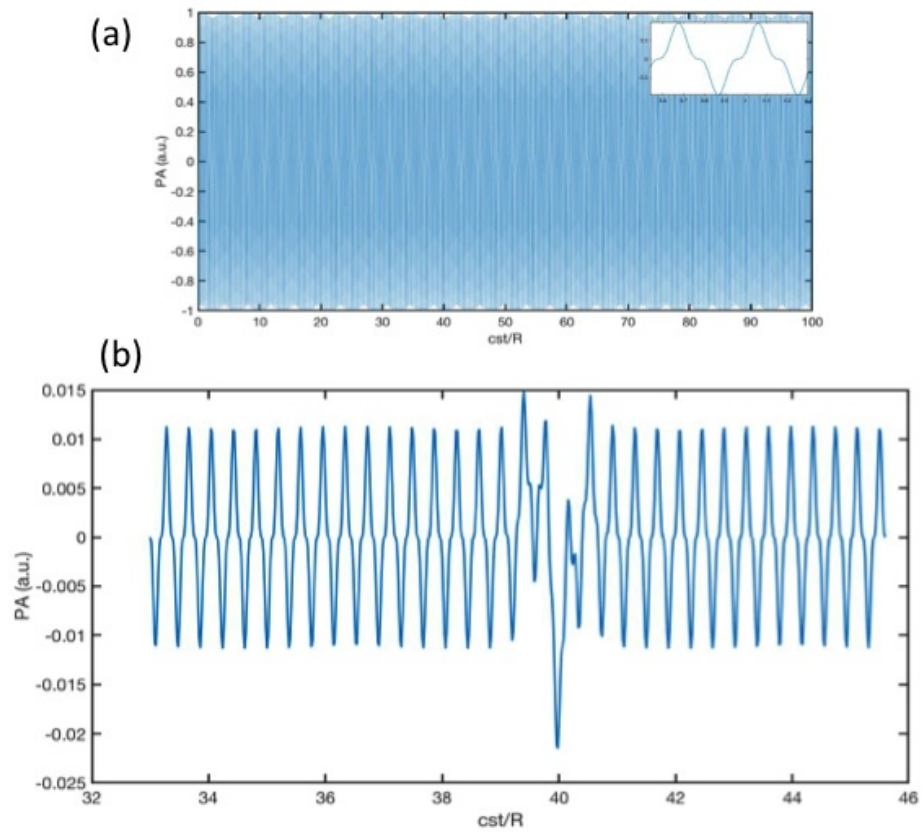
Figure 6.10. The pressure emitting from the bubble with 5 MHz vs time scale of photoacoustic wave, (b) The photoacoustic wave resulting from the first and second contribution, an ultrasonic detector located at position r=2 mm.

7. CONCLUSION

We developed a laser system which produces the wavelength tunability with a repetition rate up to 1 MHz. This system is all-fiber integrity and has higher PRF via custom developed FPGA electronics controlling laser diode. We reported that all the laser parameters are controlled by adjusting FPGA configuration and currents to the pump diodes electronically in the absence of any mechanical intervention. Moreover, the novel laser is very compact with dimensions of 40x40x9 cm3 regardless of the free-space harmonic generation unit. For example, comparing OPO laser, the big cooling unit is not necessary. The wavelength tunable fiber lasers with PRF gives an opportunity to implement photoacoustic applications by providing a fast image. In our system, the light is transmitted through the splice between Yb-doped fiber and PCF for rendering all-fiber integrity with an efficiency of 40 % One of the disadvantages of current configuration is the heating at the splice point. Despite the cooling fan, the splice should be renewed once in a while in order to compensate for decreasing power in time. In order to handle the issue for robust and long-term operation, the splicing between the gain fiber and the PCF is optimized for low-loss and high tensile strength (using GPX-3000 series splicer, Vytran, Inc.), as demonstrated in the context of in-situ absorption spectroscopy of plasmas using a similar supercontinuum source and the same type of fibre [242]. Free space coupling is also possible between Yb-doped fiber and PCF; in that case transmission can be performed with higher efficiency and higher pulse energies can be produced if all-fiber integrity is disregarded. The present limitations to the continuously and independently adjustable laser parameters arise from the requirement of simultaneous satisfaction of the following conditions during laser design: ensuring that each amplification stage is seeded with sufficient power to prevent generation of laser noise in the form of amplified spontaneous emission (ASE), ensuring that the targeted, final pulse duration will depend on the seed pulse duration in a complex manner due to gain saturation and that there is sufficient peak power to accomplish the supercontinuum generation in the PCF. We believe that even a large range of parameters are possible, albeit at the cost of increased system complexity (by adding a second AOM and additional amplifier stages). The present parameter range

was decided based on the balance between system complexity and sufficiency for most typical OR-PAM applications.

With the analyses of the extended photoacoustic transport model for characterization of red blood cells morphology in microchannel flow, our theoretical study and simulation results allow a direct investigation of how cell deformability and laser parameters affect the photoacoustic waveform. Our detailed study shows how the model could potentially reveal the process of cell aggregation. We presented the model coupling photoacoustic (PA) and the Navier-Stokes equations. The generalized wave equation includes the effects of viscosity and aggregation of cells on PA emission. Moreover, we measured the interaction force between RBCs of various patients by optical tweezer. The study of PA signal from the mathematical modeling to the experimental design and detection in micro-channels can be beneficial for therapeutic applications. The distinctive features of the photoacoustic waves enable to understand diseased or damaged RBCs having abnormal shapes and sizes, which can result from a variety of diseases. This work can be helpful to improve a hybrid simulation approach for not only the characterization of red blood cell morphology but also for cancer cell lines in the microchannel flow. To describe and analyze the mechanical processes inside a microfluidic device, our hybrid model can pave the way toward the development of new physical models in the rapidly advancing field of lab-on-chip technology and photoacoustics.

The presence of MMPs enzyme which involves in tumor growth, invasion, and metastasis, is detected with PAM by means of activation-dependent absorption changes. For this study, a novel thin PDMS having various channel widths and depths to mimic tissue or organ level physiology, vessels were created and it helps to evaluate two photoacoustic smart probes. The image of smart probe accumulation in vitro by using the microfluidic platforms in the field of photoacoustic is the first study in the literature. The study provides the investigation of the efficiency in the development of new photoacoustic contrast agents, as well as new drug candidates, and monitor treatment response in vitro before conducting animal experiments. Moreover, it is possible to quantitatively analyze the visualization of MMP activity by using acoustic microscopy

with the help of confocal microscopy. Apart from these results, it is also possible to determine the level of MMP enzyme in different cancer cell lines by using both the intracellular acoustic impedance of the cells and the activatable Photoacoustic image by using multiwavelength wavelength imaging was planned as a future work.

We proposed that the bubble generation behavior by continuous wave (CW) laser radiation is suitable than the bubble formation under the pulsed laser irradiation in the field of photoacoustics. We conduct an experimental study on the formation mechanisms and dynamics of microbubble under CW laser irradiation and characterize an enhanced photoacoustic response with controllable generation and manipulation of microbubbles by using a novel pulsed fiber laser. We propose a new theoretical model including laser parameters such as the beam width, pulse duration, and repetition rate and a bubble dynamics model in order to analyze bubble dynamics created by a focused CW laser beam on photoacoustic waves. This work represents direct observations and theoretical descriptions of the bubble formation around heated particles and the resultant enhanced amplitude of the acoustic signal. Even though the fitted experimental data does not correlate with our experiment values since the performance of the camera used in our experiment does not produce an adequate frame rate for observing behavior of bubble at the time scale of the occurrence of photoacoustic signal. However, if the simulation parameters from the literature are used, the mathematical model yields consistent results. The experimental results will obtained by using high frame rate CCD camera as a future work, and the results will be prepared to be published in a highly prestigious journal. The photoacoustic signal resulting from the assistance of microbubbles induced by irradiating several absorbers with CW laser can be monitored in a real time. This study may advance a quantitative thermal mapping in bubble-assisted thermotherapy and photoacoustic drug delivery implementation.

REFERENCES

1. Fenech, M., D. Garcia, H. J. Meiselman and G. Cloutier, "A particle dynamic model of red blood cell aggregation kinetics", *Ann. Biomed. Eng*, Vol. 37, No. 11, pp. 2299–2309, 2009.

2. Yazdani, A., H. Li, J. D. Humphrey and G. E. Karniadakis, "A General Shear-Dependent Model for Thrombus Formation", *PLOS Comput. Biol.*, Vol. 13, No. 1, p. e1005291, 2017.

3. Steffen, P., C. Verdier and C. Wagner, "Quantification of depletion-induced adhesion of red blood cells", *Physical Review letters*, Vol. 110, No. 1, p. 018102, 2013.

4. Zhang, J., P. C. Johnson and A. S. Popel, "Effects of erythrocyte deformability and aggregation on the cell free layer and apparent viscosity of microscopic blood flows", *Microvasc. Res.*, Vol. 77, No. 3, pp. 265–272, 2009.

5. Tsai, A. G., B. Y. Salazar Vázquez, P. Cabrales, E. B. Kistler, D. M. Tartakovsky, S. Subramaniam, S. A. Acharya and M. Intaglietta, "Replacing the Transfusion of 1–2 Units of Blood with Plasma Expanders that Increase Oxygen Delivery Capacity: Evidence from Experimental Studies", *Journal of Functional Biomaterials*, Vol. 5, No. 4, pp. 232–245, 2014.

6. Nash, G., "Blood rheology and ischaemia", *Eye*, Vol. 5, No. 2, p. 151, 1991.

7. Brust, M., O. Aouane, M. Thiébaud, D. Flormann, C. Verdier, L. Kaestner, M. Laschke, H. Selmi, A. Benyoussef, T. Podgorski *et al.*, "The plasma protein fibrinogen stabilizes clusters of red blood cells in microcapillary flows", *Scientific reports*, Vol. 4, p. 4348, 2014.

8. Goins, A. B., H. Sanabria and M. N. Waxham, "Macromolecular crowding and

size effects on probe microviscosity", *Biophysical Journal*, Vol. 95, No. 11, pp. 5362–5373, 2008.

9. Zhang, J., P. C. Johnson and A. S. Popel, "Red blood cell aggregation and dissociation in shear flows simulated by lattice Boltzmann method", *J. Biomech.*, Vol. 41, No. 1, pp. 47–55, 2008.

10. Ye, T., N. Phan-Thien, B. C. Khoo and C. T. Lim, "Dissipative particle dynamics simulations of deformation and aggregation of healthy and diseased red blood cells in a tube flow", *Phys. Fluids*, Vol. 26, No. 11, p. 111902, 2014.

11. Xiao, L., Y. Liu, S. Chen and B. Fu, "Simulation of Deformation and Aggregation of Two Red Blood Cells in a Stenosed Microvessel by Dissipative Particle Dynamics", *Cell Biochem. Biophys.*, Vol. 74, No. 4, pp. 513–525, 2016.

12. Maklygin, A. Y., A. V. Priezzhev, A. Karmenian, S. Y. Nikitin, I. Obolenskii, A. E. Lugovtsov and K. Li, "Measurement of interaction forces between red blood cells in aggregates by optical tweezers", *Quantum Electronics*, Vol. 42, No. 6, p. 500, 2012.

13. Bell, A. G., "ART. XXXIV.–On the Production and Reproduction of Sound by Light", *American Journal of Science (1880-1910)*, Vol. 20, No. 118, p. 305, 1880.

14. Kruger, R. A., P. Liu, Y. Fang, C. R. Appledorn *et al.*, "Photoacoustic ultrasound (PAUS)–reconstruction tomography", *Medical Physics*, Vol. 22, No. 10, pp. 1605–1609, 1995.

15. Xu, M. and L. V. Wang, "Photoacoustic imaging in biomedicine", *Review of scientific instruments*, Vol. 77, No. 4, p. 041101, 2006.

16. Harrison, T., J. C. Ranasinghesagara, H. Lu, K. Mathewson, A. Walsh and R. J. Zemp, "Combined photoacoustic and ultrasound biomicroscopy", *Optics express*, Vol. 17, No. 24, pp. 22041–22046, 2009.

17. Wang, L. V., "Tutorial on photoacoustic microscopy and computed tomography", *IEEE J. Sel. Top. Quantum Electron.*, Vol. 14, No. 1, pp. 171–179, 2008.

18. Li, C. and L. V. Wang, "Photoacoustic tomography and sensing in biomedicine", *Physics in Medicine & Biology*, Vol. 54, No. 19, p. R59, 2009.

19. Wells, P. N., "Ultrasonic imaging of the human body", *Reports on progress in physics*, Vol. 62, No. 5, p. 671, 1999.

20. Mundy, A. R., J. Fitzpatrick, D. E. Neal and N. J. George, *The scientific basis of urology*, CRC Press, 2010.

21. Beard, P., "Biomedical photoacoustic imaging", *Interface focus*, p. rsfs20110028, 2011.

22. Biswas, D., S. Vasudevan, G. C. Chen, P. Bhagat, N. Sharma and S. Phatak, "Time–frequency based photoacoustic spectral response technique for differentiating human breast masses", *Biomed. Phys. Eng. Express*, Vol. 3, No. 3, p. 035002, 2017.

23. Saha, R. K., S. Karmakar and M. Roy, "Photoacoustic response of suspended and hemolyzed red blood cells", *Appl. Phys. Lett.*, Vol. 103, No. 4, p. 044101, 2013.

24. Hysi, E., R. K. Saha and M. C. Kolios, "On the use of photoacoustics to detect red blood cell aggregation", *Biomed. Opt. Exp.*, Vol. 3, No. 9, pp. 2326–2338, 2012.

25. Zhang, H. and K.-K. Liu, "Optical tweezers for single cells", *Journal of The Royal Society Interface*, Vol. 5, No. 24, pp. 671–690, 2008.

26. Ashkin, A., "Acceleration and trapping of particles by radiation pressure", *Physical review letters*, Vol. 24, No. 4, p. 156, 1970.

27. Ashkin, A., J. M. Dziedzic, J. Bjorkholm and S. Chu, "Observation of a single-

beam gradient force optical trap for dielectric particles", *Optics letters*, Vol. 11, No. 5, pp. 288–290, 1986.

28. Griffiths, D. J., *Introduction to electrodynamics*, Prentice Hall, New Jersey, 2005.

29. Ashkin, A., "Forces of a single-beam gradient laser trap on a dielectric sphere in the ray optics regime", *Biophysical journal*, Vol. 61, No. 2, pp. 569–582, 1992.

30. Hénon, S., G. Lenormand, A. Richert and F. Gallet, "A new determination of the shear modulus of the human erythrocyte membrane using optical tweezers", *Biophys. J.*, Vol. 76, No. 2, pp. 1145–1151, 1999.

31. Dao, M., C. T. Lim and S. Suresh, "Mechanics of the human red blood cell deformed by optical tweezers", *J. Mech. Phys. Solids*, Vol. 51, No. 11, pp. 2259–2280, 2003.

32. Rundhaug, J. E., "Matrix Metalloproteinases, Angiogenesis, and Cancer: Commentary re: AC Lockhart et al., Reduction of Wound Angiogenesis in Patients Treated with BMS-275291, a Broad Spectrum Matrix Metalloproteinase Inhibitor. Clin. Cancer Res., 9: 00–00, 2003.", *Clinical Cancer Research*, Vol. 9, No. 2, pp. 551–554, 2003.

33. Razansky, D., N. J. Harlaar, J. L. Hillebrands, A. Taruttis, E. Herzog, C. J. Zeebregts, G. M. van Dam and V. Ntziachristos, "Multispectral optoacoustic tomography of matrix metalloproteinase activity in vulnerable human carotid plaques", *Molecular imaging and biology*, Vol. 14, No. 3, pp. 277–285, 2012.

34. Levi, J., S. R. Kothapalli, T.-J. Ma, K. Hartman, B. T. Khuri-Yakub and S. S. Gambhir, "Design, synthesis, and imaging of an activatable photoacoustic probe", *Journal of the American Chemical Society*, Vol. 132, No. 32, pp. 11264–11269, 2010.

35. Huh, D., W. Gu, Y. Kamotani, J. B. Grotberg and S. Takayama, "Microfluidics

for flow cytometric analysis of cells and particles", *Physiological measurement*, Vol. 26, No. 3, p. R73, 2005.

36. Sun, T. and H. Morgan, "Single-cell microfluidic impedance cytometry: a review", *Microfluidics and Nanofluidics*, Vol. 8, No. 4, pp. 423–443, 2010.

37. Pamme, N., R. Koyama and A. Manz, "Counting and sizing of particles and particle agglomerates in a microfluidic device using laser light scattering: application to a particle-enhanced immunoassay", *Lab on a Chip*, Vol. 3, No. 3, pp. 187–192, 2003.

38. Stone, H. A., A. D. Stroock and A. Ajdari, "Engineering flows in small devices: microfluidics toward a lab-on-a-chip", *Annu. Rev. Fluid Mech.*, Vol. 36, pp. 381–411, 2004.

39. Tehranirokh, M., A. Z. Kouzani, P. S. Francis and J. R. Kanwar, "Microfluidic devices for cell cultivation and proliferation", *Biomicrofluidics*, Vol. 7, No. 5, p. 051502, 2013.

40. Avigo, C., N. Di Lascio, P. Armanetti, C. Kusmic, L. Cavigli, F. Ratto, S. Meucci, C. Masciullo, M. Cecchini, R. Pini *et al.*, "Organosilicon phantom for photoacoustic imaging", *Journal of biomedical optics*, Vol. 20, No. 4, pp. 046008–046008, 2015.

41. Strohm, E. M., M. C. Kolios, D. K. Hwang, B.-U. Moon and S. S. Tsai, "Development of a microfluidic device with integrated high frequency ultrasound probe for particle characterization", *Ultrasonics Symposium (IUS), 2014 IEEE International*, pp. 1960–1963, IEEE, 2014.

42. Weber, J., P. C. Beard and S. E. Bohndiek, "Contrast agents for molecular photoacoustic imaging", *Nature methods*, Vol. 13, No. 8, p. 639, 2016.

43. Wu, D., L. Huang, M. S. Jiang and H. Jiang, "Contrast agents for photoacous-

tic and thermoacoustic imaging: a review", *International journal of molecular sciences*, Vol. 15, No. 12, pp. 23616–23639, 2014.

44. Jeon, M., W. Song, E. Huynh, J. Kim, J. Kim, B. L. Helfield, B. Y. Leung, D. E. Geortz, G. Zheng, J. Oh *et al.*, "Methylene blue microbubbles as a model dual-modality contrast agent for ultrasound and activatable photoacoustic imaging", *Journal of biomedical optics*, Vol. 19, No. 1, p. 016005, 2014.

45. Kim, C., R. Qin, J. S. Xu, L. V. Wang and R. X. Xu, "Multifunctional microbubbles and nanobubbles for photoacoustic and ultrasound imaging", *Journal of biomedical optics*, Vol. 15, No. 1, p. 010510, 2010.

46. Wilson, K. E., K. A. Homan and S. Y. Emelianov, "Remotely triggered contrast nanoagent for ultrasound and photoacoustic imaging", *Ultrasonics Symposium (IUS), 2010 IEEE*, pp. 1003–1006, IEEE, 2010.

47. Xu, R. X., "Multifunctional microbubbles and nanobubbles for photoacoustic imaging", *Contrast media & molecular imaging*, Vol. 6, No. 5, pp. 401–411, 2011.

48. Chen, Y.-S., S. J. Yoon, W. Frey, M. Dockery and S. Emelianov, "Dynamic contrast-enhanced photoacoustic imaging using photothermal stimuli-responsive composite nanomodulators", *Nature communications*, Vol. 8, p. 15782, 2017.

49. McGrath, T. E., G. J. Diebold, D. M. Bartels and R. A. Crowell, "Laser-initiated chemical reactions in carbon suspensions", *The Journal of Physical Chemistry A*, Vol. 106, No. 43, pp. 10072–10078, 2002.

50. Frez, C. and G. J. Diebold, "The photoacoustic effect from particles and bubbles", *The European Physical Journal Special Topics*, Vol. 153, No. 1, pp. 307–311, 2008.

51. González, M. G., X. Liu, R. Niessner and C. Haisch, "Strong size-dependent photoacoustic effect on gold nanoparticles by laser-induced nanobubbles", *Applied Physics Letters*, Vol. 96, No. 17, p. 174104, 2010.

52. Rayleigh, L., "VIII. On the pressure developed in a liquid during the collapse of a spherical cavity", *The London, Edinburgh, and Dublin Philosophical Magazine and Journal of Science*, Vol. 34, No. 200, pp. 94–98, 1917.

53. Brennen, C. E., *Cavitation and bubble dynamics*, Cambridge University Press, 2013.

54. Vokurka, K., "On Rayleigh's model of a freely oscillating bubble. I. Basic relations", *Czechoslovak Journal of Physics B*, Vol. 35, No. 1, pp. 28–40, 1985.

55. Simandoux, O., A. Prost, J. Gâteau and E. Bossy, "Influence of nanoscale temperature rises on photoacoustic generation: Discrimination between optical absorbers based on thermal nonlinearity at high frequency", *Photoacoustics*, Vol. 3, No. 1, pp. 20–25, 2015.

56. Lukianova-Hleb, E., Y. Hu, L. Latterini, L. Tarpani, S. Lee, R. A. Drezek, J. H. Hafner and D. O. Lapotko, "Plasmonic nanobubbles as transient vapor nanobubbles generated around plasmonic nanoparticles", *ACS nano*, Vol. 4, No. 4, pp. 2109–2123, 2010.

57. Oshemkov, S., L. Dvorkin and V. Y. Dmitriev, "Trapping and manipulating gas bubbles in water with ultrashort laser pulses at a high repetition rate", *Technical Physics Letters*, Vol. 35, No. 3, pp. 282–285, 2009.

58. Kotaidis, V., C. Dahmen, G. Von Plessen, F. Springer and A. Plech, "Excitation of nanoscale vapor bubbles at the surface of gold nanoparticles in water", *The Journal of chemical physics*, Vol. 124, No. 18, p. 184702, 2006.

59. Carlson, M. T., A. J. Green and H. H. Richardson, "Superheating water by CW excitation of gold nanodots", *Nano letters*, Vol. 12, No. 3, pp. 1534–1537, 2012.

60. Akhatov, I., N. Vakhitova, A. Topolnikov, K. Zakirov, B. Wolfrum, T. Kurz, O. Lindau, R. Mettin and W. Lauterborn, "Dynamics of laser-induced cavitation

bubbles", *Experimental thermal and fluid science*, Vol. 26, No. 6-7, pp. 731–737, 2002.

61. Angelsky, O., A. Y. Bekshaev, P. Maksimyak, A. Maksimyak, S. G. Hanson and S. Kontush, "Controllable generation and manipulation of micro-bubbles in water with absorptive colloid particles by CW laser radiation", *Optics express*, Vol. 25, No. 5, pp. 5232–5243, 2017.

62. Rastopov, S. and A. Sukhodol'sky, "Cluster nucleation in the process of CW laser induced thermocavitation", *Physics Letters A*, Vol. 149, No. 4, pp. 229–232, 1990.

63. Ramirez-San-Juan, J., E. Rodriguez-Aboytes, A. Martinez-Canton, O. Baldovino-Pantaleon, A. Robledo-Martinez, N. Korneev and R. Ramos-Garcia, "Time-resolved analysis of cavitation induced by CW lasers in absorbing liquids", *Optics Express*, Vol. 18, No. 9, pp. 8735–8742, 2010.

64. Padilla-Martinez, J., C. Berrospe-Rodriguez, G. Aguilar, J. Ramirez-San-Juan and R. Ramos-Garcia, "Optic cavitation with CW lasers: A review", *Physics of Fluids*, Vol. 26, No. 12, p. 122007, 2014.

65. Lajoinie, G., J.-Y. Lee, J. Owen, P. Kruizinga, N. de Jong, G. Van Soest, E. Stride and M. Versluis, "Laser-driven resonance of dye-doped oil-coated microbubbles: Experimental study", *The Journal of the Acoustical Society of America*, Vol. 141, No. 6, pp. 4832–4846, 2017.

66. Shah, J., S. Park, S. R. Aglyamov, T. Larson, L. Ma, K. V. Sokolov, K. P. Johnston, T. E. Milner and S. Y. Emelianov, "Photoacoustic imaging and temperature measurement for photothermal cancer therapy", *Journal of biomedical optics*, Vol. 13, No. 3, p. 034024, 2008.

67. Yeager, D., Y.-S. Chen, S. Litovsky and S. Emelianov, "Intravascular photoacoustics for image-guidance and temperature monitoring during plasmonic photothermal therapy of atherosclerotic plaques: a feasibility study", *Theranostics*, Vol. 4,

No. 1, p. 36, 2014.

68. Tian, C., Z. Xie, M. L. Fabiilli, S. Liu, C. Wang, Q. Cheng and X. Wang, "Dual-pulse nonlinear photoacoustic technique: a practical investigation", *Biomedical optics express*, Vol. 6, No. 8, pp. 2923–2933, 2015.

69. Gao, F., R. Kishor, X. Feng, S. Liu, R. Ding, R. Zhang and Y. Zheng, "An analytical study of photoacoustic and thermoacoustic generation efficiency towards contrast agent and film design optimization", *Photoacoustics*, Vol. 7, pp. 1–11, 2017.

70. Sigrist, M. W., "Laser generation of acoustic waves in liquids and gases", *Journal of applied physics*, Vol. 60, No. 7, pp. R83–R122, 1986.

71. Wang, L. V., "Multiscale photoacoustic microscopy and computed tomography", *Nature photonics*, Vol. 3, No. 9, p. 503, 2009.

72. Hu, S. and L. V. Wang, "Optical-resolution photoacoustic microscopy: auscultation of biological systems at the cellular level", *Biophysical journal*, Vol. 105, No. 4, pp. 841–847, 2013.

73. Zhang, H. F., K. Maslov, G. Stoica and L. V. Wang, "Functional photoacoustic microscopy for high-resolution and noninvasive in vivo imaging", *Nature biotechnology*, Vol. 24, No. 7, p. 848, 2006.

74. Maslov, K., H. F. Zhang, S. Hu and L. V. Wang, "Optical-resolution photoacoustic microscopy for in vivo imaging of single capillaries", *Optics letters*, Vol. 33, No. 9, pp. 929–931, 2008.

75. Li, G., K. I. Maslov and L. V. Wang, "Reflection-mode multifocal optical-resolution photoacoustic microscopy", *Journal of biomedical optics*, Vol. 18, No. 3, p. 030501, 2013.

76. Xie, Z., W. Roberts, P. Carson, X. Liu, C. Tao and X. Wang, "Evaluation of bladder microvasculature with high-resolution photoacoustic imaging", *Optics letters*, Vol. 36, No. 24, pp. 4815–4817, 2011.

77. Wang, L. V., X. Zhao, H. Sun and G. Ku, "Microwave-induced acoustic imaging of biological tissues", *Review of scientific instruments*, Vol. 70, No. 9, pp. 3744–3748, 1999.

78. Zhang, H. F., K. Maslov and L. V. Wang, "In vivo imaging of subcutaneous structures using functional photoacoustic microscopy", *Nature protocols*, Vol. 2, No. 4, p. 797, 2007.

79. Allen, T. J. and P. C. Beard, "Pulsed near-infrared laser diode excitation system for biomedical photoacoustic imaging", *Optics letters*, Vol. 31, No. 23, pp. 3462–3464, 2006.

80. Ku, G. and L. V. Wang, "Deeply penetrating photoacoustic tomography in biological tissues enhanced with an optical contrast agent", *Optics letters*, Vol. 30, No. 5, pp. 507–509, 2005.

81. Zeng, L., G. Liu, D. Yang and X. Ji, "3D-visual laser-diode-based photoacoustic imaging", *Optics express*, Vol. 20, No. 2, pp. 1237–1246, 2012.

82. Zeng, L., G. Liu, D. Yang and X. Ji, "Portable optical-resolution photoacoustic microscopy with a pulsed laser diode excitation", *Applied physics letters*, Vol. 102, No. 5, p. 053704, 2013.

83. Zeng, L., G. Liu, D. Yang and X. Ji, "Cost-efficient laser-diode-induced optical-resolution photoacoustic microscopy for two-dimensional/three-dimensional biomedical imaging", *Journal of biomedical optics*, Vol. 19, No. 7, p. 076017, 2014.

84. Wang, T., S. Nandy, H. S. Salehi, P. D. Kumavor and Q. Zhu, "A low-cost pho-

toacoustic microscopy system with a laser diode excitation", *Biomedical Optics Express*, Vol. 5, No. 9, pp. 3053–3058, 2014.

85. Kolkman, R. G., W. Steenbergen and T. G. van Leeuwen, "In vivo photoacoustic imaging of blood vessels with a pulsed laser diode", *Lasers in medical science*, Vol. 21, No. 3, pp. 134–139, 2006.

86. Zeng, L., Z. Piao, S. Huang, W. Jia and Z. Chen, "Label-free optical-resolution photoacoustic microscopy of superficial microvasculature using a compact visible laser diode excitation", *Optics express*, Vol. 23, No. 24, pp. 31026–31033, 2015.

87. Favazza, C. P., L. V. Wang, O. W. Jassim and L. A. Cornelius, "In vivo photoacoustic microscopy of human cutaneous microvasculature and a nevus", *Journal of biomedical optics*, Vol. 16, No. 1, p. 016015, 2011.

88. Li, L., R. J. Zemp, G. F. Lungu, G. Stoica and L. V. Wang, "Photoacoustic imaging of lacZ gene expression in vivo", *Journal of biomedical optics*, Vol. 12, No. 2, p. 020504, 2007.

89. Krumholz, A., J. Yao, L. V. Wang, T. Fleming, W. E. Gillanders *et al.*, "Photoacoustic microscopy of tyrosinase reporter gene in vivo", *Journal of biomedical optics*, Vol. 16, No. 8, p. 080503, 2011.

90. Wang, T., Y. Yang, U. Alqasemi, P. D. Kumavor, X. Wang, M. Sanders, M. Brewer and Q. Zhu, "Characterization of ovarian tissue based on quantitative analysis of photoacoustic microscopy images", *Biomedical optics express*, Vol. 4, No. 12, pp. 2763–2768, 2013.

91. Song, K. and L. V. Wang, "Deep reflection-mode photoacoustic imaging of biological tissue", *Journal of biomedical optics*, Vol. 12, No. 6, p. 060503, 2007.

92. Song, K. H., C. Kim, K. Maslov and L. V. Wang, "Noninvasive in vivo spectroscopic nanorod-contrast photoacoustic mapping of sentinel lymph nodes", *Euro-*

pean journal of radiology, Vol. 70, No. 2, pp. 227–231, 2009.

93. Yao, D.-K., K. I. Maslov, L. V. Wang, R. Chen and Q. Zhou, "Optimal ultraviolet wavelength for in vivo photoacoustic imaging of cell nuclei", *Journal of biomedical optics*, Vol. 17, No. 5, p. 056004, 2012.

94. Li, C., A. Aguirre, J. K. Gamelin, A. Maurudis, Q. Zhu and L. V. Wang, "Real-time photoacoustic tomography of cortical hemodynamics in small animals", *Journal of biomedical optics*, Vol. 15, No. 1, p. 010509, 2010.

95. Ai, M., W. Shu, T. Salcudean, R. Rohling, P. Abolmaesumi and S. Tang, "High energy laser pulse coupling in a multimode fiber for photoacoustic tomography", *Photons Plus Ultrasound: Imaging and Sensing 2016*, Vol. 9708, p. 97084H, International Society for Optics and Photonics, 2016.

96. Cao, R., J. P. Kilroy, B. Ning, T. Wang, J. A. Hossack and S. Hu, "Multispectral photoacoustic microscopy based on an optical–acoustic objective", *Photoacoustics*, Vol. 3, No. 2, pp. 55–59, 2015.

97. Zhang, C., K. I. Maslov, J. Yao and L. V. Wang, "In vivo photoacoustic microscopy with 7.6-μm axial resolution using a commercial 125-MHz ultrasonic transducer", *Journal of biomedical optics*, Vol. 17, No. 11, p. 116016, 2012.

98. Billeh, Y. N., M. Liu and T. Buma, "Spectroscopic photoacoustic microscopy using a photonic crystal fiber supercontinuum source", *Optics express*, Vol. 18, No. 18, pp. 18519–18524, 2010.

99. Lee, C., S. Han, S. Kim, M. Jeon, M. Y. Jeon, C. Kim and J. Kim, "Combined photoacoustic and optical coherence tomography using a single near-infrared supercontinuum laser source", *Applied optics*, Vol. 52, No. 9, pp. 1824–1828, 2013.

100. Lee, C., M. Jeon, M. Y. Jeon, J. Kim and C. Kim, "In vitro photoacoustic measurement of hemoglobin oxygen saturation using a single pulsed broadband su-

percontinuum laser source", *Applied optics*, Vol. 53, No. 18, pp. 3884–3889, 2014.

101. Shu, X., M. Bondu, B. Dong, A. Podoleanu, L. Leick and H. F. Zhang, "Single all-fiber-based nanosecond-pulsed supercontinuum source for multispectral photoacoustic microscopy and optical coherence tomography", *Optics letters*, Vol. 41, No. 12, pp. 2743–2746, 2016.

102. Loya, A. K., J. Dumas and T. Buma, "Photoacoustic microscopy with a tunable source based on cascaded stimulated Raman scattering in a large-mode area photonic crystal fiber", *Ultrasonics Symposium (IUS), 2012 IEEE International*, pp. 1208–1211, IEEE, 2012.

103. Koeplinger, D., M. Liu and T. Buma, "Photoacoustic microscopy with a pulsed multi-color source based on stimulated Raman scattering", *Ultrasonics Symposium (IUS), 2011 IEEE International*, pp. 296–299, IEEE, 2011.

104. Ferrari, M. R., J. L. Farland and T. Buma, "Photoacoustic microscopy using four-wave mixing in a multimode fiber", *Ultrasonics Symposium (IUS), 2015 IEEE International*, pp. 1–4, IEEE, 2015.

105. Buma, T., B. C. Wilkinson and T. C. Sheehan, "Near-infrared spectroscopic photoacoustic microscopy using a multi-color fiber laser source", *Biomedical optics express*, Vol. 6, No. 8, pp. 2819–2829, 2015.

106. Liu, M. and T. Buma, "Wavelength agile photoacoustic microscopy with a photonic crystal fiber supercontinuum source", *Photons Plus Ultrasound: Imaging and Sensing 2011*, Vol. 7899, p. 789944, International Society for Optics and Photonics, 2011.

107. Bondu, M. M., C. D. Brooks, C. Jakobsen, K. Oakes, P. M. Moselund, L. Leick, O. Bang and A. Podoleanu, "High energy supercontinuum sources using tapered photonic crystal fibers for multispectral photoacoustic microscopy", *Journal of biomedical optics*, Vol. 21, No. 6, p. 061005, 2016.

108. Hajireza, P., A. Forbrich and R. Zemp, "In-vivo functional optical-resolution photoacoustic microscopy with stimulated Raman scattering fiber-laser source", *Biomedical optics express*, Vol. 5, No. 2, pp. 539–546, 2014.

109. Serebryannikov, E. and A. Zheltikov, "Supercontinuum generation through cascaded four-wave mixing in photonic-crystal fibers: When picoseconds do it better", *Optics communications*, Vol. 274, No. 2, pp. 433–440, 2007.

110. Dudley, J. M., G. Genty and S. Coen, "Supercontinuum generation in photonic crystal fiber", *Reviews of modern physics*, Vol. 78, No. 4, p. 1135, 2006.

111. Boucon, A., T. Sylvestre, K. P. Huy, J.-C. Beugnot, G. Mélin, H. Maillotte and J. M. Dudley, "Supercontinuum generation by nanosecond dual-pumping near the two zero-dispersion wavelengths of a photonic crystal fiber", *Optics communications*, Vol. 284, No. 1, pp. 467–470, 2011.

112. Wadsworth, W. J., N. Joly, J. C. Knight, T. A. Birks, F. Biancalana and P. S. J. Russell, "Supercontinuum and four-wave mixing with Q-switched pulses in endlessly single-mode photonic crystal fibres", *Optics express*, Vol. 12, No. 2, pp. 299–309, 2004.

113. Dudley, J. M., L. Provino, N. Grossard, H. Maillotte, R. S. Windeler, B. J. Eggleton and S. Coen, "Supercontinuum generation in air–silica microstructured fibers with nanosecond and femtosecond pulse pumping", *JOSA B*, Vol. 19, No. 4, pp. 765–771, 2002.

114. Shi, W., P. Hajireza, P. Shao, A. Forbrich and R. J. Zemp, "In vivo near-realtime volumetric optical-resolution photoacoustic microscopy using a high-repetition-rate nanosecond fiber-laser", *Optics express*, Vol. 19, No. 18, pp. 17143–17150, 2011.

115. Shi, W., P. Shao, P. Hajireza, A. Forbrich and R. J. Zemp, "In vivo dynamic process imaging using real-time optical-resolution photoacoustic microscopy", *Jour-*

nal of biomedical optics, Vol. 18, No. 2, p. 026001, 2013.

116. Hajireza, P., W. Shi and R. Zemp, "Label-free in vivo fiber-based optical-resolution photoacoustic microscopy", *Optics letters*, Vol. 36, No. 20, pp. 4107–4109, 2011.

117. Shi, W., S. M. Kerr, I. A. Utkin, J. C. Ranasinghesagara, L. Pan, Y. B. Godwal, R. J. Zemp and R. Fedosejevs, "Optical resolution photoacoustic microscopy using novel high-repetition-rate passively Q-switched microchip and fiber lasers", *Journal of biomedical optics*, Vol. 15, No. 5, p. 056017, 2010.

118. Wang, Y., K. I. Maslov, Y. Zhang, S. Hu, L.-M. Yang, Y. Xia, J. Liu and L. V. Wang, "Fiber-laser-based photoacoustic microscopy and melanoma cell detection", *Journal of biomedical optics*, Vol. 16, No. 1, p. 011014, 2011.

119. Nedosekin, D. A., M. Sarimollaoglu, E. V. Shashkov, E. I. Galanzha and V. P. Zharov, "Ultra-fast photoacoustic flow cytometry with a 0.5 MHz pulse repetition rate nanosecond laser", *Optics express*, Vol. 18, No. 8, pp. 8605–8620, 2010.

120. Hajireza, P., A. Forbrich, Y. Jiang, W. Shi and R. Zemp, "In vivo multi-wavelength optical-resolution photoacoustic microscopy with stimulated Raman scattering fiber-laser source", *Photons Plus Ultrasound: Imaging and Sensing 2013*, Vol. 8581, p. 858129, International Society for Optics and Photonics, 2013.

121. Hajireza, P., A. Forbrich and R. J. Zemp, "Multifocus optical-resolution photoacoustic microscopy using stimulated Raman scattering and chromatic aberration", *Optics letters*, Vol. 38, No. 15, pp. 2711–2713, 2013.

122. Allen, T., M. Berendt, J. Spurrell, S. Alam, E. Zhang, D. Richardson and P. Beard, "Novel fibre lasers as excitation sources for photoacoustic tomography and microscopy", *Photons Plus Ultrasound: Imaging and Sensing 2016*, Vol. 9708, p. 97080W, International Society for Optics and Photonics, 2016.

123. Mahmud, M. S., A. Forbrich, P. Shao, W. Shi and R. J. Zemp, "A tunable MOPA laser for real-time optical resolution photoacoustic microscopy", *Photons Plus Ultrasound: Imaging and Sensing 2015*, Vol. 9323, p. 93233V, International Society for Optics and Photonics, 2015.

124. Chen, H., S. Chen, J. Wang, Z. Chen and J. Hou, "35 W high power all fiber supercontinuum generation in PCF with picosecond MOPA laser", *Optics communications*, Vol. 284, No. 23, pp. 5484–5487, 2011.

125. Ilday, F. Ö., H. Lim, J. Buckley and F. Wise, "Practical all-fiber source of high-power, 120-fs pulses at 1 μm", *Optics letters*, Vol. 28, No. 15, pp. 1362–1364, 2003.

126. Yao, D.-K., R. Chen, K. Maslov, Q. Zhou and L. V. Wang, "In vivo imaging of cell nuclei by photoacoustic microscopy without staining", *Photons Plus Ultrasound: Imaging and Sensing 2012*, Vol. 8223, p. 82231X, International Society for Optics and Photonics, 2012.

127. Yao, D.-K., K. Maslov, K. K. Shung, Q. Zhou and L. V. Wang, "In vivo label-free photoacoustic microscopy of cell nuclei by excitation of DNA and RNA", *Optics letters*, Vol. 35, No. 24, pp. 4139–4141, 2010.

128. Maker, P., R. Terhune, M. Nisenoff and C. Savage, "Effects of dispersion and focusing on the production of optical harmonics", *Physical review letters*, Vol. 8, No. 1, p. 21, 1962.

129. Eckardt, R. and J. Reintjes, "Phase matching limitations of high efficiency second harmonic generation", *IEEE journal of quantum electronics*, Vol. 20, No. 10, pp. 1178–1187, 1984.

130. Møller, U., S. T. Sørensen, C. Larsen, P. M. Moselund, C. Jakobsen, J. Johansen, C. L. Thomsen and O. Bang, "Optimum PCF tapers for blue-enhanced supercontinuum sources", *Optical fiber technology*, Vol. 18, No. 5, pp. 304–314, 2012.

131. Stone, J. M. and J. C. Knight, "Visibly "white" light generation in uniform photonic crystal fiber using a microchip laser", *Optics express*, Vol. 16, No. 4, pp. 2670–2675, 2008.

132. Sørensen, S. T., U. Møller, C. Larsen, P. Moselund, C. Jakobsen, J. Johansen, T. Andersen, C. Thomsen and O. Bang, "Deep-blue supercontinnum sources with optimum taper profiles–verification of GAM", *Optics express*, Vol. 20, No. 10, pp. 10635–10645, 2012.

133. Cranston, H. A., C. W. Boylan, G. Carroll, S. P. Sutera, J. Williamson, I. Y. Gluzman and D. J. Krogstad, "Plasmodium falciparum maturation abolishes physiologic red cell deformability", *Science*, Vol. 223, pp. 400–404, 1984.

134. Shelby, J. P., J. White, K. Ganesan, P. K. Rathod and D. T. Chiu, "A microfluidic model for single-cell capillary obstruction by Plasmodium falciparum-infected erythrocytes", *Proc. Natl. Acad. Sci.*, Vol. 100, No. 25, pp. 14618–14622, 2003.

135. Ingram, V. M., "Gene mutations in human haemoglobin: the chemical difference between normal and sickle cell haemoglobin", *Nature*, Vol. 180, No. 4581, pp. 326–328, 1957.

136. Kaul, D. K., M. Fabry, P. Windisch, S. Baez and R. Nagel, "Erythrocytes in sickle cell anemia are heterogeneous in their rheological and hemodynamic characteristics.", *J. Clin. Invest.*, Vol. 72, No. 1, p. 22, 1983.

137. Evans, E. and A. Yeung, "Hidden dynamics in rapid changes of bilayer shape", *Chem. Phys. Lipids*, Vol. 73, No. 1, pp. 39–56, 1994.

138. Barabino, G. A., M. O. Platt and D. K. Kaul, "Sickle cell biomechanics", *Annu. Rev. Biomed. Eng.*, Vol. 12, pp. 345–367, 2010.

139. Strohm, E. M., E. S. Berndl and M. C. Kolios, "High frequency label-free photoacoustic microscopy of single cells", *Photoacoustics*, Vol. 1, No. 3, pp. 49–53,

2013.

140. Strohm, E. M. and M. C. Kolios, "Classification of blood cells and tumor cells using label-free ultrasound and photoacoustics", *Cytometry Part A*, Vol. 87, No. 8, pp. 741–749, 2015.

141. He, G., B. Li and S. Yang, "In vivo imaging of a single erythrocyte with high-resolution photoacoustic microscopy", *Front. Optoelectron.*, Vol. 8, No. 2, pp. 122–127, 2015.

142. Feng, T., Q. Li, C. Zhang, G. Xu, L. J. Guo, J. Yuan and X. Wang, "Characterizing cellular morphology by photoacoustic spectrum analysis with an ultra-broadband optical ultrasonic detector", *Opt. Exp.*, Vol. 24, No. 17, pp. 19853–19862, 2016.

143. Karpiouk, A. B., S. R. Aglyamov, S. Mallidi, J. Shah, W. G. Scott, J. M. Rubin and S. Y. Emelianov, "Combined ultrasound and photoacoustic imaging to detect and stage deep vein thrombosis: phantom and ex vivo studies", *J. Biomed. Opt.*, Vol. 13, No. 5, pp. 054061–054061, 2008.

144. Rui, M., W. Bost, E. Weiss, R. Lemor and M. C. Kolios, "Photoacoustic microscopy and spectroscopy of individual red blood cells", *Proc SPIE*, 2010.

145. Strohm, E. M., E. S. Berndl and M. C. Kolios, "Probing red blood cell morphology using high-frequency photoacoustics", *Biophys. J.*, Vol. 105, No. 1, pp. 59–67, 2013.

146. Talbert, R. J., S. H. Holan and J. A. Viator, "Photoacoustic discrimination of viable and thermally coagulated blood using a two-wavelength method for burn injury monitoring", *Phys. Med. Biol.*, Vol. 52, No. 7, p. 1815, 2007.

147. Salehi, H. S., H. Li, A. Merkulov, P. D. Kumavor, H. Vavadi, M. Sanders, A. Kueck, M. A. Brewer and Q. Zhu, "Coregistered photoacoustic and ultra-

sound imaging and classification of ovarian cancer: ex vivo and in vivo studies", *Journal of Biomedical Optics*, Vol. 21, No. 4, pp. 046006–046006, 2016.

148. Aytac-Kipergil, E., A. Demirkiran, N. Uluc, S. Yavas, T. Kayikcioglu, S. Salman, S. G. Karamuk, F. O. Ilday and M. B. Unlu, "Development of a fiber laser with independently adjustable properties for optical resolution photoacoustic microscopy", *Scientific Reports*, Vol. 6, p. 38674, 2016.

149. Kamruzzahan, A., F. Kienberger, C. M. Stroh, J. Berg, R. Huss, A. Ebner, R. Zhu, C. Rankl, H. J. Gruber and P. Hinterdorfer, "Imaging morphological details and pathological differences of red blood cells using tapping-mode AFM", *Biol. Chem.*, Vol. 385, No. 10, pp. 955–960, 2004.

150. Dulińska, I., M. Targosz, W. Strojny, M. Lekka, P. Czuba, W. Balwierz and M. Szymoński, "Stiffness of normal and pathological erythrocytes studied by means of atomic force microscopy", *J. Biochem. Biophys. Meth.*, Vol. 66, No. 1, pp. 1–11, 2006.

151. Fornal, M., M. Lekka, G. Pyka-Fościak, K. Lebed, T. Grodzicki, B. Wizner and J. Styczeń, "Erythrocyte stiffness in diabetes mellitus studied with atomic force microscope", *Clin. Hemorheol. Microcirc.*, Vol. 35, No. 1, 2, pp. 273–276, 2006.

152. Maciaszek, J. L., B. Andemariam and G. Lykotrafitis, "Microelasticity of red blood cells in sickle cell disease", *J. Strain Anal. Eng. Des.*, Vol. 46, No. 5, pp. 368–379, 2011.

153. Evans, E. A. and P. L. La Celle, "Intrinsic material properties of the erythrocyte membrane indicated by mechanical analysis of deformation", *Blood*, Vol. 45, No. 1, pp. 29–43, 1975.

154. Discher, D. E., D. H. Boal and S. K. Boey, "Simulations of the erythrocyte cytoskeleton at large deformation. II. Micropipette aspiration", *Biophys. J.*, Vol. 75, No. 3, pp. 1584–1597, 1998.

155. Shiga, T., N. Maeda and K. Kon, "Erythrocyte rheology", *Crit. Rev. Oncol. Hematol.*, Vol. 10, No. 1, pp. 9–48, 1990.

156. Hochmuth, R. M., "Micropipette aspiration of living cells", *J. Biomech.*, Vol. 33, No. 1, pp. 15–22, 2000.

157. Guck, J., R. Ananthakrishnan, H. Mahmood, T. J. Moon, C. C. Cunningham and J. Käs, "The optical stretcher: a novel laser tool to micromanipulate cells", *Biophys. J.*, Vol. 81, No. 2, pp. 767–784, 2001.

158. Yoon, Y. Z., J. Kotar, A. T. Brown and P. Cicuta, "Red blood cell dynamics: from spontaneous fluctuations to non-linear response", *Soft Matter*, Vol. 7, No. 5, pp. 2042–2051, 2011.

159. Kilinc, D. and G. U. Lee, "Advances in magnetic tweezers for single molecule and cell biophysics", *Integr. Biol.*, Vol. 6, No. 1, pp. 27–34, 2014.

160. Fedosov, D. A., B. Caswell and G. E. Karniadakis, "A multiscale red blood cell model with accurate mechanics, rheology, and dynamics", *Biophys. J.*, Vol. 98, No. 10, pp. 2215–2225, 2010.

161. Li, J., G. Lykotrafitis, M. Dao and S. Suresh, "Cytoskeletal dynamics of human erythrocyte", *Proc. Natl. Acad. Sci.*, Vol. 104, No. 12, pp. 4937–4942, 2007.

162. Bow, H., I. V. Pivkin, M. Diez-Silva, S. J. Goldfless, M. Dao, J. C. Niles, S. Suresh and J. Han, "A microfabricated deformability based flow cytometer with application to malaria", *Lab Chip.*, Vol. 11, No. 6, pp. 1065–1073, 2011.

163. Diez-Silva, M., Y. Park, S. Huang, H. Bow, O. Mercereau-Puijalon, G. Deplaine, C. Lavazec, S. Perrot, S. Bonnefoy, M. S. Feld *et al.*, "Pf155 RESA protein influences the dynamic microcirculatory behavior of ring-stage Plasmodium falciparum infected red blood cells", *Sci. Rep.*, Vol. 2, p. 614, 2012.

164. Dubus, C. and J.-B. Fournier, "A Gaussian model for the membrane of red blood cells with cytoskeletal defects", *Europhys. Lett.*, Vol. 75, No. 1, p. 181, 2006.

165. Strohm, E. M., I. Gorelikov, N. Matsuura and M. C. Kolios, "Modeling photoacoustic spectral features of micron-sized particles", *Phys. Med. Biol.*, Vol. 59, No. 19, p. 5795, 2014.

166. Saha, R. K., S. Karmakar, A. Adhikari and M. C. Kolios, "Photoacoustic field calculation for nonspherical axisymmetric fluid particles", *Biomed. Phys. Eng. Express*, Vol. 3, No. 1, p. 015017, 2017.

167. Musielak, M., "Red blood cell-deformability measurement: review of techniques", *Clin. Hemorheol. Microcirc.*, Vol. 42, No. 1, pp. 47–64, 2009.

168. Rico, F., P. Roca-Cusachs, N. Gavara, R. Farré, M. Rotger and D. Navajas, "Probing mechanical properties of living cells by atomic force microscopy with blunted pyramidal cantilever tips", *Phys. Rev. E*, Vol. 72, No. 2, p. 021914, 2005.

169. Bausch, A. R., W. Möller and E. Sackmann, "Measurement of local viscoelasticity and forces in living cells by magnetic tweezers", *Biophys. J.*, Vol. 76, No. 1, pp. 573–579, 1999.

170. Song, W., W. Zheng, R. Liu, R. Lin, H. Huang, X. Gong, S. Yang, R. Zhang and L. Song, "Reflection-mode in vivo photoacoustic microscopy with subwavelength lateral resolution", *Biomed. Opt. Exp.*, Vol. 5, No. 12, pp. 4235–4241, 2014.

171. Strohm, E. M., M. J. Moore and M. C. Kolios, "Single cell photoacoustic microscopy: a review", *IEEE J. Sel. Top. Quantum Electron.*, Vol. 22, No. 3, pp. 137–151, 2016.

172. Saha, R. K., S. Karmakar and M. Roy, "Computational investigation on the photoacoustics of malaria infected red blood cells", *PLoS One*, Vol. 7, No. 12, p. e51774, 2012.

173. Saha, R. K. and M. C. Kolios, "Effects of erythrocyte oxygenation on optoacoustic signals", *J. Biomed. Opt.*, Vol. 16, No. 11, pp. 115003–1150039, 2011.

174. Diebold, G., "Photoacoustic monopole radiation: waves from objects with symmetry in one, two and three dimensions", *Photoacoustic imaging and spectroscopy*, Vol. 144, pp. 3–17, 2009.

175. Hysi, E., R. K. Saha and M. C. Kolios, "Characterization of red blood cell aggregation with photoacoustics: A theoretical and experimental study", *Proc IUS*, pp. 1187–1190, 2011.

176. Saha, R. K. and M. C. Kolios, "A simulation study on photoacoustic signals from red blood cells", *J. Acoust. Soc. Am.*, Vol. 129, No. 5, pp. 2935–2943, 2011.

177. Solano, R. P., F. I. Ramirez-Perez, J. A. Castorena-Gonzalez, E. A. Anell, G. Gutiérrez-Juárez and L. Polo-Parada, "An experimental and theoretical approach to the study of the photoacoustic signal produced by cancer cells", *AIP Adv.*, Vol. 2, No. 1, p. 011102, 2012.

178. Li, Y., H. Fang, C. Min and X. Yuan, "Analytic theory of photoacoustic wave generation from a spheroidal droplet", *Opt. Exp.*, Vol. 22, No. 17, pp. 19953–19969, 2014.

179. Liu, Y. and W. K. Liu, "Rheology of red blood cell aggregation by computer simulation", *J. Comput. Phys.*, Vol. 220, No. 1, pp. 139–154, 2006.

180. Wang, L. and H.-i. Wu, "Biomedical Optics: Principles and Imaging Wiley", *New York*, 2007.

181. Fisher, A. R., A. J. Schissler and J. C. Schotland, "Photoacoustic effect for multiply scattered light", *Phys. Rev. E*, Vol. 76, No. 3, p. 036604, 2007.

182. Wang, T., U. Rongin and Z. Xing, "A micro-scale simulation of red blood cell

passage through symmetric and asymmetric bifurcated vessels", *Sci. Rep.*, Vol. 6, 2016.

183. Zhang, J., P. C. Johnson and A. S. Popel, "An immersed boundary lattice Boltzmann approach to simulate deformable liquid capsules and its application to microscopic blood flows", *Phys. Biol.*, Vol. 4, No. 4, p. 285, 2007.

184. Morse, P. M. and H. Feshbach, *Methods of theoretical physics*, Technology Press, 1946.

185. Wang, L. V. and H.-i. Wu, *Biomedical optics: principles and imaging*, John Wiley & Sons, 2012.

186. Erkol, H., E. Aytac-Kipergil and M. B. Unlu, "Photoacoustic radiation force on a microbubble", *Phys. Rev. E*, Vol. 90, No. 2, p. 023001, 2014.

187. Peskin, C. S., "Numerical analysis of blood flow in the heart", *J. Comput. Phys.*, Vol. 25, No. 3, pp. 220–252, 1977.

188. Liu, Y., L. Zhang, X. Wang and W. K. Liu, "Coupling of Navier–Stokes equations with protein molecular dynamics and its application to hemodynamics", *Int. J. Numer. Methods Fluids*, Vol. 46, No. 12, pp. 1237–1252, 2004.

189. Tsubuto, K.-i., S. Wada and T. Yamaguchi, "Simulation study on effects of hematocrit on blood flow properties using particle method", *J. Biomech. Sci. Eng.*, Vol. 1, No. 1, pp. 159–170, 2006.

190. Késmárky, G., P. Kenyeres, M. Rábai and K. Tóth, "Plasma viscosity: a forgotten variable", *Clin. Hemorheol. Microcirc.*, Vol. 39, No. 1–4, pp. 243–246, 2008.

191. Neu, B. and H. J. Meiselman, "Depletion-mediated red blood cell aggregation in polymer solutions", *Biophysical journal*, Vol. 83, No. 5, pp. 2482–2490, 2002.

192. Abramowitz, M. and I. A. Stegun, *Handbook of mathematical functions: with*

formulas, graphs, and mathematical tables, Vol. 55, Courier Corporation, 1964.

193. Arfken, G. B., H. J. Weber and F. E. Harris, *Mathematical methods for physicists: a comprehensive guide*, Academic Press, 2011.

194. Strohm, E. M., E. Hysi and M. C. Kolios, "Photoacoustic measurements of single red blood cells", *Proc IUS*, pp. 1406–1409, 2012.

195. Bai, X., Y. Liang, H. Sun, L. Jin, J. Ma, B.-O. Guan and L. Wang, "Sensitivity characteristics of broadband fiber-laser-based ultrasound sensors for photoacoustic microscopy", *Optics Express*, Vol. 25, No. 15, pp. 17616–17626, 2017.

196. Demirkiran, A., A. Karakuzu, H. Erkol, H. Torun and M. B. Unlu, "Analysis of microcantilevers excited by pulsed-laser-induced photoacoustic waves", *Optics Express*, Vol. 26, No. 4, pp. 4906–4919, 2018.

197. Ohlinger, A., A. Deak, A. A. Lutich and J. Feldmann, "Optically trapped gold nanoparticle enables listening at the microscale", *Physical Review Letters*, Vol. 108, No. 1, p. 018101, 2012.

198. Park, Y., C. A. Best, K. Badizadegan, R. R. Dasari, M. S. Feld, T. Kuriabova, M. L. Henle, A. J. Levine and G. Popescu, "Measurement of red blood cell mechanics during morphological changes", *Proceedings of the National Academy of Sciences*, Vol. 107, No. 15, pp. 6731–6736, 2010.

199. Flügge, S., *Practical quantum mechanics*, Springer Science & Business Media, 2012.

200. Hysi, E., R. K. Saha and M. C. Kolios, "Photoacoustic ultrasound spectroscopy for assessing red blood cell aggregation and oxygenation", *J. Biomed. Opt.*, Vol. 17, No. 12, pp. 125006–125006, 2012.

201. Bayer, C. L., S. Y. Nam, Y.-S. Chen and S. Y. Emelianov, "Photoacoustic signal

amplification through plasmonic nanoparticle aggregation", *Journal of Biomedical Optics*, Vol. 18, No. 1, pp. 016001–016001, 2013.

202. Peskin, C. S., "Flow patterns around heart valves: a numerical method", *J. Comput. Phys.*, Vol. 10, No. 2, pp. 252–271, 1972.

203. Lowe, G., "1 Blood rheology in vitro and in vivo", *Baillière's Clin. Haematol.*, Vol. 1, No. 3, pp. 597–636, 1987.

204. Lipowsky, H. H., "Microvascular rheology and hemodynamics", *Microcirculation*, Vol. 12, No. 1, pp. 5–15, 2005.

205. Dintenfass, L., "Blood rheology in cardio-vascular diseases", *Nature*, Vol. 199, pp. 813–815, 1963.

206. Schmid-Schönbein, H., "Blood rheology and physiology of microcirculation", *Ric. Clin. Laboratory*, Vol. 11, pp. 13–33, 1980.

207. Baskurt, O. K. and H. J. Meiselman, "Blood rheology and hemodynamics", *Proc Thromb. Hemost.*, 05, pp. 435–450, 2003.

208. Simmonds, M. J., H. J. Meiselman and O. K. Baskurt, "Blood rheology and aging", *JGC.*, Vol. 10, No. 3, p. 291, 2013.

209. Kwaan, H. C., "Role of plasma proteins in whole blood viscosity: a brief clinical review", *Clin. Hemorheol. Microcirc.*, Vol. 44, No. 3, pp. 167–176, 2010.

210. Neumann, F., H. Katus, E. Hoberg, P. Roebruck, M. Braun, H. Haupt, H. Tillmanns and W. Kübler, "Increased plasma viscosity and erythrocyte aggregation: indicators of an unfavourable clinical outcome in patients with unstable angina pectoris.", *Heart*, Vol. 66, No. 6, pp. 425–430, 1991.

211. Kwaan, H. C. and A. Bongu, "The hyperviscosity syndromes", *Seminars in thrombosis and hemostasis*, 2, pp. 199–208, Thieme Medical Publishers, 1999.

212. Somer, T., "4 Rheology of paraproteinaemias and the plasma hyperviscosity syndrome", *Baillie're's Clin. Haematol.*, Vol. 1, No. 3, pp. 695–723, 1987.

213. Somer, T. and H. J. Meiselman, "Disorders of blood viscosity", *Ann. Med.*, Vol. 25, No. 1, pp. 31–39, 1993.

214. Chien, S., J. A. Dormandy, E. Ernst and A. Matrai, *Clinical hemorheology: applications in cardiovascular and hematological disease, diabetes, surgery and gynecology*, Springer Science & Business Media, 2012.

215. Gupta, S. P. and V. M. Patil, "Specificity of binding with matrix metalloproteinases", *Matrix metalloproteinase inhibitors*, pp. 35–56, Springer, 2012.

216. Bell, A. G., "On the production and reproduction of sound by light", *American Journal of Science*, , No. 118, pp. 305–324, 1880.

217. Pan, D., B. Kim, L. V. Wang and G. M. Lanza, "A brief account of nanoparticle contrast agents for photoacoustic imaging", *Wiley Interdisciplinary Reviews: Nanomedicine and Nanobiotechnology*, Vol. 5, No. 6, pp. 517–543, 2013.

218. Wang, L. V. and S. Hu, "Photoacoustic tomography: in vivo imaging from organelles to organs", *Science*, Vol. 335, No. 6075, pp. 1458–1462, 2012.

219. Mallidi, S., G. P. Luke and S. Emelianov, "Photoacoustic imaging in cancer detection, diagnosis, and treatment guidance", *Trends in biotechnology*, Vol. 29, No. 5, pp. 213–221, 2011.

220. Tian, C., W. Qian, X. Shao, Z. Xie, X. Cheng, S. Liu, Q. Cheng, B. Liu and X. Wang, "Plasmonic nanoparticles with quantitatively controlled bioconjugation for photoacoustic imaging of live cancer cells", *Advanced Science*, Vol. 3, No. 12, 2016.

221. Yang, X., S. E. Skrabalak, Z.-Y. Li, Y. Xia and L. V. Wang, "Photoacoustic

tomography of a rat cerebral cortex in vivo with Au nanocages as an optical contrast agent", *Nano letters*, Vol. 7, No. 12, pp. 3798–3802, 2007.

222. Mallidi, S., T. Larson, J. Aaron, K. Sokolov and S. Emelianov, "Molecular specific optoacoustic imaging with plasmonic nanoparticles", *Optics Express*, Vol. 15, No. 11, pp. 6583–6588, 2007.

223. Culjat, M. O., D. Goldenberg, P. Tewari and R. S. Singh, "A review of tissue substitutes for ultrasound imaging", *Ultrasound in medicine & biology*, Vol. 36, No. 6, pp. 861–873, 2010.

224. Vogt, W. C., C. Jia, K. A. Wear, B. S. Garra and T. J. Pfefer, "Biologically relevant photoacoustic imaging phantoms with tunable optical and acoustic properties", *Journal of biomedical optics*, Vol. 21, No. 10, pp. 101405–101405, 2016.

225. Fonseca, M., B. Zeqiri, P. Beard and B. Cox, "Characterisation of a PVCP based tissue-mimicking phantom for quantitative photoacoustic imaging", *European Conference on Biomedical Optics*, p. 953911, Optical Society of America, 2015.

226. Bohndiek, S. E., S. Bodapati, D. Van De Sompel, S.-R. Kothapalli and S. S. Gambhir, "Development and application of stable phantoms for the evaluation of photoacoustic imaging instruments", *PloS one*, Vol. 8, No. 9, p. e75533, 2013.

227. Ephrat, P., G. C. Albert, M. B. Roumeliotis, M. Belton, F. S. Prato and J. J. Carson, "Localization of spherical lesions in tumor-mimicking phantoms by 3D sparse array photoacoustic imaging", *Medical physics*, Vol. 37, No. 4, pp. 1619–1628, 2010.

228. Spirou, G. M., A. A. Oraevsky, I. A. Vitkin and W. M. Whelan, "Optical and acoustic properties at 1064 nm of polyvinyl chloride-plastisol for use as a tissue phantom in biomedical optoacoustics", *Physics in medicine and biology*, Vol. 50, No. 14, p. N141, 2005.

229. Beard, P. C., "Photoacoustic imaging of blood vessel equivalent phantoms", *International Symposium on Biomedical Optics*, pp. 54–62, International Society for Optics and Photonics, 2002.

230. Xia, W., D. Piras, M. Heijblom, W. Steenbergen, T. G. Van Leeuwen and S. Manohar, "Poly (vinyl alcohol) gels as photoacoustic breast phantoms revisited", *Journal of biomedical optics*, Vol. 16, No. 7, pp. 075002–075002, 2011.

231. Kharine, A., S. Manohar, R. Seeton, R. G. Kolkman, R. A. Bolt, W. Steenbergen and F. F. de Mul, "Poly (vinyl alcohol) gels for use as tissue phantoms in photoacoustic mammography", *Physics in medicine and biology*, Vol. 48, No. 3, p. 357, 2003.

232. Laufer, J., D. Delpy, C. Elwell and P. Beard, "Quantitative spatially resolved measurement of tissue chromophore concentrations using photoacoustic spectroscopy: application to the measurement of blood oxygenation and haemoglobin concentration", *Physics in medicine and biology*, Vol. 52, No. 1, p. 141, 2006.

233. Pogue, B. W. and M. S. Patterson, "Review of tissue simulating phantoms for optical spectroscopy, imaging and dosimetry", *Journal of biomedical optics*, Vol. 11, No. 4, pp. 041102–041102, 2006.

234. Razansky, D., J. Baeten and V. Ntziachristos, "Sensitivity of molecular target detection by multispectral optoacoustic tomography (MSOT)", *Medical physics*, Vol. 36, No. 3, pp. 939–945, 2009.

235. Cook, J. R., R. R. Bouchard and S. Y. Emelianov, "Tissue-mimicking phantoms for photoacoustic and ultrasonic imaging", *Biomedical optics express*, Vol. 2, No. 11, pp. 3193–3206, 2011.

236. Fonseca, M., B. Zeqiri, P. Beard and B. Cox, "Characterisation of a phantom for multiwavelength quantitative photoacoustic imaging", *Physics in medicine and biology*, Vol. 61, No. 13, p. 4950, 2016.

237. Laufer, J., E. Zhang and P. Beard, "Evaluation of absorbing chromophores used in tissue phantoms for quantitative photoacoustic spectroscopy and imaging", *IEEE journal of selected topics in quantum electronics*, Vol. 16, No. 3, pp. 600–607, 2010.

238. Avigo, C., N. Di Lascio, P. Armanetti, F. Stea, L. Cavigli, F. Ratto, R. Pini, S. Meucci, M. Cecchini, C. Kusmic *et al.*, "Phantom studies with gold nanorods as contrast agents for photoacoustic imaging: novel and old approaches", *SPIE BiOS*, pp. 93234B–93234B, International Society for Optics and Photonics, 2015.

239. Avigo, C., P. Armanetti, C. Masciullo, N. Di Lascio, L. Cavigli, F. Ratto, R. Pini, M. Cecchini, C. Kusmic, F. Faita *et al.*, "Novel organosilicon phantoms as testing material for photoacoustic imaging", *SPIE BiOS*, pp. 97000I–97000I, International Society for Optics and Photonics, 2016.

240. Hirasawa, T., R. J. Iwatate, M. Kamiya, S. Okawa, Y. Urano and M. Ishihara, "Dependence of photoacoustic signal generation characteristics on fluorescence quantum yields of small organic molecule based contrast agents", *Photons Plus Ultrasound: Imaging and Sensing 2017*, Vol. 10064, p. 1006434, International Society for Optics and Photonics, 2017.

241. Atchley, A. A. and L. A. Crum, *Acoustic Cavitation and Bubble Dynamics.*, VCH Publishers, Weinheim, 1985.

242. Niermann, B., I. Budunoğlu, K. Gürel, M. Böke, F. Ö. Ilday and J. Winter, "Application of a mode-locked fiber laser for highly time resolved broadband absorption spectroscopy and laser-assisted breakdown on micro-plasmas", *Journal of physics D: Applied physics*, Vol. 45, No. 24, p. 245202, 2012.